

MULTIMODAL NANOPARTICLE-BASED PLATFORMS
FOR CANCER THERAPY

by

JONGJIN JUNG

A Dissertation submitted to the
Graduate School-New Brunswick
Rutgers, The State University of New Jersey
in partial fulfillment of the requirements

for the degree of

Doctor of Philosophy

Graduate Program in Chemistry and Chemical Biology

written under the direction of

Dr. Ki-Bum Lee

and approved by

New Brunswick, New Jersey

October, 2010

ABSTRACT OF THE DISSERTATION

Multimodal Nanoparticle-Based Platforms for Cancer Therapy

By JONGJIN JUNG

Dissertation Director:
Dr. Ki-Bum Lee

Nanoscience has attracted attention as a fast burgeoning field with promising methodologies for cancer diagnosis and therapy. We designed target-specific nanoparticle-based platforms to induce the apoptosis of human brain cancer cells and to show their capability for *in vivo* theragnostics which combines therapy and diagnosis.

Quantum Dot (QD)-based system was demonstrated to deliver siRNA and monitor its uptake using extremely bright fluorescence of QDs. siRNA-QDs against GFP not only showed increased efficiency of transfection, but also synchronized QDs' color and their localization. As a model study, glioblastoma multiforme (GBM) was chosen because of high malignancy and invasiveness resulting in short mean survival rate. Multiplexing with integrin-targeting RGD and TAT peptide enabled siRNA-QDs to be delivered specifically to U87 cells, a GBM cell line with highly expressed integrin. As a chemotheragnostic agent, siRNA-QDs were transfected into GBM cells that overexpress epidemic growth factor receptor variant III (EGFRvIII). Efficiently delivered siRNA-QDs against EGFRvIII led to abnormal cell morphology and decreased cell population. These were caused by successful knockdown of EGFRvIII gene and resulting silencing of

the PI3K/AKT signaling pathway, which plays an important role in cancer proliferation and apoptosis.

In spite of high potential of siRNA-QD system, cytotoxicity and skin depth issues lead to the development of a magnetic nanoparticle (MNP)-based theragnostic system for *in vivo* application. Graphite-coated FeCo MNPs (FeCo/C) exhibited superparamagnetic properties with high crystallinity and magnetization. In addition, Raman imaging is made possible by graphite shell designed for protection of FeCo core from decomposition and oxidation. Compared to conventional iron oxide MNPs, FeCo/C showed much higher T₂-weighted magnetic resonance contrast. Dextrans were also developed to stabilize FeCo/C in physiological condition as well as to conjugate therapeutic or targeting molecules such as siRNA, antibody, and cyclic RGD. High magnetization of FeCo/C allowed for target-specific hyperthermia against U87 cells by local heating under AC magnetic field. Additionally, siRNA-FeCo/C against EGFRvIII followed by hyperthermia synergistically induced significant cell death of U87-EGFRvIII, which proved that the target-specific siRNA-FeCo/C system is a promising candidate for *in vivo* theragnostic agent.

ACKNOWLEDGEMENTS

I would like to give all my thanks to my LORD GOD who is with me, who was with me, and who is to come, the Almighty, Amen.

Next acknowledgement is to Dr. Ki-Bum Lee, my dissertation advisor. Ki-Bum has provided generous support since I joined his laboratory. I am thankful to my dissertation committee members – Dr. Jing Li, Dr. Teddy Asefa, and Dr. Laura Fabris – for their time and helpful discussion on this dissertation. I also wish to thank Dr. Ken-Kamei Ichiro and Dr. Lawrence Williams. Ken and Lawrence have given me valuable advice and help all through our collaboration.

I would like to thank Dr. David S. Talaga, my former dissertation advisor. I also had a great time when I was in David's laboratory. It was in his laboratory that I performed my valuable single molecule experiment, and learned about protein folding and laser spectroscopy. In addition, I would like to thank colleagues in my former laboratory – Dr. Yanwen Hou, Dr. Troy C. Messina, Dr. Jason T. Giurleo, Hiyun Kim, Xianlan He, and Jeremy Pronchik – for their help and friendship.

My next acknowledgement is to my colleagues and alumni in Ki-Bum's laboratory: Dr. Cheoljin Kim, Dr. Joungkyu Park, Dr. Myung Sung, Dr. Dong Chin Lee, John D. Kim, Seungjae Lee, Mr. Kevin C. Memoli, Aniruddh Solanki, Prasad Subramaniam, Birju Shah, Stacy C. Brown, and visiting scholar, Prof. Gun-Young Jung. I especially thank Mr. Kevin C. Memoli and Choonkyu Lee for their relentless proofreading of my dissertation draft.

I wish to thank my lifelong friend – Dr. Seung-Jae Lee – for his friendship and encouragement to me, my scientific mentor – Professor Doo Wan Boo - for showing his inexhaustible passion, deep knowledge and an ideal toward the science, my actual advisor – Dr. Younggyu Kim – for the advice like proverbs stemmed from his adversity and humble guidance from his compassion, and my spiritual mentor – Pastor Hyunkyung Seong – for reminding me of God’s calling and the kingdom of God.

I am especially grateful to my sincere friends, who are like my brothers and sisters, for their encouragement and support: Dr. Eun Chan Park, who is the best neuroscientist I know and a tea time friend; Dr. Young Wook Chun, who is a romantic Pooh bear in advanced biotechnology; Dr. Hoh Baik, my former roommate and a new species of engineer who applies his professional knowledge to the soccer field for state-of-the-art, technicolor moves; Choonkyu Lee, who is genius, a promising scholar, and a caring English writing tutor; Dr. Yoon-Hui Sung, who is one of the smartest friends and a generous consultant for everything; Jiwon Lee, who always calls me a teacher; Hye-Na Yoo, who looks like a junior high school student with endless bliss.

My last acknowledgment goes to my family - my father Kyu-Man Jung, my mother Myung-Ja Lee, my sisters Jin-Hee, Jin-A, Chae-Jin – for their endless love and support. Finally, I would like to make my acknowledgement with a love cherished deep in my heart to my future fiancée in advance.

I never saw a wild thing sorry for itself.

A small bird will fall frozen dead from a bough without ever having felt sorry for itself.

- D. H. Lawrence -

DEDICATION

TO MY LORD JESUS, MY PARENTS AND MY FAMILY

TABLE OF CONTENTS

ABSTRACT.....	ii
ACKNOWLEDGMENTS.....	iv
DEDICATION.....	vi
TABLE OF CONTENTS.....	vii
LIST OF TABLES.....	xi
LIST OF FIGURES.....	xii
ABBREVIATIONS.....	xiv

I. INTRODUCTION

A. Rational Design of Multimodal Nanoparticle-Based Platforms.....	2
1. Quantum Dots (QDs)	5
2. Magnetic Nanoparticles (MNPs)	9
B. Polymeric Unit for Organic-Inorganic Nanohybrid Systems.	13
1. Polyethylene Glycol (PEG)	16
2. Biodegradable Polymers.....	17
C. Glioblastoma Multiforme and the Mutant Epidermal Growth Factor Receptor (EGFRvIII)	19
D. Small Interfering RNA (siRNA)	21
E. Silencing of the PI3K/AKT Signaling Pathway and its Signaling Crosstalk.	26
F. References.....	30
II. OVERALL OBJECTIVES.....	38

III. SELECTIVE INHIBITION OF HUMAN BRAIN TUMOR CELLS THROUGH MULTIFUNCTIONAL QUANTUM DOT-BASED siRNA DELIVERY

A. Introduction.....	42
B. Materials and Methods.....	45
1. Synthesis of QD conjugates with siRNA.....	45
2. Cell culture of U87-EGFP and U87-EGFRvIII.....	45
3. Targeted delivery of siRNA-QDs.....	46
4. Transmission electron microscopy.....	47
5. Fluorescence microscopy.....	47
6. Western blotting analysis.....	47
C. Results and Discussion.....	49
1. The multifunctional QD platform for delivery and tracking of siRNA.....	49
1.1. Synthesis of CdSe/CdS/ZnS core-shell QDs.....	52
1.2. Synthesis of the multidentate DHLA-derivatized polymer ligands..	54
1.2.1. Diamine-PEG (NH ₂ -PEG ₈ -NH ₂) (1)	55
1.2.2. Mitsunobu reaction for diamine-PEG (NH ₂ -PEG ₈ -NH ₂) (1) ..	56
1.2.3. Lipoic acid <i>N</i> -hydroxysuccinimide-ester (LA-NHS) (2)	57
1.2.4. Lipoic acid-PEG-amine (LA-PEG ₈ -NH ₂) (3)	58
1.2.5. Dihydrolipoic acid-PEG-amine (DHLA-PEG ₈ -NH ₂) (4)	59
1.2.6. Surface modification of quantum dots with DHLA-PEG ₈	60
1.3. Synthesis of the heterofunctional linkers.....	60
1.3.1. 3-(2-pyridyl)-dithiopropionic acid (PDP-OH) (5)	60
1.3.2. 3-(2-pyridyl)-dithiopropionic acid pentafluorophenyl ester (HFL1) (6)	61
1.3.3. 3-Maleimidopropionic acid (MP-OH) (7)	62
1.3.4. 3-Maleimidopropionic acid pentafluorophenyl ester (HFL2) (8)	62
2. Target-specific delivery of siRNA-QDs and their transfection efficiency	63

3. Knockdown of EGFRvIII as a chemotherapeutic target by siRNA-QDs..	70
D. Conclusions.....	74
E. Appendix.....	75
F. References.....	80

IV. GRAPHITE-COATED MAGNETIC NANOPARTICLES AS MULTIMODAL IMAGING PROBES AND HYPERTHERMIA AGENTS FOR BRAIN TUMOR CELLS

A. Introduction.....	86
B. Materials and Methods.....	89
1. Synthesis of Magnetic Nanoparticles.....	89
1.1. Synthesis of FeCo/C NPs.....	89
1.2. Synthesis of Fe ₃ O ₄ NPs.....	89
1.2.1. Synthesis of iron-oleate complex.....	89
1.2.2. Synthesis of Fe ₃ O ₄ NPs.....	89
1.3. Physical characterization of the FeCo/C NPs.....	90
2. Surface modification of the FeCo/C NPs with the functionalized dextran.....	90
2.1. T ₂ measurements.....	90
2.2. Conjugation of targeting molecules to FeCo/C NPs.....	91
3. Cell culture of U87-EGFP and other control cells.....	91
4. <i>In vitro</i> imaging.....	92
4.1. MR imaging.....	92
4.2. Raman imaging.....	92
5. <i>In vivo</i> MR imaging.....	93
6. Hyperthermia measurements.....	93

C. Results and Discussion.....	95
1. The synthesis of high performance FeCo/C NPs and their magnetic properties.....	95
1.1. The synthesis of FeCo/C NPs.....	100
2. The MR/Raman imaging of FeCo/C for single cell and in vivo.....	101
3. Dextran-coated FeCo/C NPs.....	105
3.1. Synthesis of amine functionalized dextran.....	108
3.1.1. Dextran functionalized with 4-nitrophenyl chloroformate groups (4-NC dextran) (2)	108
3.1.2. Dextran functionalized with amine groups (3)	109
3.2. Synthesis of carboxyl functionalized dextran.....	110
3.2.1. Dextran functionalized with carboxyl groups (4)	110
4. Target-specific hyperthermia-based cancer therapy.....	113
5. A combined therapy via siRNA and hyperthermia for synergistic silencing of the PI3K/AKT signaling pathway in bTCs.....	120
D. Conclusions.....	123
E. Appendix.....	124
F. References.....	130
 V. CONCLUSIONS AND PERSPECTIVES.....	 135
 CURRICULUM VITAE.....	 142

LISTS OF TABLES

Table I-1	Summary comparison of the synthetic methods for MNPs	10
Table I-2	Conventional and new types of nanoparticle-based MRI contrast agents	12

LIST OF FIGURES

Figure I-1.	Multimodal and multifunctional nanoparticle platforms	4
Figure I-2.	Thermal decomposition method for the synthesis of monodisperse and high quality quantum dots.....	8
Figure I-3.	Schematic illustration of nanocomposites including polymeric carrier for cancer therapy.....	14
Figure I-4.	EGFR/mutant EGFR in the PI3K/AKT signaling pathway and their effect on brain tumor cells.....	20
Figure I-5.	Mechanism of RNA interference by siRNA.....	22
Figure I-6.	Proton sponge effect and endosomal escape of nanocarriers.....	24
Figure I-7.	Signaling crosstalk by FAK and ERK between EGFR and Integrin influencing cellular structural dynamics.....	27
Figure III-1.	Quantum dots as a multi-functional nanoplatfrom.....	43
Figure III-2.	TEM image of DHLA-PEG ₈ -amine coated CdSe/CdS/ZnS core-shell QDs.....	51
Figure III-3.	TEM image of CdSe/CdS/ZnS core-shell QDs.....	53
Figure III-4.	Synthetic routes to DHLA-PEG-NH ₂ & heterofunctional linkers.....	54
Figure III-5.	Toxicity of QDs using MTS assay.....	63
Figure III-6.	Knockdown of EGFP in U87 cells using siRNA-QDs.....	64
Figure III-7.	Knockdown of EGFP in U87 cells using siRNA-QD modified with RGD and HIV-Tat peptides.....	68
Figure III-8.	Knockdown efficiency of EGFP within U87-EGFP cells and internalization of multifunctional siRNA-QDs.....	69
Figure III-9.	Phase contrast images showing the internalization of siRNA- QDs against EGFRvIII into the U87-EGFRvIII cells.....	72

Figure III-10.	Knockdown of EGFRvIII in U87-EGFRvIII cells using multifunctional siRNA-QDs.....	73
Figure IV-1.	Multimodal magnetic FeCo graphite nanoparticles for multimodal imaging and targeted brain tumor therapy.....	87
Figure IV-2.	Structural and magnetic properties of the FeCo/C NPs.....	98
Figure IV-3.	HR-TEM image of FeCo/C NPs as a function of [FeCo]/Sucrose ratio.....	99
Figure IV-4.	MR measurements and imaging of FeCo/C NPs and Resovist....	103
Figure IV-5.	MR and Raman imaging of FeCo/C NPs in various cell lines....	104
Figure IV-6.	Synthesis of various dextran derivatives and coating with FeCo/C NPs for bioconjugation.....	106
Figure IV-7.	Bioconjugation strategies for cRGD peptide/EGFR antibody coupling to dextran coated FeCo/C NPs with a functional group.....	107
Figure IV-8.	Synthesis of dextran functionalized with 4-nitrophenyl chloroformate groups and amine groups.....	108
Figure IV-9.	Synthesis of dextran functionalized with carboxyl groups.....	110
Figure IV-10.	Photographs of colloidal solutions of 11nm FeCo/C NPs.....	112
Figure IV-11.	<i>In vitro</i> hyperthermia studies of the FeCo/C NPs.....	115
Figure IV-12.	Characterization for <i>In vitro</i> hyperthermia studies and siRNA delivery using the FeCo/C NPs.....	116
Figure IV-13.	U87-EGFP cell death induced by hyperthermia using FeCo/C and Fe ₃ O ₄ NPs.....	117
Figure IV-14.	Targeted hyperthermia using FeCo/C NPs in co-cultures of U87-EGFP and astrocytes.....	118
Figure IV-15.	Annexin-V assay for quantification of apoptotic cells in co-cultures of U87-EGFP cells and astrocytes.....	119
Figure IV-16.	siRNA-mediated knockdown and hyperthermia using siRNA-FeCo/C constructs in U87 cells.....	122

ABBREVIATIONS

NP	Nanoparticle
QD	Quantum dot
MNP	Magnetic nanoparticle
PEG	Polyethylene glycol
PLGA	Poly (lactic-co-glycolic acid)
PBAE	Poly (β -amino ester)
siRNA	Small interfering RNA
TOP	Tri-octylphosphine
TOPO	Tri-octylphosphine oxide
TBP	Tri-butylphosphine
SILAR	Successive ionic layer absorption and reaction
acac	acetylacetonate
MR	Magnetic resonance
SPIO	Superparamagnetic iron oxide
MEIO	Magnetism-engineered iron oxide
CLIO	Cross-linked iron oxide
CVD	Chemical vapor deposition
PEI	Polyethyleneimine
PLA	Poly (D, L-lactic acid)
PCL	Poly (ϵ -caprolactone)
PAMAM	Poly (amido amine)
CD	Cyclodextran
RES	Reticuloendothelial system
PHEA	Poly (hydroxyethyl-L-asparagine)
PHEG	Poly (hydroxyethyl-L-glutamate)
PGA	Poly (glutamic acid)
PLL	Poly-L-lysine
GBM	Glioblastoma multifome
EGFR	Epidermal growth factor receptor

EGFRvIII	Epidermal growth factor receptor variant III
RISC	RNA-induced silencing complex
RLC	RISC-loading complex
Ago2	Argonaut2
nt	Nucleotide
shRNA	Short hairpin RNA
GFP	Green fluorescence protein
RTK	Receptor tyrosine kinase
FAK	Focal adhesion kinase
ERK	Extracellular signal-regulated kinase
RNAi	RNA interference
HDA	Hexadecylamine
DHLA	Dihydrolipoic acid
PTPPf	3-(2-pyridyl)-dithiopropionic acid pentafluorophenyl ester
MPPf	3-maleimidopropionic acid pentafluorophenyl ester
FRET	Fluorescence resonance energy transfer
ODE	1-octadecene
LA-NHS	Lipoic acid <i>N</i> -Hydroxysuccinimide-Ester
PDP-OH	3-(2-Pyridyl)-dithiopropionic acid
MP-OH	3-Maleimidopropionic acid
TEM	Transmission electron microscopy
bTCs	Brain tumor cells
XRD	X-ray diffraction
SQUID	Superconducting quantum interference device
CNT	Carbon nanotube
cRGD	Cyclic RGD
4-NC dextran	Dextran with 4-nitrophenyl chloroformate
SAR	Specific absorption rate
MAA	Mercaptoacetic acid
MSA	Merceptosuccinic acid

CHAPTER I

INTRODUCTION

A. Rational Design of Multimodal Nanoparticle-Based Platforms

Nanoscience refers to the study of structures on the scale of approximately 1~1000nm and their applications in various fields such as solar cells, electronic devices, drug/gene delivery, regenerative medicine, tissue engineering, and biological diagnosis¹⁻⁴. This field has been rapidly burgeoning during the last two decades and especially its biological application has been widely demonstrated as a proof-of-principle. Recently, the successful emergence of nanoscience is required to be practically applied to the clinical medicine field to solve many key problems concerning cancer biology for therapy² as well as regenerative medicine using stem cells¹. In this study, I focused on the design of target specific nanoparticle-based platforms to induce the apoptosis of cancer cells and to show their capacity to be extended to in vivo systems for the further clinical purpose of using them as theragnostics which combines therapy and diagnosis.

Amongst various nanoparticles (NPs), inorganic NPs have been drawing significant attention from physicists and biologists due to their unique physical features such as electronic, magnetic, and optical properties as well as their promising application in the biomedical field. The advantage of inorganic NPs is that they can be used as efficient delivery vehicles because their high surface to volume ratio makes possible an enlarged loading capacity by functionalizing with high density on the surface. Their unique chemical or physical properties can also be utilized for diagnosis, therapy, and controlled release. Here, I used semiconductor NPs-quantum dots (QDs)⁵- magnetic nanoparticles (MNPs)⁶, and Polymer-MNP nanohybrid⁷ for cancer therapy and diagnosis. In order to maximize NPs' full potential and harness the purpose to use NPs, it is required to design rationally the efficient NP-based platform.

First, most NPs are synthesized in an organic solvent environment and surrounded by hydrophobic ligands. Because all biological systems are based in aqueous media, hydrophilic ligands should surround the surface of NPs to make them water-soluble⁸. Moreover, coated ligands will be able to maintain their unique properties and be stable in various salt concentrations and pH ranges. Typically there are two different methods to make NPs water-soluble^{9,10}. One is to exchange the as-deposited hydrophobic ligands with new hydrophilic ligands containing a replacing moiety via stronger chemical reactivity. The other one is the ‘addition method’ that incorporates amphiphilic chemicals into the hydrophobic ligands to expose the hydrophilic part outside. These two approaches have advantages and disadvantages. The exchange method can maintain the original size of the NPs. However, it affects the properties of the core materials due to the changed physical structure of the interface between ligand and the NPs’ core. Meanwhile, the addition method maintains the NPs’ properties independent of their size¹¹.

Second, in addition to hydrophilic part of ligands for water-soluble NPs, other molecules such as polyethylene glycol (PEG) can be linked for the prevention of nonspecific binding of biomolecules. PEG has been known to be biologically inert and plays an important role in blocking access of reactive chemicals to the core. Especially, PEGylation must be carried out to extend circulation time in *in vivo* applications by preventing early secretion by kidney or opsonization which stimulates immune response. PEG can be replaced by various polymeric units such as PLGA[poly(lactic-co-glycolic acid)] and PBAE [poly(β -amino ester)] for other purposes. For example, these increase the loading capacity for drugs or small interfering RNA (siRNA) delivery. In addition, there could be specific roles to overcome biological barriers for target-specific delivery^{12,13}.

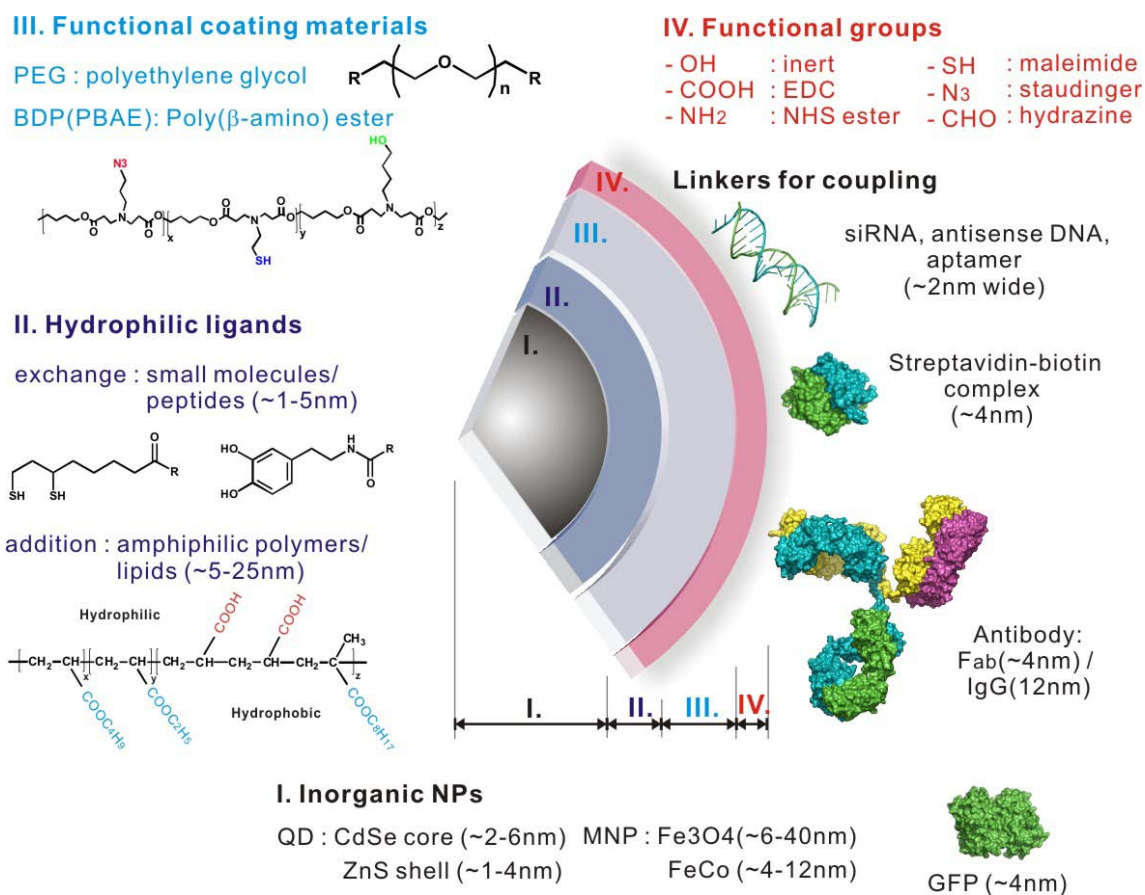


Figure I-1. Multimodal and multifunctional nanoparticle platforms

Third, various functional groups can be placed on the end moiety to affect multifunctionality via conjugation with various molecules and to modulate surface charge¹⁴. Each functional group should be selected according to its unique uses due to the different chemical properties of the conjugating units. Hydroxyl group is very stable in aqueous solution and inert. Therefore, it can be used to make the system more water-soluble, protected from nonspecific binding and access of chemically reactive

species. Amine group or carboxylic group can conjugate biomolecules with a covalent bond via amine-NHS ester conjugation or EDC coupling. If the functional group is overlapped with target molecules' one, bifunctional linkers are required. Thiol group can be utilized to attach molecules with various methods via covalent bond and disulfide bond. Thiol-maleimide conjugation is the usual method to conjugate covalently target molecules in a highly specific manner. In addition, this group can be linked to other molecules via disulfide bond by dithiopyridyl functional moiety, which allows the release of attached molecules under reducing conditions in the cytoplasm in the presence of glutathione and dihydrolipoic acid. Recently, novel functional groups such as azide and aldehyde have been demonstrated to show Staudinger reaction based click chemistry and hydrazone based conjugation methods¹⁵.

All these methods maintain the unique physical properties of the core while maximizing the loading capacity as a delivery vehicle and making use of the surface area for multiplexing and targeting. Core materials in this study are briefly introduced in the following section.

1. Quantum Dots (QDs)

QDs - Semiconductor nanoparticles - have been considered as a representative nanosystem because it shows novel quantum physical properties such as quantum confinement effect and quantum size effect beyond classical mechanics¹⁶⁻¹⁸. For biological applications, QDs have attracted interest because quantum confinement generates unique optical properties. According to their sizes, QDs emit photons with different wavelengths due to different band gap energies between the conduction and valence bands: smaller sizes

emit in the short wavelength range and larger size radiates longer wavelength photons. In addition, they have broad absorption ranges and narrow emission peaks, which enables multicolor detection with a single light source. Most of all, high quantum yields and extinction coefficients generate about fifty times higher brightness than general organic dyes. Enhanced photostability makes them strong candidates for the substitution of organic dyes in the fields of single molecule biophysics and cell biology¹⁹⁻²¹.

Although new QDs independent of the size effect have recently been developed, this chapter will briefly introduce the development of size dependent CdSe based QD systems. Modern QD synthesis had been pioneered by Bawendi *et al* via hydrothermal methods that produce high quality QDs with narrow size distributions ($< 30\text{nm}$ FWHM in emission spectra) and high brightness using relatively simple parameters such as temperature and concentration¹⁶. Thermal decomposition methods make infinitive seed crystals by injecting and reacting reactive species such as Se in TOP (Tri-octylphosphine) into another one such as $\text{Cd}(\text{CH}_3)_3$ in TOPO (Tri-octylphosphine oxide) at a specific temperature. The size is controlled by temperature and time. This approach has been further developed by the Alivisatos group, replacing the ligand, TOP, with TBP and other parameters^{16,18}.

Because a CdSe core is relatively vulnerable to reactive chemicals, shells with different species with different band gaps have been deposited on the surface of the CdSe core. Guyot-Sionnest *et al* showed CdSe/ZnS core shell QDs which are more stable and brighter¹⁶. As introduced synthetic routes use dimethyl cadmium as a Cd source which easily decomposes, is highly reactive in ambient conditions, and is highly toxic. Seeking an easier synthetic method and greener approach, Peng *et al* has succeeded in replacing

dimethyl cadmium with other cadmium species such as cadmium oxide and cadmium acetate which are very stable at room temperature in air/oxygen-exposed conditions²²⁻²⁵. They tested various fatty acids and amines to find good ligands for high quality CdSe QDs. They also introduced non-coordinating solvents such as octadecene to apply this new methodology to other types of QD synthesis and to adjust the reaction volume as an important parameter without affecting the behavior of other reactive components²⁶⁻²⁸. They also significantly contributed to the development of core-shell QD synthesis by introducing the SILAR (Successive Ionic Layer Absorption and Reaction) method which deposits metal layer-by-layer on bulk materials. After the mole concentration of CdSe core is calculated, the exact amount of each species for shell deposition is added with controlled speed at a specific temperature in order to deposit them homogenously on the core surface^{29,30}. As a result, high numbers of shell layers can be deposited without further purification and size sorting steps. In addition, by depositing CdS and ZnS shell layers, emission spectra can be shifted in a controlled manner and lattice mismatch is significantly reduced to 5% from 15% which is produced when just one ZnS shell is layered³¹⁻³³.

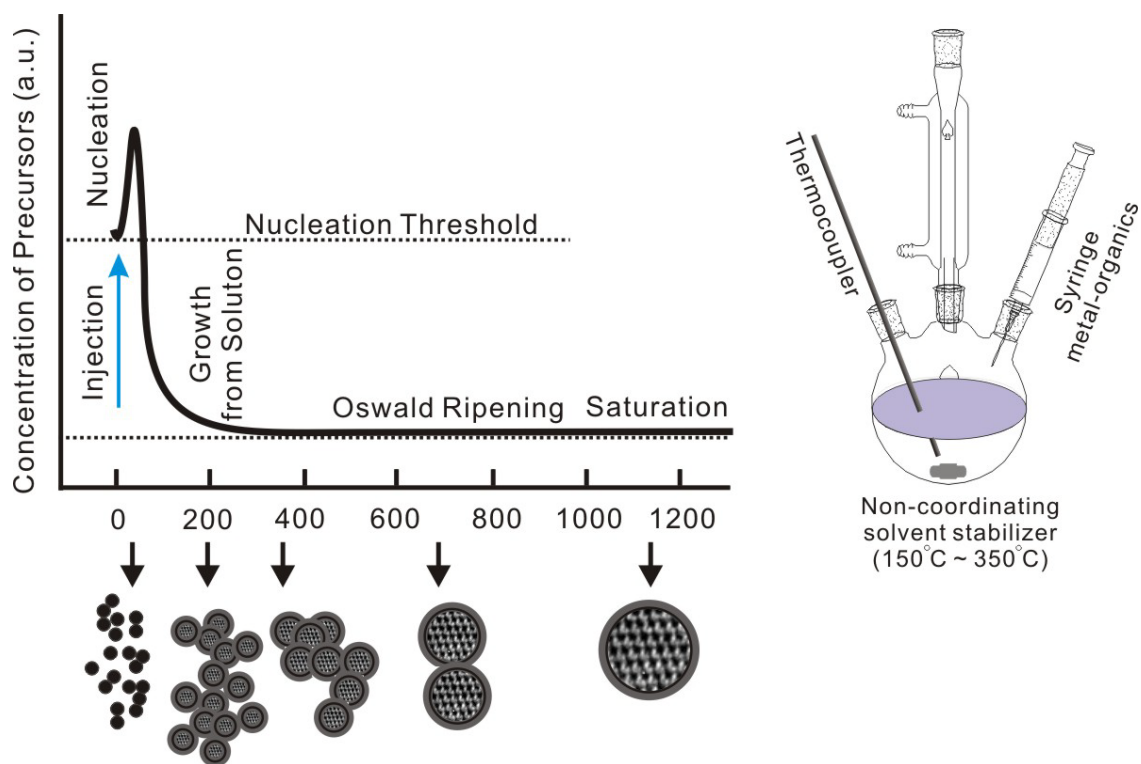


Figure I-2. Thermal decomposition method for the synthesis of monodisperse and high quality quantum dots

Adapted with the permission from ref. 18

2. Magnetic Nanoparticles (MNPs)

MNPs are typical inorganic NPs with new magnetic properties by the quantum confinement effect within the sub-micron size and the surface effect. Bulk magnetic particles show multi-domain ferromagnetism as particle size increases while smaller nanoparticles under the critical size have single domain ferromagnetism with higher H_c values^{34,35}. Depending on size, shape, and components, thermal energy becomes higher than magnetic spin energy barrier enough to fluctuate freely between different spin directions. Therefore, net magnetization is zero under free spin fluctuation conditions, which has been called superparamagnetism^{36,37}. In addition, as the NPs' size is decreasing, portion of atoms on the surface area of NPs is higher than core. In spite of uniformly aligned magnetic spins of core, spins on the surface are tilted and disordered, which is named 'surface-spin canting effect'. When the size of MNPs is under a certain nanometer scale, canted spins on the surface would represent unexpected magnetic phenomena³⁵.

Several different approaches have been developed for the synthesis of MNPs. Here, I will focus on the thermal decomposition method and hydrothermal method for iron oxide MNP and iron cobalt MNP synthesis because these synthetic methods have been used for this study^{37,38}. The thermal decomposition approach was adapted and modified from the synthesis of semiconductor nanoparticles. Generally, thermal decomposition is the chemical reaction in heated conditions where each component breaks up and forms new species reacting with another component. In the MNP synthesis, organometallic compounds such as $\text{Fe}(\text{acac})_3$ (acac=acetylacetonate), surfactants as a ligand, and organic solvent are exposed to high temperature with quantified ratios of each component. The reaction temperature, reaction time, and ratio are critical parameters for the monodispersity,

morphology, and size. With slight modification, various methods have been developed for high quality MNPs.

On the other hand, hydrothermal synthesis had been a terminology that is mainly limited to the synthesis of single crystals in high temperature aqueous solution at high vapor pressures. The crystals grow in an instrument called an ‘autoclave’, made of Teflon-lined stainless steel to endure high pressure and temperature. This method utilizes reaction at the interface of each phase and phase transfer between solid and solution. In this reaction, uniform size distribution and high crystallinity are caused by high pressure generated by high temperature in the reaction with the assistance of stirring. Because the reaction of this method is performed in aqueous solution, it can produce water-soluble NPs with the generation of minimal waste products.

Table I-1 : Summary comparison of the synthetic methods for MNPs

Synthetic method	Synthesis	Reaction temp [°C]	Reaction period	Solvent
Thermal decomposition	Complicated, inert atmosphere	100 -320	Hours-days	Organic solvent
Hydrothermal synthesis	Simple, high pressure	220	Hours ca.days	Water, ethanol

Synthetic method	Surface-capping agents	Size distribution	Shape control	yield
Thermal decomposition	Needed, added during reaction	Very narrow	Very good	High/ scalable
Hydrothermal synthesis	Needed, added during reaction	Very narrow	Very good	medium

Copyright Wiley-VCH Verlag GmbH & Co. KGaA.

Reproduced with the permission of Ref. 37.

For the past two decades, Fe_2O_3 iron oxide MNPs have been investigated for the characterization of aforementioned properties of MNPs compared to the bulk materials³⁹. Under a certain size range they show enhanced magnetic resonance (MR) imaging properties and magnetization due to the generation of superparamagnetism. They have been called SPIO (SuperParamagnetic Iron Oxide) MNPs and Hyeon *et al* have developed the synthesis of another type of SPIO with Fe_3O_4 ⁴⁰. Compared to Fe_2O_3 SPIOs, Fe_3O_4 SPIOs have stronger magnetization and higher MR contrasting ability⁴¹. However, they require an organic stabilizer such as dextran because they are unstable and decompose easily in physiological conditions. As a result, they have been commercialized for liver or kidney specific contrasting agents with the following names: Resovist⁴², Feridex, Combidex.

In the meantime, the Cheon group has developed a synthetic approach for MEIO (magnetism-engineered iron oxide) NPs with high and tunable nanomagnetism, and resulting enhanced MR contrasting⁴³. Although the synthetic method was not published due to patent issues, they claim that uniform, single crystalline and highly magnetized Fe_3O_4 MEIO was obtained under high temperature in an organic medium without further description of the synthesis. They also reported that compared to SPIO and related NP probes such as CLIO (cross-linked iron oxide) with severe limitation for MR imaging because of low magnetic moment and low r_2 coefficient, MEIO has superior magnetic properties such as high and tunable mass magnetization and short spin-spin relaxation time of the proton, which are critical for advanced MR imaging. They further demonstrated new types of MEIO by doping several transition metals (Mn, Ni, Co) which replace Fe^{2+} ion and generate a new configuration of magnetic spin as a result of new electron spin structures.

MnFe₂O₄ (MnMEIO) NPs showed significantly enhanced mass magnetization values and were targeted to cancer in the mouse resulting in highly sensitive imaging.

Table I-2 : Conventional and new types of nanoparticle-based MRI contrast agents

Name	Magnetic core size [nm]	Total size[nm]	Coating material	$r^{2[a]}$ [mM ⁻¹ S ⁻¹]	B[T]
<i>Conventional MNP agents</i>					
AMI-25 ^[39] (Feridex;Endorem)	5-6	80-150	Dextran	ca. 100	0.47
SHU 555A ^[42] (Resovist)	ca.4.2	ca.62	Carbodextran	151	0.47
AMI-227 ^[40] (combidex;Sinerem)	4-6	20-40	Dextran	53	0.47
CLIO; MION ^[41]	ca. 2.8	10-30	Dextran	ca.69	1.5
<i>New types of synthetic MNPs</i>					
Fe ₃ O ₄ (MEIO) ^[43]	12	15	DMSA	218	1.5
MnFe ₂ O ₄ ^[43] (MnMEIO)	12	15	DMSA	358	1.5
FeCo ^[44]	7	30	Carbon and phospholipids-PEG	644	1.5

[a] The r^2 value are literature values and can be slightly variable depending on the field strength and MR pulse sequence

Copyright Wiley-VCH Verlag GmbH & Co. KGaA.

Reproduced with the permission of Ref.38

Metal alloy types of MNPs such as FeCo and FePt have attracted nanoscientists' interest as strong candidates to be MR contrast agents because of much higher magnetization than any type of iron oxide MNPs. However, the development of synthetic methods is quite challenging due to poor chemical stability and easy oxidation⁴⁵.

The Dai group reported that MNPs composed of FeCo core and a graphitic shell were synthesized with high magnetization values. They insisted that this system has even T₁ and T₂ contrast imaging ability. Silica was used as a template for making nanocrystal seeds via ultra-sonication⁴⁴. A graphitic shell was deposited on the surface of FeCo core via CVD (chemical vapor deposition) method. After the core-shell FeCo/C MNPs were made, they were purified from silica using hydrofluoric acid. They also applied exactly same approach to synthesize FePt/C MNPs. The Liu group published a thermal decomposition method for the synthesis of FeCo. Fe(acac)₃ and Co(acac)₃ were used with several ligands for the FeCo core and as-produced FeCo was annealed in a high temperature heating furnace. They insisted that carbon graphite was formed on the surface of FeCo core during the annealing process and it prevents the degradation of the FeCo core⁴⁶.

B. Polymers for Organic-Inorganic Nanohybrid Systems

Polymers are promising nanocarriers and can be useful for organic – inorganic nanohybrid systems⁴⁷. Because polymer is an organic material and its synthetic methods are well-established, it has many outstanding advantages which can make up for the lack of unique physical properties of inorganic one. Different from hard materials like inorganic nanocrystals, polymeric nano-systems are soft materials and can be integrated into the metabolic pathway in biological systems for secretion after expiration of their functions. In order to solve this issue and controlled release of conjugated materials, polymer nanochemists have further developed biodegradable polymers which break down by pH level and enzyme. Well-established synthetic routes make it possible to tailor

nano-systems for their purpose such as functionalization for conjugation with biomolecules, efficient delivery, and 'stealth' function to escape from immune responses.

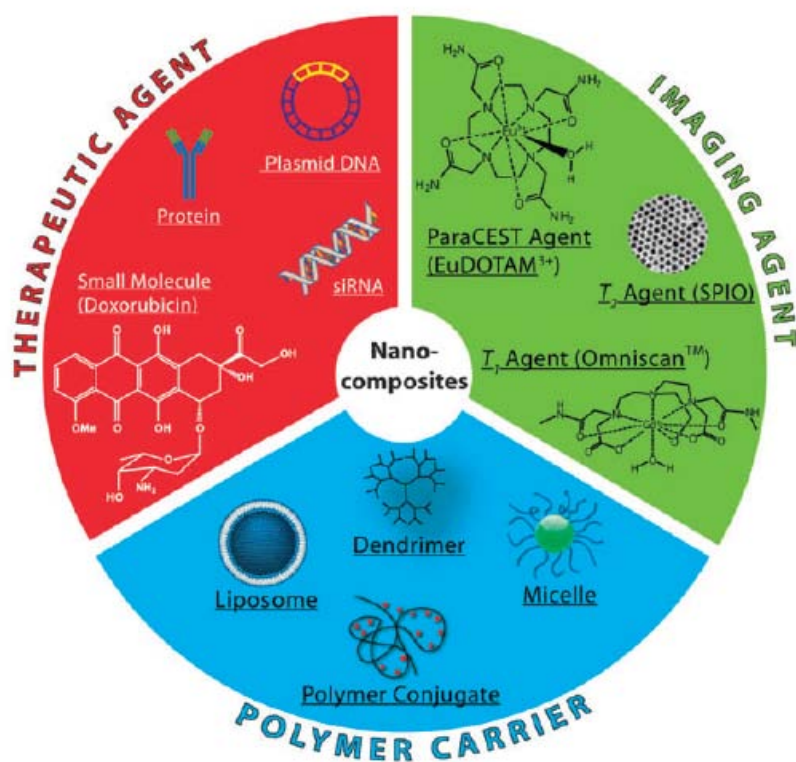


Figure I-3. Schematic illustration of nanocomposites including polymeric carrier for cancer therapy

Reproduced by permission of The Royal society of Chemistry from ref. 53

Polymers themselves can be nanocarriers for the delivery of drugs, gene plasmids, and siRNA⁴⁸. First, polymers such as PEG, N-(2-hydroxypropyl) methacrylamide, PEI, and dendrimer can covalently or non-covalently conjugate drug/siRNA molecules, and targeting molecules such as antibody can be attached in addition to relatively easy control

of net charge⁴⁹. Second, amphiphilic block copolymers can form micelles for the delivery of hydrophobic anticancer drugs or imaging probes. The inner hydrophobic part is usually prepared with poly (D, L-lactic acid) (PLA) and poly (ε-caprolactone) (PCL), and the outer hydrophilic part is composed of PEG-based polymers for the prevention of nonspecific binding as well as conjugation with targeting molecules. Third, the formation of nano-sized liposomes has been explored intensively for several decades for drug delivery and prolonged circulation time in vivo. Amphiphilic phospholipids, block copolymers, and cholesterol form bilayers like cell membrane via a self-assembly process. Fourth, supramolecular nanoparticle platforms are proposed for efficient drug conjugation and delivery. The Tseng group synthesized a PAMAM (1st generation polyamidoamine dendrimer)-PEI-PEG based nanoparticle system. Adamantane (Ad)-conjugated PAMAM forms nanoparticles with small sizes, and cyclodextran (CD)-conjugated PEI plays the role of glue to put together Ad-PAMAM nanoparticles via docking of Ad into CD. Ad-PEG can bind to this platform via the same mechanism. Their size can be modulated by changing the ratio of each component⁵⁰.

One reason to use polymers for inorganic nanomaterials is to make hydrophobic NPs water-soluble and biocompatible by coating with amphiphilic polymers or exchanging chemicals. Especially the Nie group has synthesized size-controllable functional polymers for QDs. Polymer-magnetic nanoparticle hybrids have also been developed for increased circulation time and ‘stealth’ function⁵¹. In addition, it is also used to conjugate drug molecules to use as in vivo theragnostics (therapy + diagnostics). Jon *et al* reported that the SPIO nanoparticles with a polymer shell which is composed of poly-3-(trimethoxysilyl) propyl methacrylate-r-PEG methyl ether methacrylate-r-N-acryloxy-succinimide⁵². By

incorporating doxorubicin into the polymer non-covalently, it was released in lung carcinoma tissue in mice, and tumor shrinkage was confirmed with MRI imaging. Haam *et al* also used biodegradable poly(lactic-co-glycolic acid) (PLGA) to make multifunctional complexes with several SPIO MNPs, doxorubicine, and targeting antibody⁴⁷. It showed several times stronger MR imaging sensitivity than individual SPIO MNPs, successful targeting with Herceptin which is a therapeutic antibody, and decreased size of tumor tissue by doxorubicine and Herceptin⁵³.

1. Polyethylene Glycol (PEG)

PEG is one of the most popular polymeric materials for biological and clinical application. At first, it has been preferred because of significantly reduced nonspecific binding of biomolecules, and dramatically increases the stability of proteins after it is conjugated. Generally speaking, PEG is an inexpensive polymer, has 'stealth' behavior against immune system, increases the blood circulation time, and decreases the uptake by the reticuloendothelial system (RES). Most of all, a lot of PEG-drug platforms have been already approved by FDA.

PEG allows the avoidance of renal clearance by modulating the conjugating molecules' mass because of the threshold size for clearance and the molar mass of PEG can easily be produced. It also represents a high solubility in aqueous solutions and organic solvents. Functionalization of end-groups have been comprehensively exploited, which resulted in widespread commercialization with low cost. In aqueous solution, it has highly flexible structures and prevents the access of proteins and reactive chemicals due to steric hindrance and its intrinsic inertness⁵⁴.

On the other hand, PEG has several disadvantages. Most of all, it is not biodegradable. Usually, relatively low-molar-mass PEGs have been used because about 60kDa is a threshold level for renal clearance. However, if PEGs with a low molar mass under 400Da are administered, it is reported that there are toxic effects because of diacid and hydroxyl acid metabolites produced by alcohol and aldehyde dehydrogenases. Usually mechanical stress such as stirring, flow, and ultrasound can induce polymers to be degraded. However, mechanical stress tests have not been carried out for PEG polymers and materials conjugated to PEGs. Since PEG shows significant scission at 50-60 °C for a certain period, it can affect the synthetic process of PEGylation to other materials. In addition, it can be photo-oxidized and degraded under UV light by forming ester and formate groups.

As an alternative to PEG for drug delivery, several polymers units have been investigated: biodegradable poly(amino acid)s such as poly (hydroxyethyl-L- asparagine) (PHEA), poly(hydroxyethyl-L-glutamate)(PHEG), and poly(glutamic acid) (PGA), and non-biodegradable polymers such as poly(glycerol), poly(2-oxazoline)s, poly (acrylamide), poly (vinylpyrrolidone), and poly (N-(2-hydroxypropyl) methacrylamide).

2. Biodegradable Polymers

Various polymers have been developed and tested for drug/gene delivery including siRNA, and hybrids with inorganic nanoparticles. These polymers have to satisfy the following conditions: they should be biocompatible and shows minimized cytotoxicity, it is preferred to be biodegradable or other controlled release tool such as light, pH, or

enzyme sensitivity for the quantitative secretion of conjugated molecules, and they should be easily functionalized to attach auxiliary molecules for the multifunctionality⁵⁵.

Cationic polymers such as poly-L-lysine (PLL), polyethyleneimine (PEI), poly(amido amine)s (PAMAMs) have been used for gene/siRNA delivery and nanohybrids with inorganic nanoparticles due to easy crossing of the endosomal barrier⁵⁶. However, it has an intrinsic cytotoxicity problem due to strong positive charges and difficult –to-control net positive charge, and the release and secretion mechanism has not been elucidated well owing to non-biodegradability.

Poly(lactic-*co*-glycolic acid) (PLGA) has been utilized to form a functional block copolymer for drug delivery and nanohybrids for highly sensitive nanoaggregates of MNPs. Even though it has excellent properties such as biodegradability and biocompatibility, the net charge cannot be controlled and addition of functional groups is quite limited.

In order to satisfy all these criteria, polymer chemists have developed PEI-based degradable polymers for gene/siRNA delivery. Instead of cytotoxic PEI (10~25kDa), low-molecule-weight (LMW) PEI has been used for less cytotoxicity and its poor transfection efficiency has been overcome with biodegradable cross linkers by hydrolysis at neutral pH or endosomal low pH, enzymatic degradation, and cytoplasm specific degradation via glutathione as well as DHLA (dihydrolipoic acid). The other approach is to synthesize graft copolymers with LMW PEI with other supplementary chemicals such as nonionic hydrophilic cyclodextrin (CD) for high stability and less cytotoxicity, degradable polycaprolactone (PCL), chitosan, dextran, and poly(propylene imine) dendrimers.

Recently, the Langer group has developed poly(b-amino ester) (PBAE) polymers as promising tools for siRNA/shRNA delivery and regenerative medicine using stem

cells⁵⁷. Because of the amino ester backbone, it has an intrinsically mild positive charge to form a complex with the phosphate backbone of gene/siRNA, and can be easily linked with functional groups for further bioconjugation in addition to biodegradability and biocompatibility. The Langer group has kept proposing the synthetic scheme to import useful side chains such as amines or thiols for further conjugation with targeting molecules such as cRGD and antibody, and various end groups for the increase of transfection efficiency⁵⁸. They further showed that once it makes a hybrid with nanoparticles, its delivery can be accomplished with high efficiency.

C. Glioblastoma Multifome (GBM) and the Mutant Epidermal Growth Factors

Receptor (EGFRvIII)

According to the national cancer reports, primary malignant brain tumors and other nerve system tumors occur in about 23,000 people annually and 13,000 of malignant brain tumor patients die every year. Especially Glioblastoma Multifome (GBM) originating from glial cells is known to be the most malignant, invasive, fast-progressive, and difficult-to-treat brain tumor⁵⁹. Moreover, the mean survival rate after cancer treatment is just 10-12 months^{60,61}. Because there are a lot of biological barriers for chemotherapy and surgery for brain tumor, it is necessary to develop novel early diagnostic tools and therapeutic strategies and nanotechnology can be a promising tool.

The epidermal growth factor receptor (EGFR) is the key protein placed in upstream of the PI3K/AKT signaling pathway^{62,63}. Because this signaling pathway plays a critical role in cell proliferation and apoptosis, several drug molecules are targeted to

down-regulate it by inhibiting the function of the protein in this pathway such as Erlotinib/Gefinib for EGFR, and Rapamycin for mTOR. EGFR forms a dimeric complex when the ligand such as epidermal growth factor binds to the active site on the extracellular domain^{64,65}. Subsequently, the kinase domain in cytoplasm region of each monomer is close together and phosphorylates the tyrosine residue on the long and flexible tail. That complex transmits the proliferation triggering signal to following proteins in the downstream such as AKT, mTOR, and S6⁶⁶.

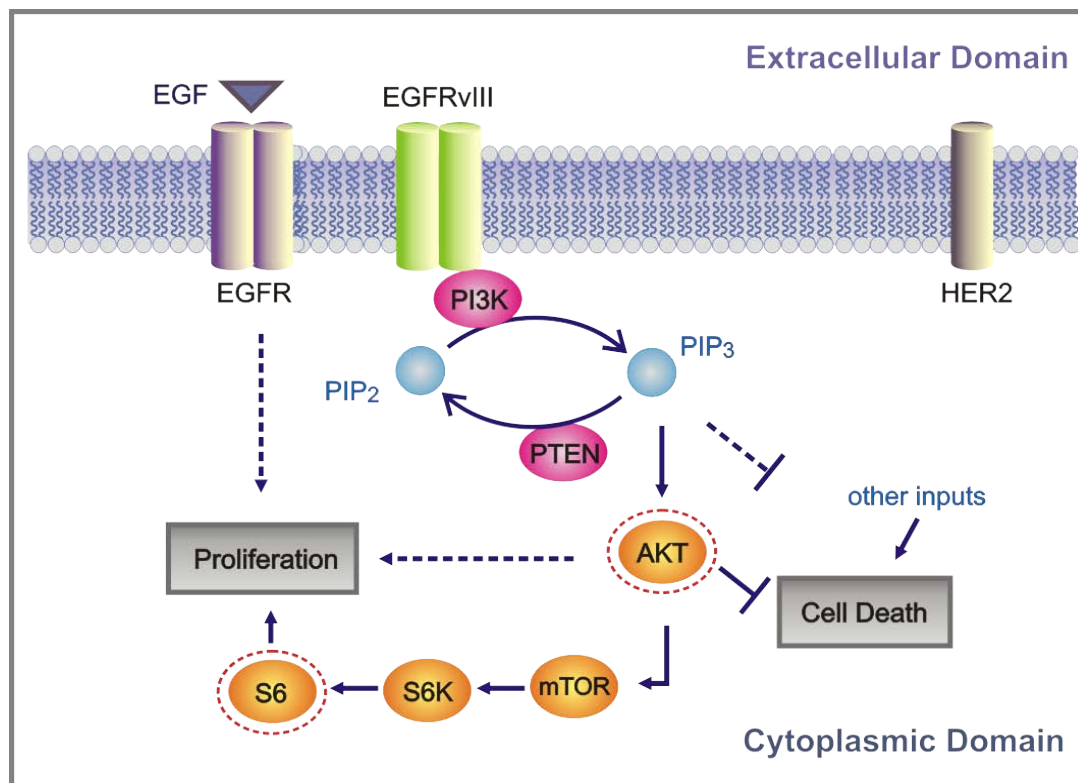


Figure I-4. EGFR/mutant EGFR in the PI3K/AKT signaling pathway and their effect on brain tumor cells

Adapted with permission from ref. 68

EGFR is a universal and key receptor tyrosine kinase for cellular growth and progression. However, most cancer cells overexpress EGFR which is a key oncogene involved in the fast proliferation rate, because it makes cells highly sensitive to small amounts of ligands. There is also a mutant form of EGFR (EGFRvIII) in many cancers, which lacks amino acids from 6 to 273 in the extracellular domain and is always activated without ligand binding^{67,68}. Reportedly, EGFRvIII is expressed in several types of cancers such as glioma, medulloblastomas, breast carcinomas, and ovarian carcinomas^{69,70}. A more interesting point is that EGFRvIII is tumor-specifically expressed and consequently could be a highly selective therapeutic target without side effects.

D. Small Interfering RNA (siRNA)

RNA interference (RNAi) phenomenon has been evaluated as a revolutionary discovery to enable silencing of specific gene expression⁷¹. The general mechanism is as follows: a double-stranded RNA with a specific sequence binds to Dicer protein which cleaves it around 21 nucleotides of RNA fragment. The resulting RNA fragment is complexed with RLC (RISC-loading complex) where the sense sequence of the double-stranded RNA fragment is cleaved. Once Argonaut2 (Ago2) forms an effective machinery with remaining proteins and around 21 nucleotide (nt) antisense RNA, it is called RISC (RNA-induced silencing complex) and cleaves the target mRNA at the center of duplex between siRNA and mRNA. Except microRNA there are two different types of RNAi tools. First is small interfering RNA (siRNA) which is chemically synthesized with 21nt length and jumps into RISC without a cleavage step by Dicer. Second is short hairpin

RNA (shRNA) which is cloned in the plasmid or viral vector construct to be expressed endogenously and subsequently to be processed by Dicer for the preparation of siRNA sequence⁷².

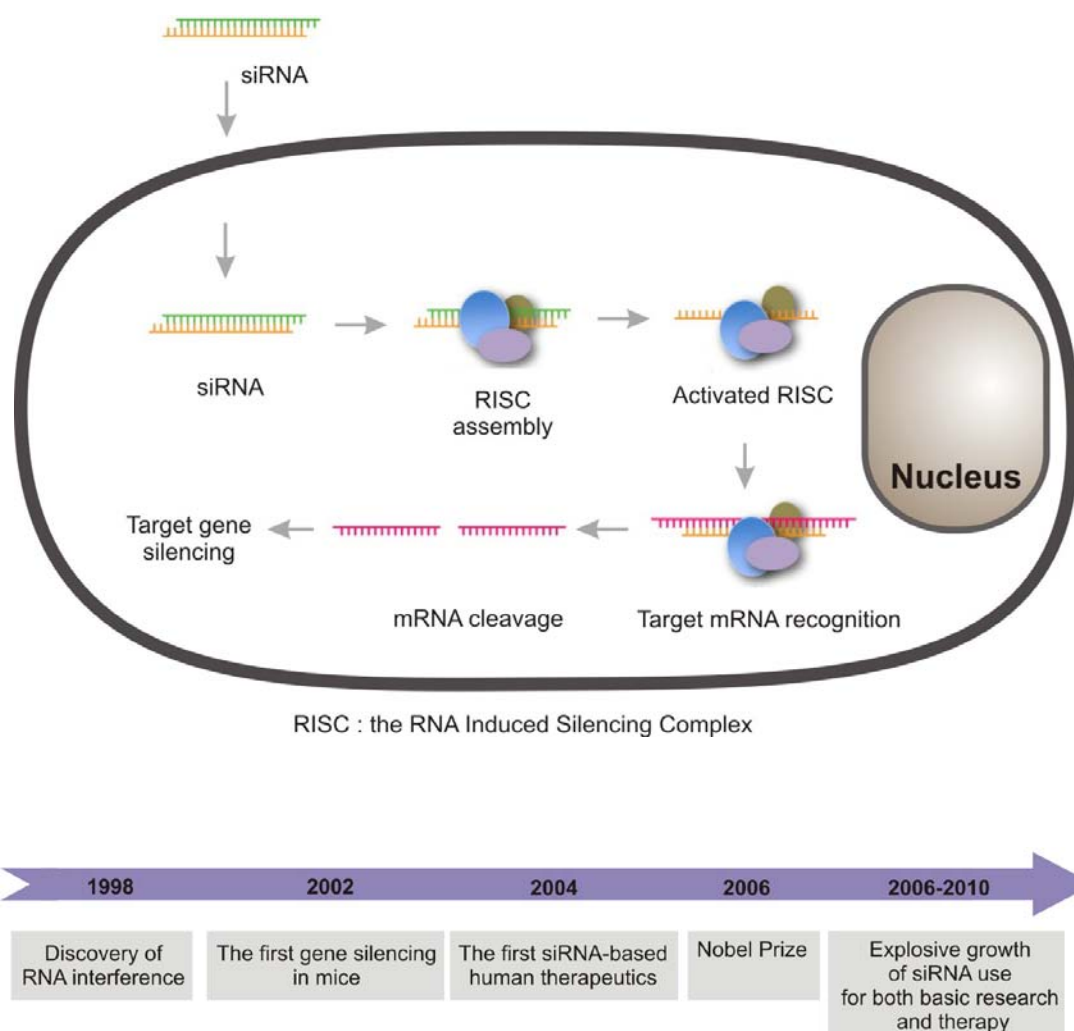


Figure I-5. Mechanism of RNA interference by siRNA

Adapted with the permission from ref. 77

Chemically synthesized siRNA can address the knockdown effect relatively easily and quickly by non-viral delivery tools such as cationic lipid-based methods (Lipofectamine-Invitrogen, XtremeGene-Roche)⁷³. However, because of limited concentration of siRNA in a cell, the knockdown efficiency keeps decreasing after 72-96 hours as cell population increases by cell division. It is known that the effective time window for siRNA is 7~8 days and it requires at least two days of transfection time to be delivered into the cytoplasm for the knockdown effect. Paradoxically, the transient time window and relatively easy delivery make siRNA one of the promising candidates for biological therapeutic reagents. On the other hand, shRNA needs to be engineered genetically for insertion into the vector system and to be transfected into the nucleus. Once it is transfected and placed into the nucleus successfully, the life time of shRNA is almost permanent because cellular system transcribes the sequence with its own protein machinery. However, it takes a lot of time and effort to insert the shRNA into the vector system such as lentivirus and to screen the properly transfected and stabilized cells^{74,75}.

For the preparation of high efficiency, the most effective sequence target should be exploited. Fortunately, several biotechnology companies supply the searching tool to find suitable candidates of siRNA and as-prepared siRNA with high knockdown efficiency for the gene with high demands such as green fluorescence protein (GFP). Once the sequence is determined, there are several options for the purification, duplexed form, amount, and chemical modification. One of the popular modifications is phosphorylation at the 5' of the antisense strand to stabilize the siRNA against nucleolytic degradation. Moreover, functional group, fluorescence dyes, and lipophilic group can be conjugated for the easy release, co-localization, and improved cellular uptake, etc. Most importantly is that most

modifications should be performed in a sense strand because it will be removed when it forms a RISC, and will not affect their activity. Especially, the 3' of antisense should be conserved the most⁷⁴.

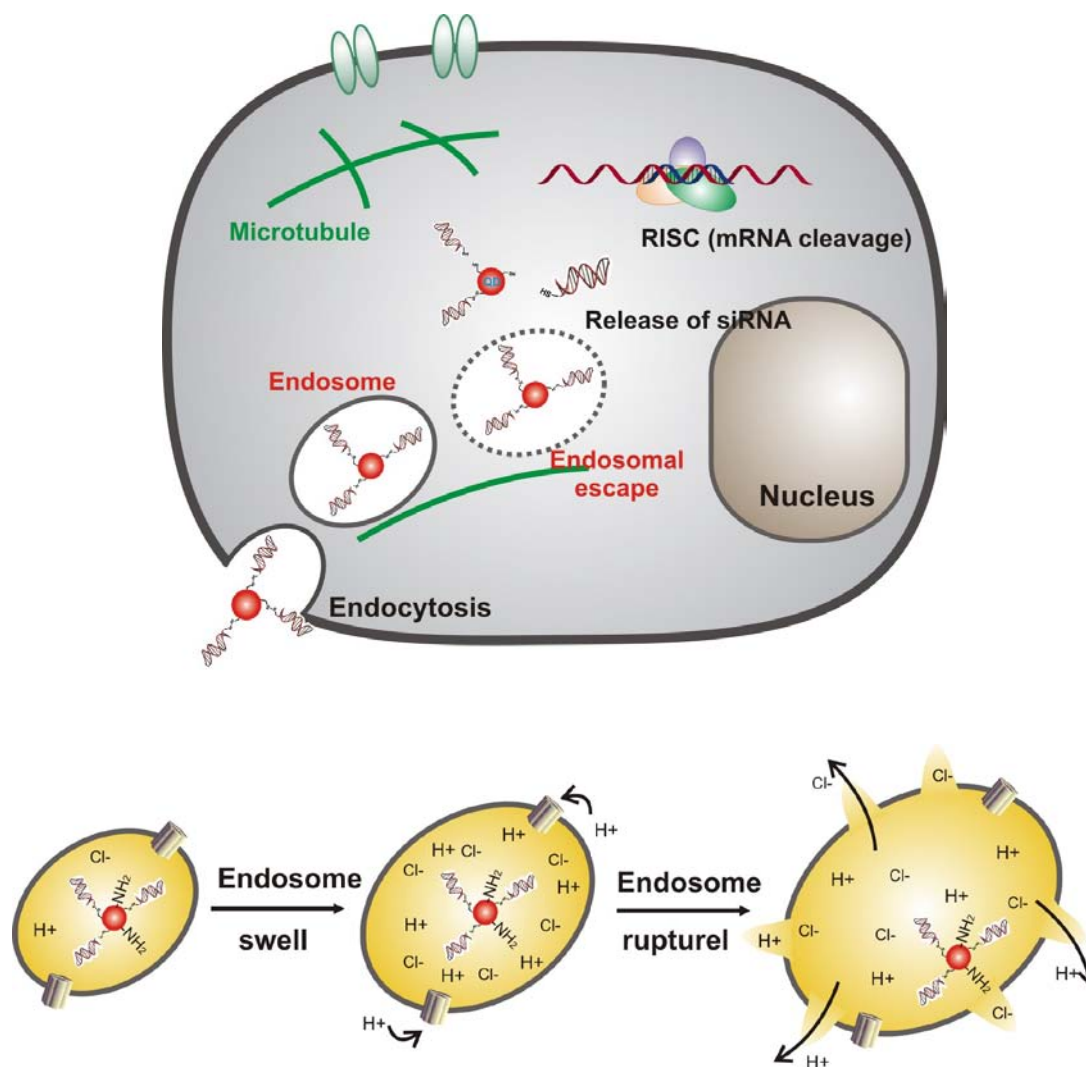


Figure I-6. Proton sponge effect and endosomal escape of nanocarriers

Adapted with the permission from ref. 79

One important issue is transfection mechanism and delivery tools. First, the cellular barrier against siRNA delivery is their repulsion by negative charges between extracellular interface of cell membrane and phosphate backbone of siRNA⁷⁵. The second one is the induction of internalization by pinocytosis, endocytosis, or receptor-mediated endocytosis because its size makes it impossible to penetrate the cell membrane. Once it is internalized, it should escape from the endosome to be transfected into the cytoplasm. There are several types of endosomes such as the early endosome and late endosome according to their pH value from about 6.5 to about 5.5. If siRNA fails to escape from the endosome properly, it will be secreted out of the cell called exocytosis or it will move to lysosome to be degraded⁷⁶.

Cationic lipid and polymer based siRNA delivery is one of the popular and well-established delivery methods. It has been reported that cationic lipid or polymer forms a nanometer size complex which enhances endocytosis, and resulting net charge which is represented N/P ratio – amine group/phosphate group - determines transfection efficiency⁷⁶. Biochemists proposed the “proton sponge effect” as a potent hypothesis⁷⁷. It describes that the amine group of cationic lipid or polymer absorbs protons from the endosome with a lower pH and it pumps in insufficient protons from the cytoplasm. Since the proton pump is coupled with sodium and potassium channels, it also brings in other ions and induces the unbalanced osmotic pressure. When a number of amine groups uncoupled with phosphate groups are beyond a certain threshold level, the endosome bursts and releases all the molecules into the cytoplasm. Based on this mechanism, cationic lipid and polymer based delivery has a cytotoxicity issue and there are significant efforts to

make polymers for siRNA transfection with high transfection efficiency and low cytotoxicity⁷⁸.

E. Silencing of the PI3K/AKT Signaling Pathway and its Signaling Crosstalk

As mentioned before, the PI3K/AKT signaling pathway is one of the most important signal transduction units inside a cell, responsible for cell survival, proliferation and differentiation. Owing to these intrinsic features, it is closely related with several key oncogenes in many cancers and has been a therapeutic target^{79,80}. Chemotherapeutic targets could be classified in the following four categories: receptor tyrosine kinase (RTK) - cytoplasmic domain of EGFR or HER2 is the target of Gefitinib and Erlotinib, PI3K is the target of Wortmannin and LY294002, AKT is the target of Perifosine and BKM120, and Rapamycin and Everolimus are inhibitors of mTOR that is a critical unit responsible for cellular nutrition availability, energy level, oxygen level, and mitogenic signaling for cell growth and proliferation^{81,82}.

As small molecule drugs silence this signaling pathway by inhibiting the function of key oncogenic proteins, siRNA can turn off this signal transduction by decreasing the expression level of target proteins. Because the silencing of the PI3K/AKT signaling pathway has been known not only to retard the rate of cancer cell proliferation but also to induce cancer cell apoptosis, this signal transduction route could be a promising target to utilize siRNA as a chemotherapeutic agent⁸³. In addition, siRNA and small drug molecules are complementary partners and intensively studied for the synergistic effect by delivering them together because their silencing mechanisms are different in a sense that drug

molecules inhibit as-expressed proteins but are relatively weak for newly synthesizing proteins in addition to multi-drug resistant mechanism of cancer cells.

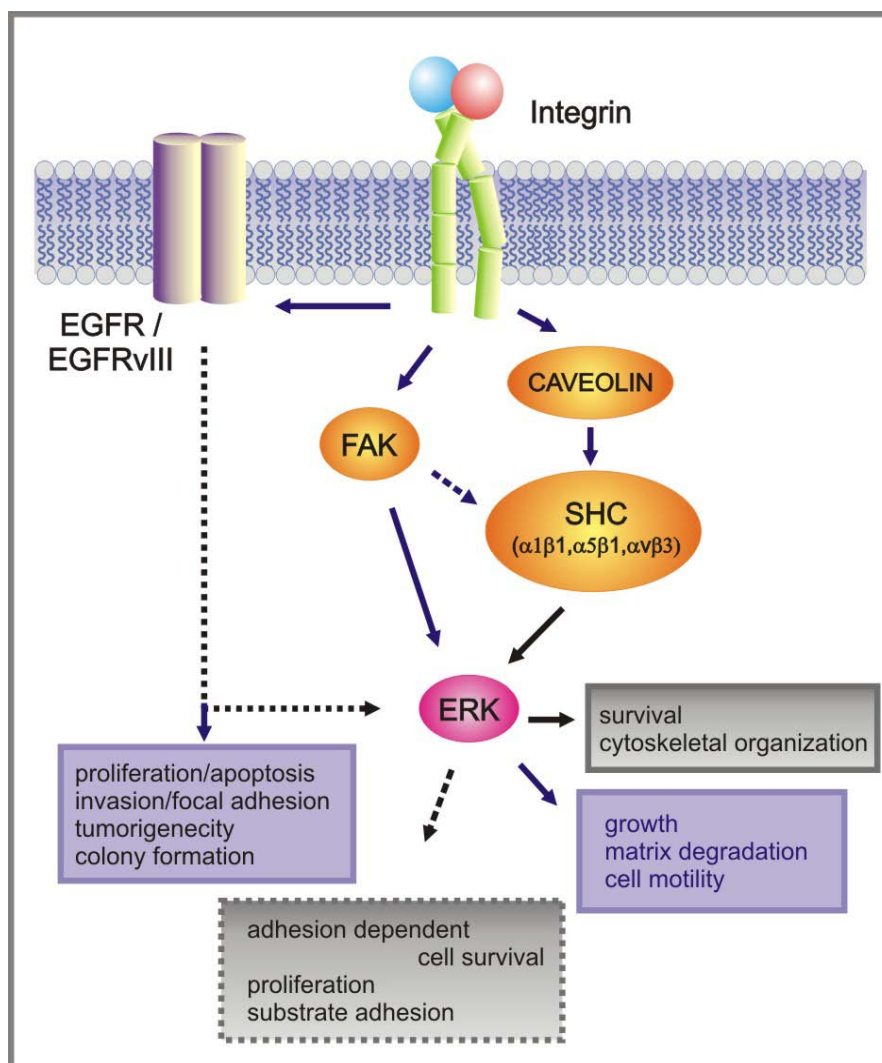


Figure I-7. Signaling crosstalk by FAK and ERK between EGFR and Integrin influencing cellular structural dynamics

Adapted with the permission from ref. 88

On the contrary, siRNA does the knockdown of mRNA without affecting as-expressed oncogenes. There are also several issues that the working time window and delivery mechanism are different between siRNA and drug molecules. In order to maximize the effect of combination treatment with siRNA and drug, various polymers have been developed for the controlled release and multi-functionality to overcome these obstacles for combined chemotherapy⁸⁴.

Each signaling pathway is interconnected with other signal transduction routes and forms complicated signaling networks. Therefore, after the PI3K/AKT signaling pathway is silenced, it accompanies other physiological change of cancer cells such as low invasion, depressed focal adhesion formation, and low cell cycle progression plus increased apoptosis and decreased cell proliferation^{85,86}. These phenotype changes are caused by the signaling network. It was reported that EGFR signaling regulation affects interactions with integrin and FAK (focal adhesion kinase) as well as Src kinase and Rap1, which leads to actin remodeling for cancer cell invasion and metastasis⁸⁷. In addition, EGFR communicates the ERK (extracellular signal-regulated kinase) signaling pathway which is responsible for substrate adhesion of cell, cell motility, and cytoskeletal organization^{88,89}.

With the comprehensive collection of the relationship between the PI3K/AKT signaling pathway and others, therapeutic targets could be beyond the induction of cancer cell death. For example, the silencing of the PI3K/AKT signaling pathway also generates the change of cytoskeleton formation and focal adhesion formation in addition to integrin expression level⁸⁶. It enables the practical study of cancer cell metastasis^{90,91}. Once their relationship becomes clear, delivery of dual siRNA against EGFR (EGFRvIII) and

FAK(integrin) could be developed as a therapeutic target for cancer cell migration and metastasis⁹¹.

F. References

- 1 Solanki, A., Kim, J. D. & Lee, K. B. Nanotechnology for regenerative medicine: nanomaterials for stem cell imaging. *Nanomedicine* **3**, 567-578, doi:10.2217/17435889.3.4.567 (2008).
- 2 Peer, D. *et al.* Nanocarriers as an emerging platform for cancer therapy. *Nature Nanotechnology* **2**, 751-760, doi:10.1038/nnano.2007.387 (2007).
- 3 Ferreira, L., Karp, J. M., Nobre, L. & Langer, R. New opportunities: The use of Nanotechnologies to manipulate and track stem cells. *Cell Stem Cell* **3**, 136-146, doi:10.1016/j.stem.2008.07.020 (2008).
- 4 Petros, R. A. & DeSimone, J. M. Strategies in the design of nanoparticles for therapeutic applications. *Nature Reviews Drug Discovery* **9**, 615-627, doi:10.1038/nrd2591 (2010).
- 5 Zamir, E., Lommerse, P. H. M., Kinkhabwala, A., Grecco, H. E. & Bastiaens, P. I. H. Fluorescence fluctuations of quantum-dot sensors capture intracellular protein interaction dynamics. *Nature Methods* **7**, 295-298, doi:10.1038/nmeth.1441 (2010).
- 6 Na, H. B., Song, I. C. & Hyeon, T. Inorganic Nanoparticles for MRI Contrast Agents. *Advanced Materials* **21**, 2133-2148, doi:10.1002/adma.200802366 (2009).
- 7 Yu, M. K. *et al.* Drug-loaded superparamagnetic iron oxide nanoparticles for combined cancer imaging and therapy in vivo. *Angewandte Chemie-International Edition* **47**, 5362-5365, doi:10.1002/anie.200800857 (2008).
- 8 Clapp, A. R., Goldman, E. R. & Mattoussi, H. Capping of CdSe-ZnS quantum dots with DHLA and subsequent conjugation with proteins. *Nature Protocols* **1**, 1258-1266, doi:10.1038/nprot.2006.184 (2006).
- 9 Susumu, K. *et al.* Enhancing the stability and biological functionalities of quantum dots via compact multifunctional ligands. *Journal of the American Chemical Society* **129**, 13987-13996, doi:10.1021/ja0749744 (2007).
- 10 Liu, W. *et al.* Compact biocompatible quantum dots functionalized for cellular imaging. *Journal of the American Chemical Society* **130**, 1274-1284, doi:10.1021/ja076069p (2008).

- 11 Uyeda, H. T., Medintz, I. L., Jaiswal, J. K., Simon, S. M. & Mattoussi, H. Synthesis of compact multidentate ligands to prepare stable hydrophilic quantum dot fluorophores. *Journal of the American Chemical Society* **127**, 3870-3878, doi:10.1021/ja044031w (2005).
- 12 Kim, B. *et al.* Tuning payload delivery in tumour cylindroids using gold nanoparticles. *Nature Nanotechnology* **5**, 465-472, doi:10.1038/nnano.2010.58 (2010).
- 13 Giljohann, D. A., Seferos, D. S., Prigodich, A. E., Patel, P. C. & Mirkin, C. A. Gene Regulation with Polyvalent siRNA-Nanoparticle Conjugates. *Journal of the American Chemical Society* **131**, 2072-+, doi:10.1021/ja808719p (2009).
- 14 Arvizo, R. R. *et al.* Effect of Nanoparticle Surface Charge at the Plasma Membrane and Beyond. *Nano Letters* **10**, 2543-2548, doi:10.1021/nl1011401 (2010).
- 15 Xiao, Y. *et al.* Anti-HER2 IgY antibody-functionalized single-walled carbon nanotubes for detection and selective destruction of breast cancer cells. *Bmc Cancer* **9**, doi:35110.1186/1471-2407-9-351 (2009).
- 16 Rosenthal, S. J., McBride, J., Pennycook, S. J. & Feldman, L. C. Synthesis, surface studies, composition and structural characterization of CdSe, core/shell and biologically active nanocrystals. *Surface Science Reports* **62**, 111-157, doi:10.1016/j.surfrep.2007.02.001 (2007).
- 17 Michalet, X. *et al.* Properties of fluorescent semiconductor nanocrystals and their application to biological labeling. *Single Molecules* **2**, 261-276 (2001).
- 18 Murray, C. B., Kagan, C. R. & Bawendi, M. G. Synthesis and characterization of monodisperse nanocrystals and close-packed nanocrystal assemblies. *Annual Review of Materials Science* **30**, 545-610 (2000).
- 19 Medintz, I. L., Uyeda, H. T., Goldman, E. R. & Mattoussi, H. Quantum dot bioconjugates for imaging, labelling and sensing. *Nature Materials* **4**, 435-446, doi:10.1038/nmat1390 (2005).
- 20 Cai, W. B. *et al.* Peptide-labeled near-infrared quantum dots for imaging tumor vasculature in living subjects. *Nano Letters* **6**, 669-676, doi:10.1021/nl052405t (2006).
- 21 Pinaud, F., Clarke, S., Sittner, A. & Dahan, M. Probing cellular events, one quantum dot at a time. *Nature Methods* **7**, 275-285, doi:10.1038/nmeth.1444 (2010).
- 22 Peng, X. G., Schlamp, M. C., Kadavanich, A. V. & Alivisatos, A. P. Epitaxial growth of highly luminescent CdSe/CdS core/shell nanocrystals with photostability

- and electronic accessibility. *Journal of the American Chemical Society* **119**, 7019-7029 (1997).
- 23 Peng, Z. A. & Peng, X. G. Formation of high-quality CdTe, CdSe, and CdS nanocrystals using CdO as precursor. *Journal of the American Chemical Society* **123**, 183-184 (2001).
 - 24 Qu, L. H., Peng, Z. A. & Peng, X. G. Alternative routes toward high quality CdSe nanocrystals. *Nano Letters* **1**, 333-337, doi:10.1021/nl015532 (2001).
 - 25 Qu, L. H., Yu, W. W. & Peng, X. P. In situ observation of the nucleation and growth of CdSe nanocrystals. *Nano Letters* **4**, 465-469, doi:10.1021/nl035211r (2004).
 - 26 Peng, X. G. Green chemical approaches toward high-quality semiconductor nanocrystals. *Chemistry-a European Journal* **8**, 335-339 (2002).
 - 27 Yu, W. W. & Peng, X. G. Formation of high-quality CdS and other II-VI semiconductor nanocrystals in noncoordinating solvents: Tunable reactivity of monomers. *Angew. Chem.-Int. Edit.* **41**, 2368-2371 (2002).
 - 28 Peng, X. G. & Thessing, J. in *Semiconductor Nanocrystals and Silicate Nanoparticles* Vol. 118 *Structure and Bonding* 79-119 (2005).
 - 29 Li, J. J. *et al.* Large-scale synthesis of nearly monodisperse CdSe/CdS core/shell nanocrystals using air-stable reagents via successive ion layer adsorption and reaction. *Journal of the American Chemical Society* **125**, 12567-12575, doi:10.1021/ja0363563 (2003).
 - 30 Yu, W. W., Qu, L. H., Guo, W. Z. & Peng, X. G. Experimental determination of the extinction coefficient of CdTe, CdSe, and CdS nanocrystals. *Chemistry of Materials* **15**, 2854-2860, doi:10.1021/cm034081k (2003).
 - 31 Jung, J. J. *et al.* Selective Inhibition of Human Brain Tumor Cells through Multifunctional Quantum-Dot-Based siRNA Delivery. *Angew. Chem.-Int. Edit.* **49**, 103-107, doi:10.1002/anie.200905126 (2010).
 - 32 Smith, B. R. *et al.* Real-time intravital imaging of RGD-quantum dot binding to luminal endothelium in mouse tumor neovasculature. *Nano Letters* **8**, 2599-2606, doi:10.1021/nl80141f (2008).
 - 33 Cai, W. B. & Chen, X. Y. Preparation of peptide-conjugated quantum dots for tumor vasculature-targeted imaging. *Nature Protocols* **3**, 89-96, doi:10.1038/nprot.2007.478 (2008).

- 34 Jun, Y. W., Seo, J. W. & Cheon, A. Nanoscaling laws of magnetic nanoparticles and their applicabilities in biomedical sciences. *Accounts Chem. Res.* **41**, 179-189, doi:10.1021/ar700121f (2008).
- 35 Mornet, S., Vasseur, S., Grasset, F. & Duguet, E. Magnetic nanoparticle design for medical diagnosis and therapy. *Journal of Materials Chemistry* **14**, 2161-2175, doi:10.1039/b402025a (2004).
- 36 Jun, Y. W., Choi, J. S. & Cheon, J. Heterostructured magnetic nanoparticles: their versatility and high performance capabilities. *Chemical Communications*, 1203-1214, doi:10.1039/b614735f (2007).
- 37 Lu, A. H., Salabas, E. L. & Schuth, F. Magnetic nanoparticles: Synthesis, protection, functionalization, and application. *Angewandte Chemie-International Edition* **46**, 1222-1244, doi:10.1002/anie.200602866 (2007).
- 38 Jun, Y. W., Lee, J. H. & Cheon, J. Chemical design of nanoparticle probes for high-performance magnetic resonance imaging. *Angewandte Chemie-International Edition* **47**, 5122-5135, doi:10.1002/anie.200701674 (2008).
- 39 Weissleder, R. *et al.* Superparamagnetic iron-oxide-pharmacokinetics and toxicity. *Am. J. Roentgenol.* **152**, 167-173 (1989).
- 40 Jung, C. W. & Jacobs, P. Physical and chemical-properties of superparamagnetic iron-oxide MR contrast agents - Ferumoxides, ferumoxtran, Ferumoxsil. *Magn. Reson. Imaging* **13**, 661-674 (1995).
- 41 Josephson, L., Tung, C. H., Moore, A. & Weissleder, R. High-efficiency intracellular magnetic labeling with novel superparamagnetic-tat peptide conjugates. *Bioconjugate Chem.* **10**, 186-191 (1999).
- 42 Reimer, P. *et al.* Clinical-results with Resovist - A phase-2-clinical-trial. *Radiology* **195**, 489-496 (1995).
- 43 Lee, J. H. *et al.* Artificially engineered magnetic nanoparticles for ultra-sensitive molecular imaging. *Nat. Med.* **13**, 95-99, doi:10.1038/nm1467 (2007).
- 44 Seo, W. S. *et al.* FeCo/graphitic-shell nanocrystals as advanced magnetic-resonance-imaging and near-infrared agents. *Nat. Mater.* **5**, 971-976, doi:10.1038/nmat1775 (2006).
- 45 Desvaux, C. *et al.* Multimillimetre-large superlattices of air-stable iron-cobalt nanoparticles. *Nat. Mater.* **4**, 750-753, doi:10.1038/nmat1480 (2005).
- 46 Chaubey, G. S. *et al.* Synthesis and stabilization of FeCo nanoparticles. *Journal of the American Chemical Society* **129**, 7214-+, doi:10.1021/ja0708969 (2007).

- 47 Yang, J. *et al.* Multifunctional magneto-polymeric nanohybrids for targeted detection and synergistic therapeutic effects on breast cancer. *Angewandte Chemie-International Edition* **46**, 8836-8839, doi:10.1002/anie.200703554 (2007).
- 48 Davis, M. E. & Brewster, M. E. Cyclodextrin-based pharmaceuticals: Past, present and future. *Nature Reviews Drug Discovery* **3**, 1023-1035, doi:10.1038/nrd1576 (2004).
- 49 MacKay, J. A. *et al.* Self-assembling chimeric polypeptide-doxorubicin conjugate nanoparticles that abolish tumours after a single injection. *Nature Materials* **8**, 993-999, doi:10.1038/nmat2569 (2009).
- 50 Wang, H. *et al.* A Supramolecular Approach for Preparation of Size-Controlled Nanoparticles. *Angewandte Chemie-International Edition* **48**, 4344-4348, doi:10.1002/anie.200900063 (2009).
- 51 Wang, S. T. *et al.* Photothermal Effects of Supramolecularly Assembled Gold Nanoparticles for the Targeted Treatment of Cancer Cells. *Angewandte Chemie-International Edition* **49**, 3777-3781, doi:10.1002/anie.201000062 (2010).
- 52 Yang, F. *et al.* Gene delivery to human adult and embryonic cell-derived stem cells using biodegradable nanoparticulate polymeric vectors. *Gene Therapy* **16**, 533-546, doi:10.1038/gt.2008.182 (2009).
- 53 Khemtong, C., Kessinger, C. W. & Gao, J. M. Polymeric nanomedicine for cancer MR imaging and drug delivery. *Chemical Communications*, 3497-3510, doi:10.1039/b821865j (2009).
- 54 Guthi, J. S. *et al.* MRI-Visible Micellar Nanomedicine for Targeted Drug Delivery to Lung Cancer Cells. *Molecular Pharmaceutics* **7**, 32-40, doi:10.1021/mp9001393 (2010).
- 55 Jere, D. *et al.* Poly(beta-amino ester) as a carrier for si/shRNA delivery in lung cancer cells. *Biomaterials* **29**, 2535-2547, doi:10.1016/j.biomaterials.2008.02.018 (2008).
- 56 Jere, D. *et al.* Degradable polyethylenimines as DNA and small interfering RNA carriers. *Expert Opinion on Drug Delivery* **6**, 827-834, doi:10.1517/17425240903029183 (2009).
- 57 Zugates, G. T., Anderson, D. G., Little, S. R., Lawhorn, I. E. B. & Langer, R. Synthesis of poly(beta-amino ester)s with thiol-reactive side chains for DNA delivery. *Journal of the American Chemical Society* **128**, 12726-12734, doi:10.1021/ja061570n (2006).

- 58 Lee, J. S. *et al.* Gold, Poly(beta-amino ester) Nanoparticles for Small Interfering RNA Delivery. *Nano Letters* **9**, 2402-2406, doi:10.1021/nl9009793 (2009).
- 59 Yamanaka, R. & Saya, H. Molecularly Targeted Therapies for Glioma. *Annals of Neurology* **66**, 717-729, doi:10.1002/ana.21793 (2009).
- 60 Cully, M., You, H., Levine, A. J. & Mak, T. W. Beyond PTEN mutations: the PI3K pathway as an integrator of multiple inputs during tumorigenesis. *Nature Reviews Cancer* **6**, 184-192, doi:10.1038/nrc1819 (2006).
- 61 Fan, Q. W. & Weiss, W. A. RNA interference against a glioma-derived allele of EGFR induces blockade at G(2)M. *Oncogene* **24**, 829-837, doi:10.1038/sj.onc.1208227 (2005).
- 62 Engelman, J. A. Targeting PI3K signalling in cancer: opportunities, challenges and limitations. *Nature Reviews Cancer* **9**, 550-562, doi:10.1038/nrc2664 (2009).
- 63 Liu, P. X., Cheng, H. L., Roberts, T. M. & Zhao, J. J. Targeting the phosphoinositide 3-kinase pathway in cancer. *Nature Reviews Drug Discovery* **8**, 627-644, doi:10.1038/nrd2926 (2009).
- 64 Mischel, P. S. & Cloughesy, T. Using molecular information to guide brain tumor therapy. *Nature Clinical Practice Neurology* **2**, 232-233, doi:10.1038/ncpneuro0145 (2006).
- 65 Wang, M. Y. *et al.* Mammalian target of rapamycin inhibition promotes response to epidermal growth factor receptor kinase inhibitors in PTEN-Deficient and PTEN-intact glioblastoma cells. *Cancer Research* **66**, 7864-7869, doi:10.1158/0008-5472.can-04-4392 (2006).
- 66 Wong, K. K., Engelman, J. A. & Cantley, L. C. Targeting the PI3K signaling pathway in cancer. *Current Opinion in Genetics & Development* **20**, 87-90, doi:10.1016/j.gde.2009.11.002 (2010).
- 67 Mellinghoff, I. K. Molecular determinants of the response of glioblastomas to EGFR kinase inhibitors (vol 353, pg 2012, 2005). *New England Journal of Medicine* **354**, 884-884 (2006).
- 68 Mellinghoff, I. K., Cloughesy, T. F. & Mischel, P. S. PTEN-mediated resistance to epidermal growth factor receptor kinase inhibitors. *Clinical Cancer Research* **13**, 378-381, doi:10.1158/1078-0432.ccr-06-1992 (2007).
- 69 Lesniak, M. S. & Brem, H. Targeted therapy for brain tumours. *Nature Reviews Drug Discovery* **3**, 499-508, doi:10.1038/nrd1414 (2004).

- 70 Luo, J., Solimini, N. L. & Elledge, S. J. Principles of Cancer Therapy: Oncogene and Non-oncogene Addiction. *Cell* **136**, 823-837, doi:10.1016/j.cell.2009.02.024 (2009).
- 71 Kim, V. N. RNA interference in functional genomics and medicine. *Journal of Korean Medical Science* **18**, 309-318 (2003).
- 72 Dykxhoorn, D. M. & Lieberman, J. Running interference: Prospects and obstacles to using small interfering RNAs as small molecule drugs. *Annual Rev. of Biomed. Engineering* **8**, 377-402, doi:10.1146/annurev.bioeng.8.061505.095848 (2006).
- 73 McNamara, J. O. *et al.* Cell type-specific delivery of siRNAs with aptamer-siRNA chimeras. *Nature Biotechnology* **24**, 1005-1015, doi:10.1038/nbt1223 (2006).
- 74 Lee, J. H. *et al.* All-in-One Target-Cell-Specific Magnetic Nanoparticles for Simultaneous Molecular Imaging and siRNA Delivery. *Angewandte Chemie-International Edition* **48**, 4174-4179, doi:10.1002/anie.200805998 (2009).
- 75 Kim, S. S., Garg, H., Joshi, A. & Manjunath, N. Strategies for targeted nonviral delivery of siRNAs in vivo. *Trends in Molecular Medicine* **15**, 491-500, doi:10.1016/j.molmed.2009.09.001 (2009).
- 76 Elbakry, A. *et al.* Layer-by-Layer Assembled Gold Nanoparticles for siRNA Delivery. *Nano Letters* **9**, 2059-2064, doi:10.1021/nl9003865 (2009).
- 77 Yezhelyev, M. V., Qi, L. F., O'Regan, R. M., Nie, S. & Gao, X. H. Proton-sponge coated quantum dots for siRNA delivery and intracellular imaging. *Journal of the American Chemical Society* **130**, 9006-9012, doi:10.1021/ja800086u (2008).
- 78 Uprichard, S. L. The therapeutic potential of RNA interference. *Febs Letters* **579**, 5996-6007, doi:10.1016/j.febslet.2005.08.004 (2005).
- 79 Lal, A. *et al.* Mutant epidermal growth factor receptor up-regulates molecular effectors of tumor invasion. *Cancer Research* **62**, 3335-3339 (2002).
- 80 Ning, Y. *et al.* Down-regulation of integrin alpha(2) surface expression by mutant epidermal growth factor receptor (EGFRvIII) induces aberrant cell spreading and focal adhesion formation. *Cancer Research* **65**, 9280-9286, doi:10.1158/0008-5472.can-05-0407 (2005).
- 81 Vogel, V. & Sheetz, M. Local force and geometry sensing regulate cell functions. *Nature Reviews Molecular Cell Biology* **7**, 265-275, doi:10.1038/nrm1890 (2006).
- 82 Kim, K. *et al.* Epidermal growth factor receptor vIII expression in U87 glioblastoma cells alters their proteasome composition, function, and response to

- irradiation. *Molecular Cancer Research* **6**, 426-434, doi:10.1158/1541-7786.mcr-07-0313 (2008).
- 83 Arwert, E. *et al.* Visualizing the dynamics of EGFR activity and antiglioma therapies in vivo. *Cancer Research* **67**, 7335-7342, doi:10.1158/0008-5472.can-07-0077 (2007).
 - 84 Yamoutpour, F. *et al.* Gene silencing for epidermal growth factor receptor variant III induces cell-specific cytotoxicity. *Molecular Cancer Therapeutics* **7**, 3586-3597, doi:10.1158/1535-7163.mct-08-0653 (2008).
 - 85 Van Trappen, P. O. & Pepper, M. S. Lymphatic dissemination of tumour cells and the formation of micrometastases. *Lancet Oncology* **3**, 44-52 (2002).
 - 86 Kuphal, S., Bauer, R. & Bosserhoff, A. K. Integrin signaling in malignant melanoma. *Cancer and Metastasis Reviews* **24**, 195-222 (2005).
 - 87 Joyce, J. A. & Pollard, J. W. Microenvironmental regulation of metastasis. *Nature Reviews Cancer* **9**, 239-252, doi:10.1038/nrc2618 (2009).
 - 88 Ricono, J. M. *et al.* Specific Cross-talk between Epidermal Growth Factor Receptor and Integrin alpha(v)beta(5) Promotes Carcinoma Cell Invasion and Metastasis. *Cancer Research* **69**, 1383-1391, doi:10.1158/0008-5472.can-08-3612 (2009).
 - 89 Ulrich, T. A., Pardo, E. M. D. & Kumar, S. The Mechanical Rigidity of the Extracellular Matrix Regulates the Structure, Motility, and Proliferation of Glioma Cells. *Cancer Research* **69**, 4167-4174, doi:10.1158/0008-5472.can-08-4859 (2009).
 - 90 Duneau, A. L. *et al.* Cell adhesion molecules for targeted drug delivery. *Journal of Pharmaceutical Sciences* **95**, 1856-1872, doi:10.1002/jps.20676 (2006).
 - 91 Desgrosellier, J. S. & Cheres, D. A. Integrins in cancer: biological implications and therapeutic opportunities. *Nature Reviews Cancer* **10**, 9-22, doi:10.1038/nrc2748 (2010).

CHAPTER II

OVERALL OBJECTIVES

Nanoscience confronts new challenges from academic or industrial fields because it is required to contribute to novel application and create a new science at the interface of energy, biology, and medicine by itself beyond the proof-of-principle. One promising approach is to apply nanoscience to cancer therapy and regenerative medicine. Nanoparticles can be used for imaging modality and delivery of therapeutics as well as targeting molecules. In addition, the modulation of the microenvironment such as geometries and chemical properties enables us to investigate cellular behavior in a quantitative manner for cancer therapy and clinical applications.

In this comprehensive study, I have explored the potential of multimodal nanoparticles as excellent imaging probes and delivery vehicles and therapeutic agents with specific targeting at both the cellular and in vivo levels.

First, quantum dots have been utilized for the targeted delivery of siRNA against EGFRvIII to silence PI3K/AKT signaling to suppress the proliferation of brain tumor cells (GBM). Because QDs have strong fluorescence intensity, both delivery status of siRNA and targeting by RGD/TAT peptide can be synchronized with the fluorescence color.

Second, QDs have a limitation for the extension to in vivo application because of their intrinsic cytotoxicity by cadmium and selenium. Therefore, we synthesized high performance FeCo/C (iron cobalt with graphite shell) magnetic nanoparticles for the highly sensitive MR imaging and hyperthermia agent to induce cell death by local-heating under an AC magnetic field. We further show the delivery of siRNA against EGFRvIII conjugated with FeCo/C MNPs and the possibility to be combined with hyperthermia.

Third, in order to strengthen the multifunctionality in addition to the multimodality tested previous studies, we designed a poly(b-amino ester) (PBAE)-based polymer-MNP

nanohybrid platform which is closer to clinical application as a theragnostic. Anticancer drugs units are covalently linked to the PBAE backbone and oligoamines attached the PBAE backbone can be used not only for conjugating targeting molecules such as antibody and cRGD but also for siRNA non-covalently. Therefore, FeCo/C MNPs enable the diagnosis of specific cancer and to monitor its shrinkage by released anticancer drugs and siRNA. A cellular studies were performed here using a couple of effective combinations for drug and siRNA: knockdown of multidrug resistance genes, HER 2 gene or EGFRvIII gene.

In addition, the quantitative systems based on 'top-down' approach for cell metastasis are established because the knockdown of oncogenes such as EGFRvIII and HER2 accompany the change of focal adhesion formation and cell migration, and thus lacks a systematic way to evaluate the change. We designed the microcontact printed patterns and microfluidics to evaluate the effect of gene silencing and to connect phenotype change.

CHAPTER III

SELECTIVE INHIBITION OF HUMAN BRAIN TUMOR CELLS THROUGH MULTIFUNCTIONAL QUANTUM DOT-BASED siRNA DELIVERY

A. Introduction

One of the most promising new chemotherapeutic strategies is the RNA interference (RNAi)-based approach, wherein small double-stranded RNA molecules can sequence-specifically inhibit the expression of targeted oncogenes.^{1,2} In principle, this method has high specificity and broad applicability for chemotherapy. For example, the small interfering RNA (siRNA) strategy enables manipulation of key oncogenes that modulate signaling pathways and thereby regulate the behavior of malignant tumor cells. To harness the full potential of this approach, the prime requirements are to deliver the siRNA molecules with high selectivity and efficiency into tumor cells and to monitor both siRNA delivery and the resulting knock-down effects at the single cell level. Although several approaches such as polymer- and nanomaterial-based methods³⁻⁶ have been attempted, limited success has been achieved for delivering siRNA into the target tumor cells. Moreover, these types of approaches mainly focus on the enhancement of transfection efficiency, knock-down of non-oncogenes (e.g. green fluorescent protein (GFP)), and the use of different nanomaterials such as quantum dots (QDs), iron oxide nanoparticles, and gold nanoparticles.⁷⁻¹² Therefore, to narrow the gap between current nanomaterial-based siRNA delivery and chemotherapies, there is a clear need to develop methods for target-oriented delivery of siRNA^{13,14}, for further monitoring the effects of siRNA-mediated target gene silencing via molecular imaging probes⁸, and for investigating the corresponding up/down regulation of signaling cascades.¹⁵ Perhaps most importantly, to begin the development of the necessary treatment modalities, the nanomaterial-based siRNA delivery strategies must be demonstrated on oncogenes involved in cancer pathogenesis

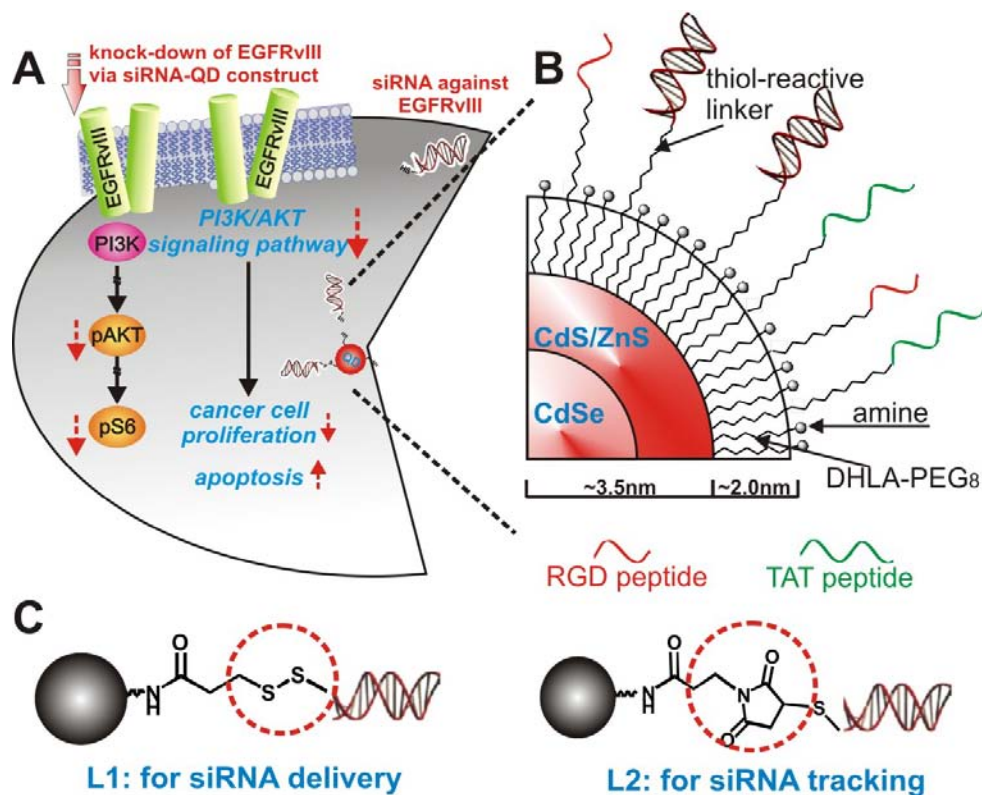


Figure III-1. (A): Quantum dots as a multi-functional nanoplatform to deliver siRNA and to elucidate of EGFRvIII- knockdown effect of PI3K signaling pathway in U87-EGFRvIII (B): Detailed structural information of multifunctional siRNA-QDs (C): Two different strategies for the siRNA-QD conjugate. (L1) Linker for attaching siRNA to QDs through a disulfide linkage which was easily reduced within the cells to release the siRNA. (L2) Linker for covalently conjugating siRNA to QDs which enabled tracking of siRNA-QDs within the cells. Copyright Wiley-VCH Verlag GmbH & Co. KGaA. Reproduced with the permission of Ref. 49

Herein, we describe the synthesis and target-specific delivery of multifunctional siRNA-QD constructs for selectively inhibiting the expression of epidermal growth factor receptor variant III (EGFRvIII) in target human U87 glioblastoma cells, and subsequently monitoring the resulting down-regulated signaling pathway with high efficiency.¹⁶

Glioblastoma multiforme (GBM) is the most malignant, invasive, and difficult-to-treat primary brain tumor. Successful treatment of GBM is rare with a mean survival of only 10-12 months.^{17,18} EGFRvIII, the key growth factor receptor triggering cancer cell proliferation in many cancer diseases such as brain tumors and breast cancer, is a constitutively active mutant of EGFR which is expressed in only human GBM and several other malignant cancers, but not in normal healthy cells (Figure 1A).^{19,20} We targeted EGFRvIII, since it has been known that knock-down of this gene is one of the most effective ways to down-regulate the PI3K/AKT signaling pathway, a key signal cascade for cancer cell proliferation and apoptosis.^{15,21,22} Hence by targeting EGFRvIII, our multi-functional nanoparticle-based siRNA delivery strategy could potentially minimize the side effects caused by conventional chemotherapies, specifically immune suppression, while significantly improving the efficacy of chemotherapy against GBM.

B. Materials and Methods

1. Synthesis of QD conjugates with siRNA

The siRNA molecules for EGFP and EGFRvIII containing 5' thiol group were purchased from Dharmacon and Invitrogen respectively. The siRNA for EGFP was designed as follows; Sense sequence was 5'-thiol-GGCUACGUCCAGGAGCGCACC and antisense sequence was 5'-phosphate-UGCGCUCCUGGACGUAGCCUU. For the knockdown of EGFRvIII, 5'-thiol-GAAAGGUAAUUAUGUGGUGdTdT (sense) and 5'-phosphate-CACCACAUAUUAACCUUUCdTdT (antisense) were used. QDs in the PBS were mixed with 1000 fold excess of the cross linker, MPPf and PTPPf, for one hour. After removing the unreacted linkers by ultracentrifugation, siRNA molecules were coupled to QDs by mixing together for one hour. After the conjugation, free siRNA was removed using ultracentrifugation. For the quantification of ratio of QD and siRNA, the siRNA linked to QDs via PTPPf (disulfide bond) were treated with DTT for one hour. After centrifugation, the supernatant was analyzed under UV at 260 nm quantifying the siRNA detached from QDs. By determining the concentration of QDs in the same volume at the first absorption peak²³, the siRNA molecules per QD were estimated. For the conjugation of HIV-Tat(CYGRKKRRQRRR) and RGD(RGDC) to siRNA-QDs, the same method as that used to conjugate siRNA to QD was used with the ratio of 1:10:10 (siRNA:RGD:HIV-Tat).

2. Cell culture of U87-EGFP and U87 EGFRvIII

Cells were cultured in the following growth media: DMEM (Dulbecco's modified Eagle's medium) with high glucose (Invitrogen), 10% Fetal Bovine Serum (FBS), 1%

streptomycin-penicillin, 1% glutamax (Invitrogen), and selection markers, G418 (100 μ g/ml) and hygromycin B (30 μ g/ml) for U87-EGFP and U87-EGFRvIII respectively. For the knockdown experiment, passaged cells were prepared to 40-60% confluency in 96-well plates. For the knockdown experiment and cell viability assay, media was exchanged with serum-free basal media (150 μ l) and siRNA-QDs solution (30 μ l) with the cationic lipid based transfection reagent, X-tremeGENE (0.4 μ l, Roche), was added after 20-30 minutes. After incubation for 12 hours, media was exchanged with normal media. Fluorescence measurement and cellular assays were performed after 48-96 hours from the starting point. Once intensity of EGFP was decreased, it was trypsinized and co-cultured with control U87-EGFP (1:1 ratio) in 48-well plates for direct comparison of knockdown level. Cells were washed with DPBS and fixed with 2-4% paraformaldehyde solution for long term storage at 4°C.

3. Targeted delivery of siRNA-QDs

U87-EGFP cells were co-cultured with control cells (or control neuroblastomas or neuroendocrine tumor), which are PC12 and SK-N-BE(2)C. Each control cell was passaged in 96 well plates, and 6 - 8 hours later U87-EGFP cells were co-cultured. Cell culture media for PC12 and U87 well plate was a mixture of DMEM, 10% horse serum, 5% FBS, and 1% streptomycin-penicillin. For U87 cells, DMEM, 10% FBS, and 1% streptomycin-penicillin was used as a culture media. F12 and MEM mixture (1:1), 10% FBS, and 1% streptomycin-penicillin were used to prepare the media for SK-N-BE(2)C. For the delivery of HIV-tat and RGD peptide conjugated siRNA-QDs, media was exchanged with serum free DMEM or Opti-MEM media. After adding the QD solution,

the cells were incubated for 6 – 8 hrs. The media was removed and washed with serum free media. Fluorescence images were taken after replacing the media with regular media.

4. Transmission electron microscopy

U87-EGFP transfected with siRNA-QDs samples were prepared using the Spurr's kit (EMS, Hatfield, PA). The images were obtained using the TEM (JEOL 100CX TEM).

5. Fluorescence microscopy

Cells in well plates were washed with DMEM and refilled with normal media. For the fluorescence, DIC, and phase contrast images were obtained using the Zeiss Axio observer inverted epifluorescence microscope. Each image was captured with different channels and focus. Images were processed and overlapped using Image-Pro (MediaCybernetics) and ImageJ (NIH).

6. Western blotting analysis

Cells were lysed with RIPA buffer (Thermo scientific, Rockford, IL) with protease inhibitor cocktail (Sigma-Aldrich) and phosphates inhibitor cocktail I, II (Sigma-Aldrich). After centrifugation, cell lysates were assayed for protein concentration using the Bio-Rad protein assay kit (Bio-Rad, Hercules, CA). Proteins (20 µg) were separated in 10% SDS polyacrylamide gels by electrophoresis, then transferred to a nitrocellulose membrane and subjected to immunoblotting. The following primary antibodies were used; polyclonal rabbit anti-human EGFRvIII (Spring Bioscience, Pleasanton, CA), polyclonal mouse anti-human EGFR (Santa Cruz Biotechnology, Santa

Cruz, CA), monoclonal mouse anti-human S6 (Santa Cruz Biotechnology) and monoclonal mouse anti-human phospho-S6 (Ser235/236) (Santa Cruz Biotechnology). Horse radish peroxidase (HRP)-conjugated polyclonal anti-mouse IgG and anti-rabbit IgG were used as the secondary antibodies. Immunoreactive bands were detected with the enhanced chemiluminescence (ECL) kit (GE Healthcare, Piscataway, NJ)

C. Results and Discussion

1. The Multifunctional QD platform for delivery and tracking of siRNA

I prepared two types of siRNA-QD conjugates, one for siRNA delivery and the other for siRNA tracking (Figure 1B and C). Core-shell CdSe/CdS/ZnS QDs with a 7 nm diameter were synthesized.^{24,25} The QDs were coated with trioctyl-phosphine oxide (TOPO) or hexadecylamine (HDA). In order to make the QD constructs water-soluble and suitable for conjugating with siRNA, we displaced these hydrophobic ligands with a dihydrolipoic acid (DHLA) derivatized with an amine terminated poly(ethylene glycol) (PEG) spacer. The expectation was that the dithiol moiety would provide strong coordination to the QD surface and increase stability in aqueous media, the PEG spacer would increase water solubility and reduce non-specific binding, and the amine group would enable conjugation to the siRNA element.^{26,27} The TEM image of DHLA-PEG₈-amine coated showed that the average size of the ligand-exchanged QD platform and its stability in Figure 2A. Two bifunctional linkers were synthesized and evaluated for siRNA conjugation. Linker L1, PTPPf [3-(2-pyridyl)-dithiopropionic acid pentafluorophenyl ester], was designed to release siRNA upon cellular entry through cleavage of the disulfide linkage, through enzymatic reduction or ligand-exchange (e.g. glutathione).²⁸⁻³⁰ Linker L2, MPPF (3-maleimidopropionic acid pentafluorophenyl ester), was designed to be more robust, thereby enabling evaluation of cellular uptake and localization of the siRNA construct within the cellular compartments.³¹

The bifunctional linker system on the QDs was verified using fluorescence resonance energy transfer (FRET) in Figure 2B. The FRET signal between the QDs and the attached dye-conjugated molecule is optimally detected when the distance between

the two is between 1-10 nm. If the signal is obtained we can conclude that the molecule is attached to the QD through the bifunctional linker via a disulfide linkage. Alexa 647 dye conjugated biomolecules with a thiol (-SH) group were attached to QDs through the bifunctional linker. When the Alexa 647-QD system was excited at 400 nm, Alexa 647 was not supposed to emit photons because this wavelength is out of the range of Alexa 647's direct excitation. However, we observed two different emission peaks at 400 nm excitation, which indicated that there was an energy transfer process (FRET) from the QD to Alexa 647 due to the confined distance between them (1-10nm range). We were therefore able to verify that the bifunctional linker efficiently conjugated two different molecules.

The final design component was to functionalize the construct for tumor cell-selective transfection. For this purpose two functional peptides, thiol-modified RGD peptide and thiol-modified HIV-Tat derived peptide, were attached to the siRNA-QDs via the conjugation methods described above. Brain tumor cells (U87 and U87-EGFRvIII) overexpress the integrin receptor protein $\alpha_v\beta_3$, which strongly binds to the RGD binding domain.³² RGD functionalized siRNA-QDs selectively accumulate in brain tumor cells *in vitro*, and can be tracked by fluorescence microscopy.³³ In addition, the HIV-Tat peptide enables efficient transfection of siRNA-QDs in cells when directly attached to the QD surface.^{34,35} The density of siRNA on the QDs and the ratio between siRNA strands and peptides were optimized for gene knockdown. It was found that the density of 10 siRNAs/per nanoparticle and the ratio of 1:10 (siRNA: each peptide) was in close agreement with literature values⁸, and was optimal for knocking down the target genes (EGFP and EGFRvIII) overexpressed in our U87 cell lines.

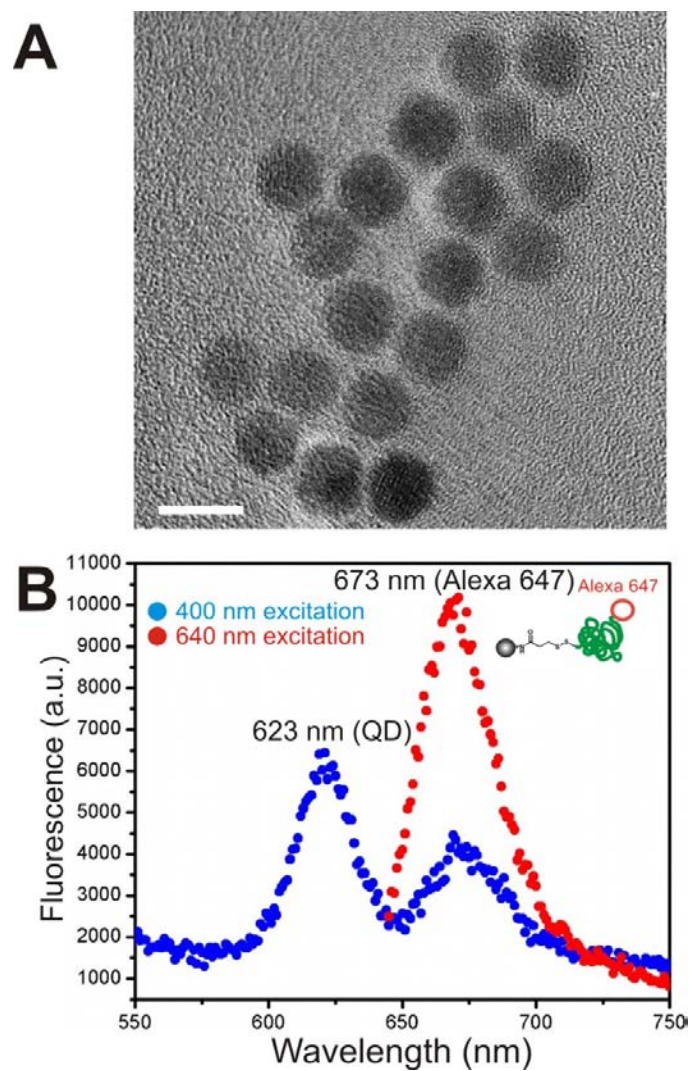


Figure III-2. (A): TEM image of DHLA-PEG₈-amine coated CdSe/CdS/ZnS core-shell QDs (scale bar = 10nm) (B): Analysis of the attachment of siRNA and RGD/HIV-Tat peptides.

1. 1. Synthesis of CdSe/CdS/ZnS Core-Shell QDs

CdSe cores are synthesized using the method developed by Peng *et al.*³⁶⁻³⁹ CdO and stearic acid is heated around 220°C until it becomes colorless. After Trioctylbutyl phosphine(TOPO), Hexadecylamine(HDA), and 1-octadecne(ODE) are added and heated up to 280°C, selenium solution which is prepared with selenium, tributylphosphine (TBP), and ODE in glove box, is injected (quickly). Growth temperature is fixed to 260°C and reaction stops by cooling down when it reaches desired size. By adjusting growing time, green (545nm) and red (580nm) colored QDs are obtained. The growing of QD core and resulting color change were monitored with UV-Visible spectrometer in Figure 3B (left).

After purifying CdSe core²³, we synthesize CdSe/(CdS)/ZnS core shell applying successive ion layer absorption reaction (SILAR) method²⁴. Cd injection solution is prepared by heating Cd, Oleic acid and ODE to around 230°C. Zn injection solution is heated around 120°C until it become clear after Zn undecylenate is mixed with trioctylphosphine (TOP) and ODE in glove box. Sulfur is dissolved in ODE by heating around 180°C for sulfur injection solution. After the calculation of amount of injection solution for each layer, CdSe core in hexane is added to HDA and ODE mixture. The reaction flask is pumped to remove the hexane completely and temperature is elevated to 100°C to get rid of residual hexane and air. When reaction temperature reaches to 240°C, each injection solution is added for each layer of shell. After checking the growth every 3-5mins by UV-Vis spectrum until the red shift of spectra stops, next injection solution is added. Each shell deposition was monitored with UV-Visible spectra in Figure 3B (right), and their final size distribution was verified to be monodispersed as well as to be about 7

nm range with TEM image in Figure 3A. distributionFinally green (CdSe/ZnS : 555nm) and red (CdSe/CdS/ZnS : 605nm) colored QDs are prepared.

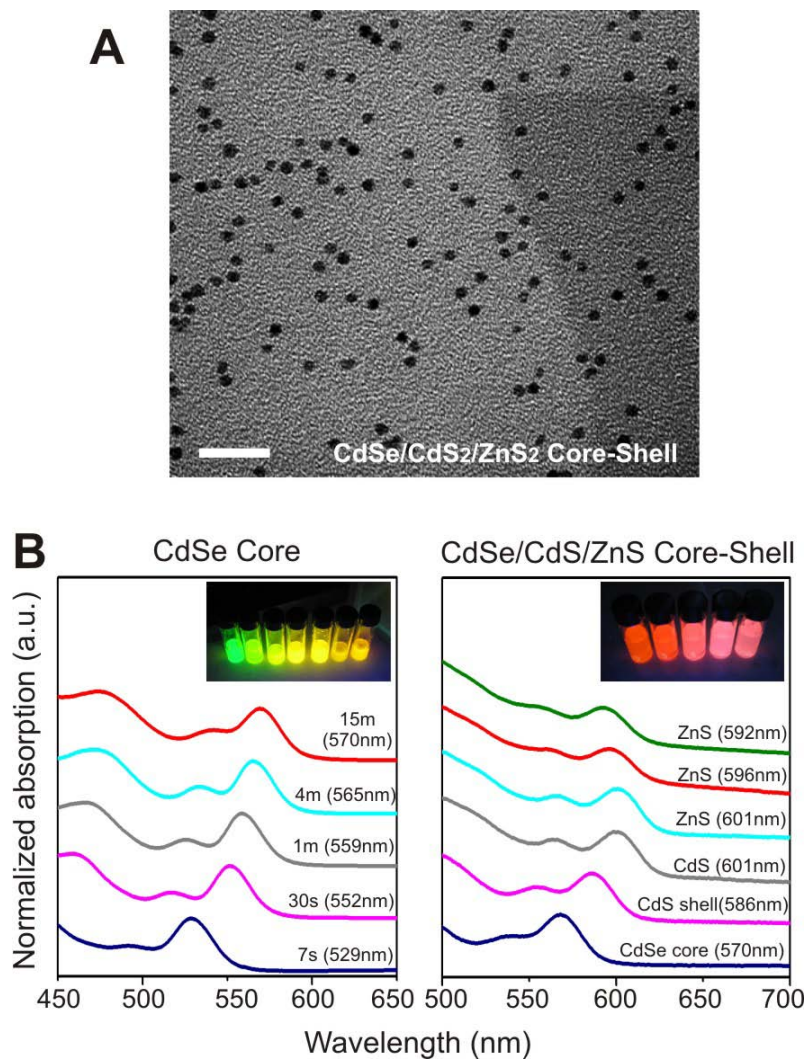


Figure III-3. (A): TEM image of CdSe/CdS/ZnS core-shell QDs (scale bar = 50nm) (B): Normalized UV-Vis absorption spectra of CdSe core (left) while these were growing and CdSe/CdS/ZnS core shell (right) after each shell was deposited.

1. 2. Synthesis of the Multidentate DHLA-Derivatized Polymer Lignds

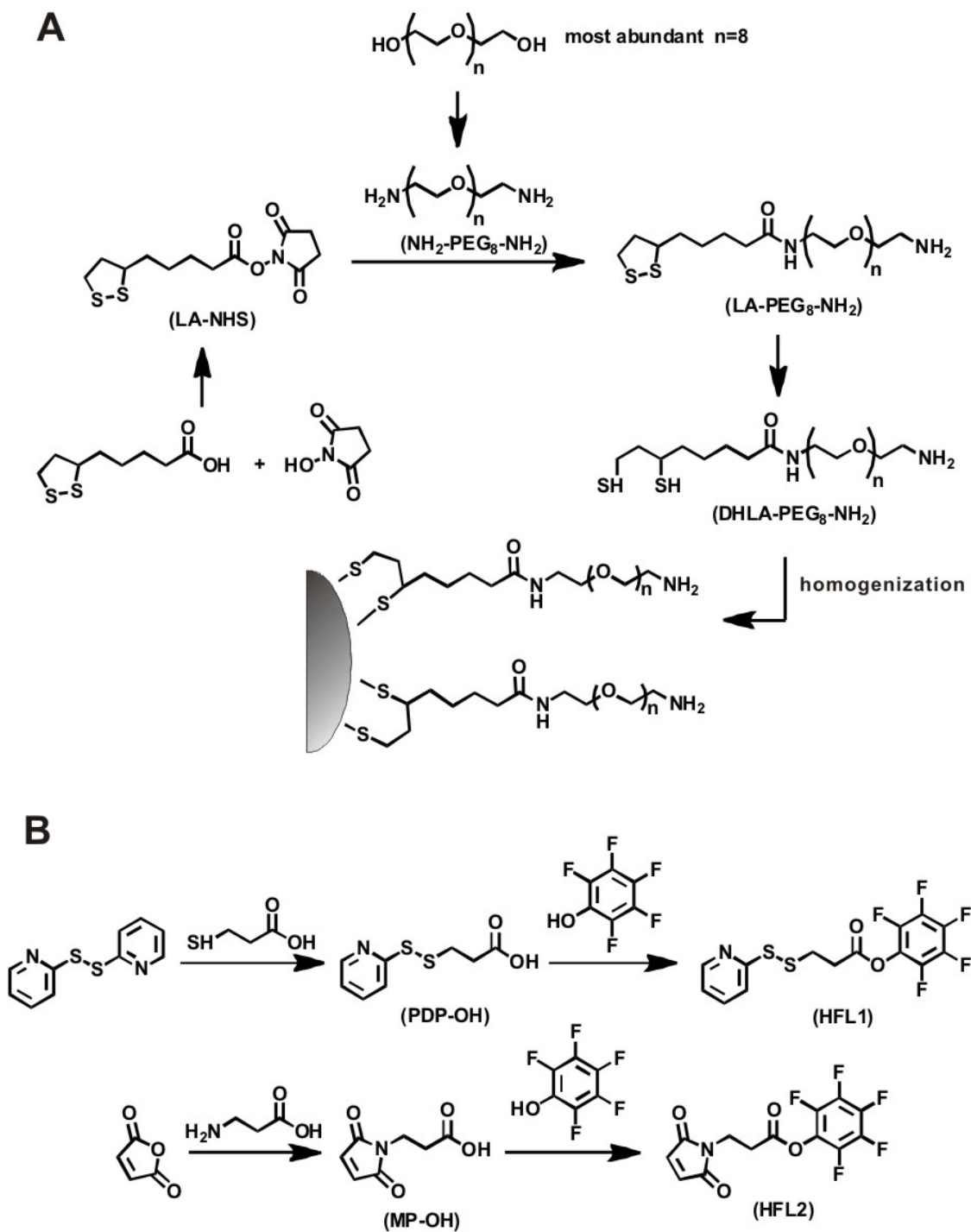
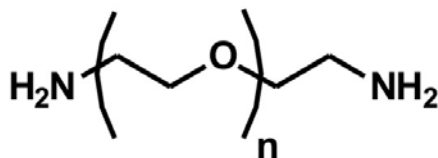


Figure III-4. Synthetic routes to DHLA-PEG-NH₂ (A) / heterofunctional linkers (B)

1. 2. 1. Diamino-PEG (NH₂-PEG₈-NH₂) (1)



Diamino-PEG (NH₂-PEG₈-NH₂) (1)

This procedure was modified from the literature.²⁶ Neat PEG₈ (20.0 g, 50.0 mmol, average MW 400 g/mol) was degassed at 100 °C for 4 h with stirring to remove all traces of water. The flask was cooled on an ice bath before thionyl chloride (10.5 mL, 145.0 mmol) was added dropwise. The solution was warmed to room temperature and stirred for 22 h, showing complete conversion to the bis-chloride by TLC (*R_f* 0.75, 90% DCM/MeOH, plate dried under vacuum prior to running) and ESI-MS (*m/z* 517.4 [M+H]⁺). The crude product was diluted with DMF (20 mL) and the solvent removed under reduced pressure. After repeating this three times, the flask was left under high vacuum overnight to remove all traces of thionyl chloride. The crude dark yellow product was dissolved in a solution of sodium azide (9.4 g, 145.0 mmol) in 250 mL of DMF. The resulting dark orange solution was stirred for 16 h at 85 °C, showing complete conversion to the diazide by TLC (*R_f* 0.6, 90% DCM/MeOH) and ESI-MS (*m/z* 531.4 [M+H]⁺). The solvent was removed under reduced pressure, and 200 mL of DCM was added. The precipitate was removed by vacuum filtration through Celite[®] and the solvent removed under high vacuum overnight to yield the intermediate diazide as a brown oil. The sample was dissolved in 300 mL of THF, and triphenylphosphine (27.8 g, 106.0 mmol) was

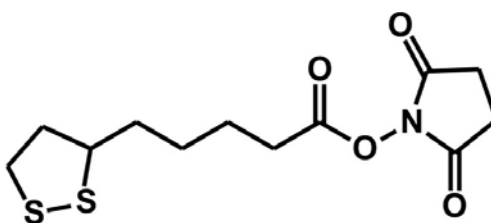
added. The dark orange solution was stirred at room temperature for 24 h, showing complete consumption of the diazide by ESI-MS and formation of the iminophosphorane intermediate by TLC (R_f 0.4, 90% DCM/MeOH). 4 mL of water was added and the dark brown mixture was stirred for 24 h, showing complete reduction to the bis-amine **1** by TLC (R_f 0.1, 90% DCM/MeOH) and ESI-MS (m/z 457.4 $[M+H]^+$). The THF was removed *in vacuo*, yielding a crude orange solid. 100 mL of water was added, and the precipitate was removed by vacuum filtration through a Büchner funnel. The filtrate was washed with toluene (3 x 50 mL). The water was removed *in vacuo* to give a dark orange oil. The crude product was purified by alumina column chromatography (DCM/MeOH, 95:5), giving **1** as a light-yellow oil (19.8 g, 99%). Spectroscopic data matched those previously reported.²⁶ Traces of triphenylphosphine oxide were detected by ^1H NMR.

1. 2. 2. Mitsunobu Reaction for Diamino-PEG ($\text{NH}_2\text{-PEG}_8\text{-NH}_2$) (**1**)

The previously reported protocols^{26,27} for the synthesis of **1** required multiple steps; therefore, we applied a Mitsunobu reaction⁴⁰ to access the bis-amine in a single step: PEG₈ (10.0 g, 25.0 mmol), previously dried over 3 Å molecular sieves, triphenylphosphine (13.1 g, 2.0 equiv), and phthalimide (7.4 g, 2.0 equiv) were dissolved in 150 mL of DCM and cooled to 0 °C under nitrogen. To this solution was added 95% diisopropylazodicarboxylate (DIAD, 10.4 mL, 2.0 equiv) dropwise with stirring, the temperature being kept at or below 20 °C. After the addition was complete, the reaction was allowed to warm to room temperature and was stirred for another hour. To the flask was then added 55% hydrazine (3.6 mL, 2.5 equiv) and the reaction was refluxed overnight under nitrogen. It was then cooled to room temperature and filtered. The filtrate

was stirred with 15 g of Amberlyst[®] 15 cation exchange resin for 5 h. The resin was then filtered and washed with DCM (3 x 50 mL). It was then added to a solution of 2.9 g of NaOH in 100 mL of anhydrous EtOH and mechanically stirred overnight. The resin was filtered and washed with 95% EtOH (3 x 50 mL). The filtrate and washings were concentrated *in vacuo* to give **1** as an amber oil (9.2 g, 93%). Spectroscopic data matched those previously reported.²⁶

1. 2. 3. Lipoic Acid *N*-Hydroxysuccinimide-Ester (LA-NHS) (**2**)

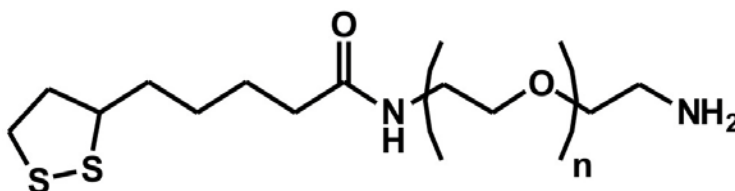


Lipoic Acid *N*-Hydroxysuccinimide-Ester (LA-NHS) (**2**)

This procedure was modified from the literature.²⁶ To a solution of DL-lipoic acid (5.00 g, 24.23 mmol) and *N*-hydroxysuccinimide (3.35 g, 29.1 mmol) in 150 mL of THF at 4 °C was added slowly a solution of dicyclohexylcarbodiimide (DCC, 6.00 g, 29.1 mmol) in 10 mL of THF. The mixture was warmed to room temperature and stirred for 8 h, showing complete conversion to the coupling product **2** by TLC (R_f 0.7, 90% DCM/MeOH). The precipitate was removed by vacuum filtration through Celite[®] and the solvent was evaporated *in vacuo*, leaving a yellow solid. The crude product was redissolved in ethyl acetate and filtered again. This filtrate was concentrated *in vacuo*, giving a pale-yellow oil. Recrystallization from a solution of hot ethyl acetate/hexane

(1:1 v/v) afforded pure dithiane **2** a pale-yellow solid (3.47 g, 47%). The mother liquor was concentrated down and saved for future recrystallizations. Spectroscopic data matched those previously reported.²⁶

1. 2. 4. Lipoic Acid-PEG-Amine (LA-PEG₈-NH₂) (**3**)

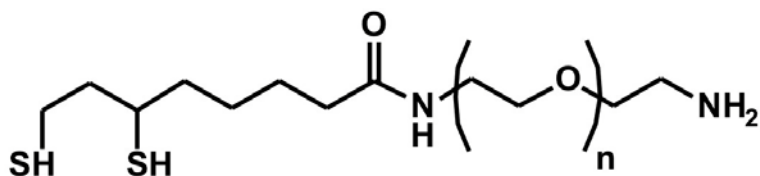


Lipoic Acid-PEG-Amine (LA-PEG₈-NH₂) (**3**)

This procedure was modified from the literature.²⁶ To a yellow solution of **1** (13.04 g, 32.8 mmol) and sodium bicarbonate (2.75 g, 32.8 mmol) in DMF/water (100 mL, 50:50 v/v) at 4 °C was added dropwise a solution of recrystallized **2** (1.80 g, 5.9 mmol) in 10 mL of DMF over 1 h, turning the reaction mixture a lighter yellow. The solution was warmed to room temperature and stirred for 16 h, showing complete conversion to the amide **3** by TLC (R_f 0.15, 90% DCM/MeOH) and ESI-MS (m/z 601.3 $[M+H]^+$). The crude product mixture was extracted with chloroform (3 x 30 mL). The combined organic extracts were washed with water (3 x 30 mL), dried over sodium sulfate, and filtered, and the solvent was evaporated under reduced pressure. The crude product was purified by alumina column (DCM/MeOH, 95:5), yielding **3** as a yellow oil (1.93 g, 58%). The remainder of the product was contaminated with traces of **1**. This material was recycled along with excess **1** that was recovered from the aqueous layer. Spectroscopic data matched those previously reported.²⁶

The published procedure²⁶ for the synthesis of **3** required excessive extractions from the DMF/water layer; therefore, we developed the following protocol: **1** (7.8 g, 5.0 equiv) was dissolved in 50 mL of DCM. To this solution was added a solution of **2** in 50 mL of DCM, dropwise with stirring, over 1 h. After another 30 min, the solvent was removed *in vacuo* and the residue chromatographed on silica gel eluting (1% NH₄OH/10% MeOH/DCM). **3** were obtained as an amber oil weighing (2.6 g, 96%). Spectroscopic data matched those previously reported.²⁶

1. 2. 5. Dihydrolipoic Acid-PEG-Amine (DHLA-PEG₈-NH₂) (**4**)



Dihydrolipoic Acid-PEG-Amine (DHLA-PEG₈-NH₂) (**4**)

This procedure was modified from the literature.²⁶ To a yellow solution of **3** (0.200 g, 0.333 mmol) in 4:1 water/ethanol (3 mL) at 4 °C was slowly added 4 equiv of sodium borohydride (0.050 g, 1.331 mmol) over a 30 min period. The bubbling solution was stirred for 4 h at 4 °C, showing only 67% conversion to the reduction product **4** by ESI-MS (m/z 603.3 [M+H]⁺). The product and starting material had overlapping TLC spots (R_f 0.15, 90% DCM/MeOH). The reaction mixture was left stirring overnight at room temperature. No further conversion was observed, so a total of 8 more equiv of sodium borohydride were added over a 48 h period, driving the reaction to completion in 72 h. The crude reaction mixture was acidified to pH 2 with 1 M HCl, and extracted with

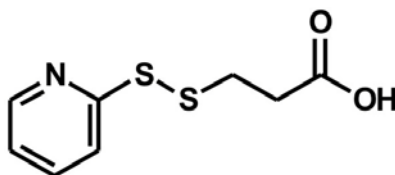
chloroform (3 x 15 mL). The combined organics were dried over magnesium sulfate and filtered. The solvent was removed *in vacuo* to furnish the dithiol **4** as a yellow oil (0.196 g, 98%). Spectroscopic data matched those previously reported.²⁶ Traces of triphenylphosphine oxide were detected by ¹H NMR. A stability study was conducted on the dithiol. A 6 mg sample in CDCl₃ was kept under argon in a capped NMR tube for 48 h, and no change was observed in the ¹H NMR spectrum. The sample was then exposed to the atmosphere in an uncapped NMR tube for 48 h, again showing no change by ¹H NMR. This product appeared to be air-stable.

1. 2. 6. Surface Modification of Quantum Dots with DHLA-PEG₈

Hydrophobic ligands (TOPO/HDA) on the surface of the as-synthesized QDs were exchanged with **4** according to known protocols.²⁷

1. 3. Synthesis of the Heterofunctional Linkers

1. 3. 1. 3-(2-Pyridyl)-dithiopropionic acid (PDP-OH) (**5**)

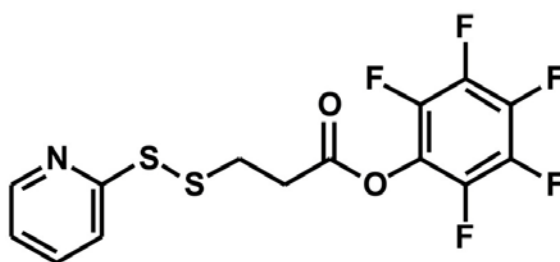


3-(2-Pyridyl)-dithiopropionic acid (PDP-OH) (**5**)

This procedure was modified from the literature.²⁹ Pyridyl disulfide (3.11 g, 14.11 mmol) was dissolved in 30 mL of anhydrous EtOH and cooled to -10 °C. Mercaptopropionic acid (MPA, 1.0 g, 9.42 mmol) in 20 mL of anhydrous EtOH was

added dropwise over 30 min at -10 °C. The reaction mixture was allowed to warm to room temperature. After 24 h, the solvent was removed *in vacuo* and the residue was chromatographed (5-15% EtOAc/hexane). **7** was isolated as a pale yellow solid (1.3 g, 64%). Spectroscopic data matched those previously reported.²⁹

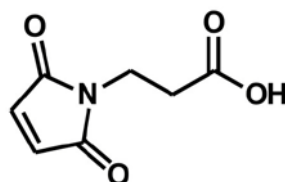
1. 3. 2. 3-(2-Pyridyl)-dithiopropionic acid pentafluorophenyl ester (HFL1) (**6**)



3-(2-Pyridyl)-dithiopropionic acid pentafluorophenyl ester (HFL1) (**6**)

This procedure was modified from the literature.²⁸ **7** (1.3 g, 6.04 mmol), pentafluorophenol (PFP, 1.1 g, 1 equiv), and DCC (1.25 g, 1 equiv) were dissolved in 30 mL of DCM and the reaction mixture was stirred at room temperature under nitrogen. After 48 hours, another 100 mg of both PFP and DCC were added to drive the coupling to completion within 3 hours. The solvent was removed *in vacuo*, and the residue was purified by silica gel column chromatography (5% EtOAc/hexane). **8** was obtained as a yellow oil (1.88 g, 82%). Spectroscopic data matched those previously reported.⁸ Traces of DCC were detected by ¹H NMR.

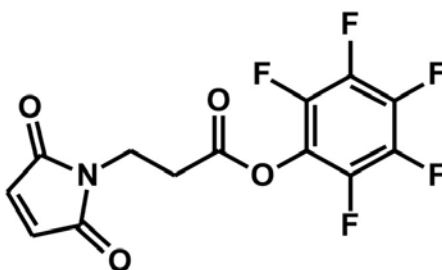
1. 3. 3. 3-Maleimidopropionic acid (MP-OH) (7)



3-Maleimidopropionic acid (MP-OH) (7)

MP-OH was synthesized according to the literature.⁴¹ **5** was obtained as a white solid (43%). A significant amount of crude product could not be loaded onto the silica column due to its low solubility in chloroform even at elevated temperatures. This crude material was saved for future purifications. Spectroscopic data matched those previously reported.⁴¹

1. 3. 4. 3-Maleimidopropionic acid pentafluorophenyl ester (HFL2) (8)



3-Maleimidopropionic acid pentafluorophenyl ester (HFL2) (8)

HFL2 was synthesized according to the literature.²⁸ **6** was obtained as a white solid (74%). ¹H-NMR (CDCl₃) δ: 6.72 (2H, s, maleimide), 3.95 (2H, t, -CH₂^α-), 3.04 (2H, t, -CH₂^β-). Nielsen and Buchardt⁴² inadvertently reported the maleimide proton signal as the solvent peak (δ: 7.26, s, CDCl₃). Our spectrum agreed well with that of the reported hexanoic analogue.²⁸

2. Target-specific delivery of siRNA-QDs and their transfection efficiency

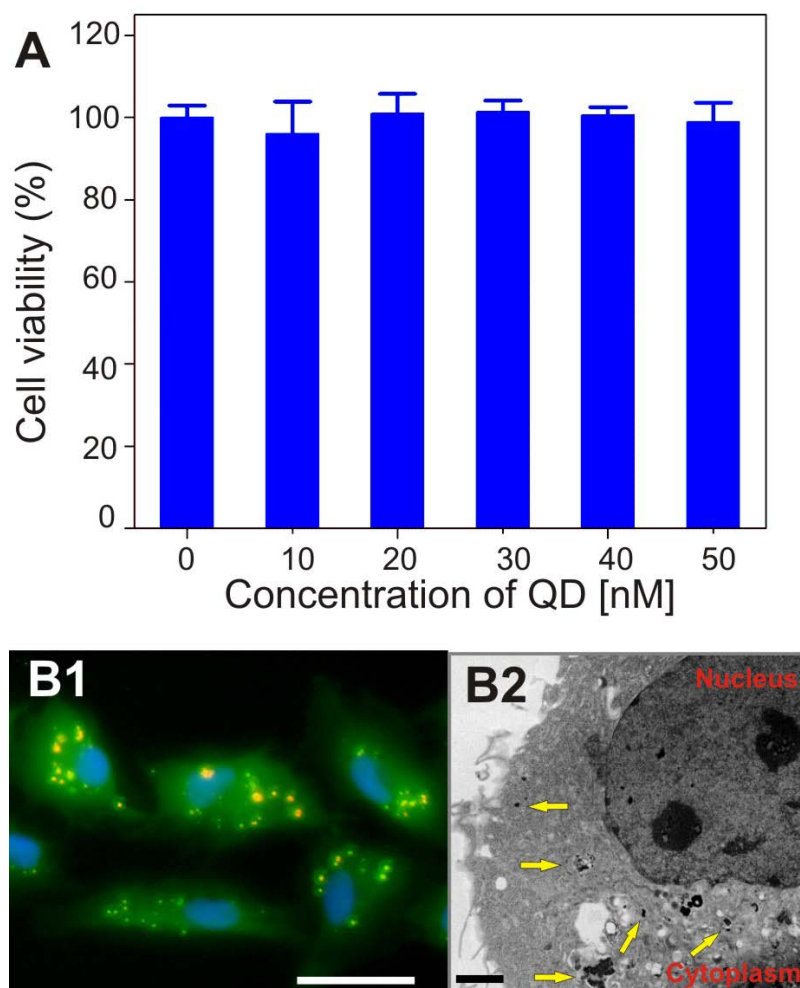


Figure III-5. (A): Toxicity of QDs using MTS assay. Most of U87 cells were found to be viable across the concentration range of QDs. The QDs tested within the above range were found to be non-cytotoxic and all knockdown experiments were conducted within the 50 nM range. **(B1): Tracking siRNA delivery using siRNA covalently linked to QDs.** The siRNA-QDs can be clearly seen within the cytoplasm of the U87-EGFP cells. The QDs used for tracking the delivery of siRNA emitted at 594 nm and were yellow-orange in color, as opposed to the QDs used for delivering the siRNA which emitted at 614 nm and were red in color. (Scale bar = 100 μ m) **(B2): TEM image of internalization of multifunctional siRNA-QDs.** Multifunctional siRNA-QDs transfected in the cytoplasm are verified with TEM image (scale bar = 2.5 μ m)

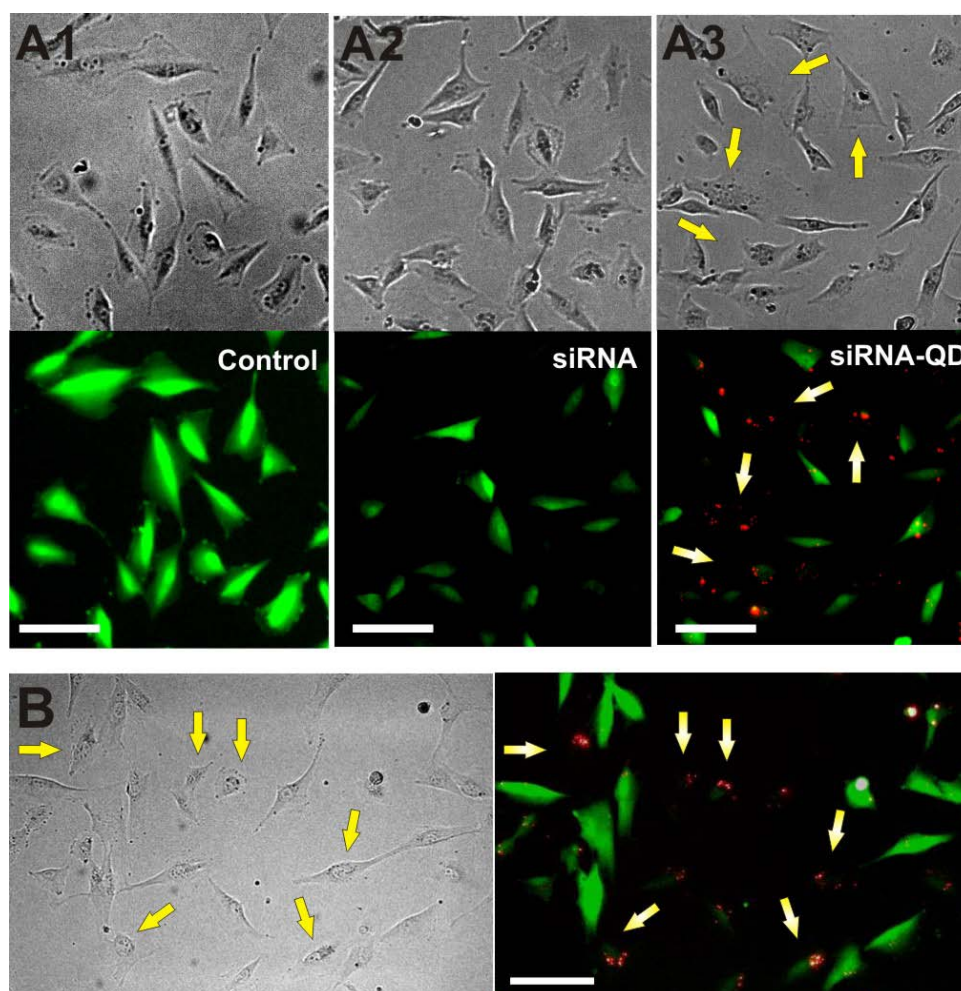


Figure III-6. Knockdown of EGFP in U87 cells using siRNA-QDs (A1): Control U87-EGFP cells without siRNA-QDs; (A2): U87-EGFP cells transfected with only siRNA and knockdown of EGFP; (A3): EGFP knockdown using multi-functional siRNA-QDs (phase contrast images vs corresponding fluorescence images); Phase contrast image showing that the morphology of U87-EGFP cells has not changed as compared to the control cells in (A1). Fluorescence image clearly shows the knockdown of EGFP in cells (marked by yellow arrows) which have internalized the siRNA-QDs (red) after 48 hrs. (B): Co-cultures of U87-EGFP control cells (without siRNA-QDs) and U87-EGFP cells transfected with siRNA-QDs so as to investigate them under the same conditions; Phase contrast image clearly shows no difference in the morphology of the U87-EGFP control cells and the siRNA-QDs transfected cells. Fluorescence image clearly shows the decrease in the EGFP signal in the U87-EGFP cells transfected with siRNA-QD as compared to the surrounding U87-EGFP control cells. (Scale bar: 100 μ m) Copyright Wiley-VCH Verlag GmbH & Co. KGaA. Reproduced with the permission of Ref. 49

To optimize gene silencing with our siRNA-QD constructs and to assess the transfection efficiency and RNA interference (RNAi) activity, we examined the suppression of EGFP expressed in U87 cell lines that were genetically modified to express EGFP. Cytotoxicity of the constructs was tested by serial dilution studies. The range of concentration causing minimal/negligible cytotoxicity was identified in Figure 5A and the subsequent experiments employed the concentrations within this range.^{43,44} Importantly, the EGFP cell line has been widely used to investigate siRNA-based silencing of EGFP, since the suppression of EGFP expression does not compromise cell viability. The transfection efficiency of three different kinds of constructs were evaluated; constructs modified with the RGD peptide only, those modified with the HIV Tat peptide only, and those with both HIV-Tat and RGD peptide. Although the siRNA-QDs modified with only RGD showed considerable selective internalization within U87-EGFP cells, siRNA-QDs modified with a combination of RGD and HIV-tat peptides (the ratio of siRNA: RGD: HIV-Tat being 1:10:10 per QD) showed maximum internalization within U87-EGFP cells, in close agreement with previous studies.⁸ This optimal condition was used for subsequent siRNA-QD experiments.

The U87-EGFP cell line was then treated with siRNA-QDs (siRNA:QDs = 0.12 μ M:0.11 μ M), modified with HIV-Tat [\sim 1.2 μ M] and RGD [\sim 1.2 μ M], and simultaneously imaged using fluorescence microscopy in Figure 6. Cationic lipids (X-tremeGENE, Roche) were used to further enhance cellular uptake and prevent degradation of the siRNA within the endosomal compartment of the cells. The siRNA-QDs showed significant internalization into the cells. Knockdown of the EGFP signal was observed after 48-72 hrs (Figure 6A3). Fluorescence intensity was influenced by

other factors such as exposure time, media condition, and cell shrinkage. To minimize the influence from these external factors, the control U87-EGFP cells (without siRNA) were trypsinized and co-cultured with U87-EGFP cells transfected with siRNA-QDs in the same well. The U87 cells containing siRNA-QDs were easily distinguishable from the control cells due to the bright fluorescent property of the QDs (Figure 6C). Cells with internalized siRNA-QDs showed considerable knockdown of the EGFP protein when compared with the surrounding control U87-EGFP cells in Figure 6C.

To further demonstrate the target-specific delivery of the siRNA-QDs, we incubated the siRNA-QDs modified with Tat and RGD against EGFP in co-cultures of the U87-EGFP cell line with other less-tumorigenic cell lines, such as PC-12 and SK-N-BE(2)C in Figure 7, having a considerably small number of integrin receptors.⁴⁵⁻⁴⁷ The presence of RGD tripeptide molecules on the surface of the siRNA-QDs led to specific binding with integrin receptors overexpressed in the U87 cells, resulting in higher cellular uptake by the malignant U87 cells as compared to the less tumorigenic PC-12 cells/SK-N-BE(2)C as seen by the selective accumulation of the QDs within the U87-EGFP cells in Figure 7. These results confirmed our hypothesis that the target-specific delivery of the siRNA-QDs into brain cancer cells can be significantly enhanced by functionalizing the QDs with targeting moieties like RGD tripeptide.

The intracellular delivery of the siRNA-QDs within the U87-EGFP cells was also confirmed by transmission electron microscopy (TEM), which clearly shows the presence of QDs in the cytoplasm of the cells in Figure 8A. The knockdown efficiency of the siRNA-QDs was similar to or slightly better than that of the positive control consisting of U87-EGFP cells transfected with only siRNA using X-tremeGENE in Figure 6A. This

high transfection efficiency appears to be due to synergistic effects of the two transfection peptides. Decrease in fluorescence intensities (EGFP signal, green fluorescence) within cells treated with the above mentioned systems were then compared with the intensity of U87-EGFP without siRNA. As shown in Figure 8B, the decrease in fluorescence intensity of U87-EGFP incubated with siRNA-QDs and siRNA alone was comparable, but drastically lower than that observed for the control without siRNA. Cells with internalized siRNA-QDs show decreased green fluorescence (EGFP signal) when compared with the control. This data strongly suggests that siRNA-QDs can be simultaneously used as delivery and imaging probes.

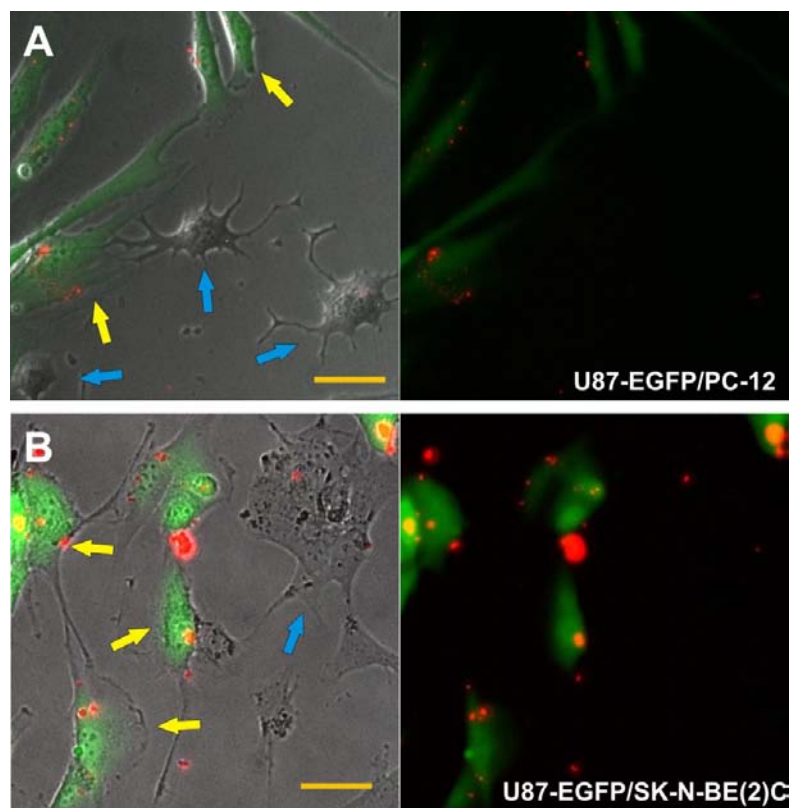


Figure III-7. Knockdown of EGFP in U87 cells using siRNA-QD modified with RGD and HIV-Tat peptides (note that yellow arrows represent U87- EGFP cells transfected with the siRNA-QDs and the blue arrows indicate PC-12 cells or SK-N-BE(2)C cells) **(A):** Phase contrast and fluorescence image showing the target-oriented delivery of siRNA-QDs in co-cultures of the malignant U87-EGFP cells, overexpressing the $\alpha_v\beta_3$ integrin receptors, and the less tumorigenic PC-12 cells (blue arrows) incubated with the siRNA-QDs. It can be clearly seen that most of the siRNA-QDs, due to the presence of RGD and HIV-tat peptides, were taken up by the U87-EGFP cells and not by the PC-12 cells. (Scale bar: 50 μ m) **(B):** Phase contrast and fluorescence image showing the target-oriented delivery of siRNA-QDs in co-cultures of the malignant U87-EGFP cells and the less tumorigenic SK-N-BE(2)C cells (blue arrows) incubated with the siRNA-QDs. Most of the siRNA-QDs, due to the presence of RGD and HIV-tat peptides, were taken up by the U87-EGFP cells instead of SK-N-BE(2)C cells (Scale bar: 50 μ m)

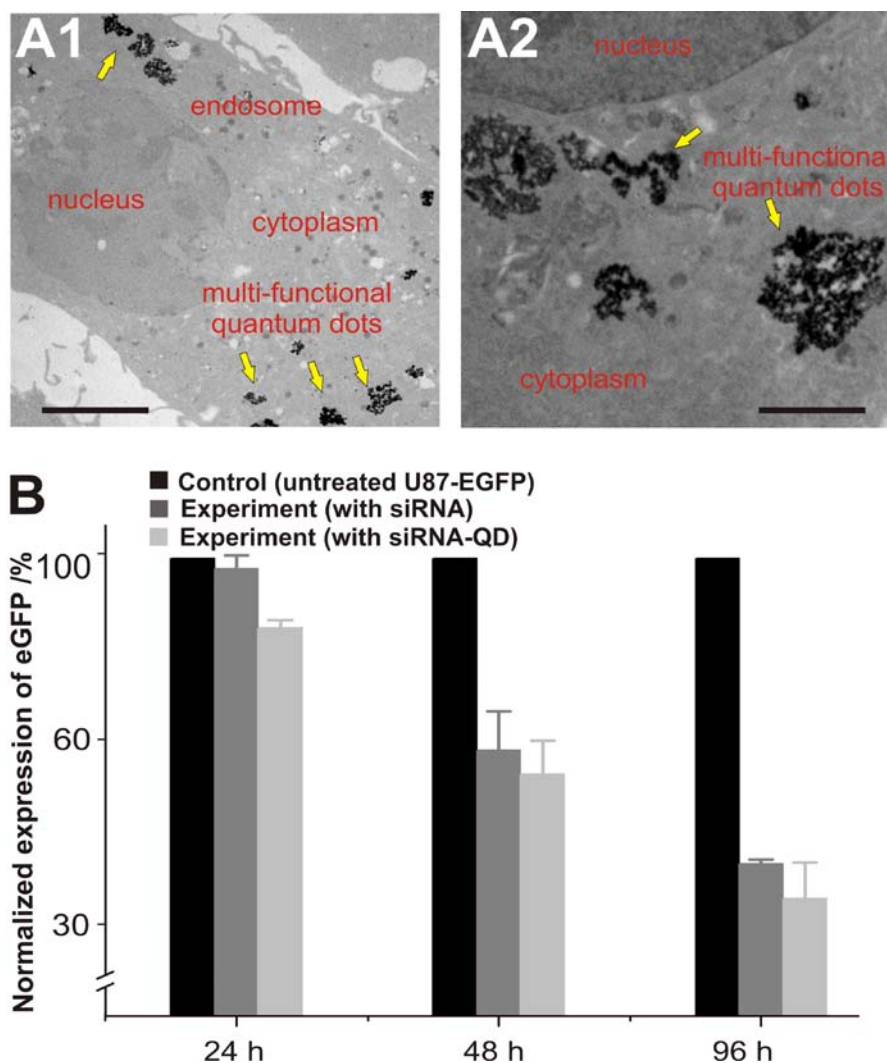


Figure III-8. Knockdown efficiency of EGFP within U87-EGFP cells and internalization of multifunctional siRNA-QDs . (A): TEM analysis of the internalization of the multifunctional siRNA-QDs into the U87-EGFP cells; (A1) Presence of multi-functional siRNA-QDs (yellow arrows) within the cytoplasm and the endosome (Scale bar: 5 μ m). (A2) Zoomed-in image showing individual siRNA-QDs within the cytoplasm (Scale bar: 2.5 μ m). (B): The bar graph represents the knockdown of EGFP over 24h, 48h, and 96h in U87-EGFP cells treated with siRNA only (dark grey), and siRNA-QD (light grey). The EGFP knockdown data was normalized with the expression levels of EGFP in the control U87-EGFP cells (black). Copyright Wiley-VCH Verlag GmbH & Co. KGaA. Reproduced with the permission of Ref. 49

3. Knockdown of EGFRvIII as a chemotherapeutic target by siRNA-QDs

Having demonstrated the selective manipulation of the U87-EGFP cell line, we then focused on the knockdown of EGFRvIII with our siRNA-QD constructs. U87-EGFRvIII cells were genetically modified to overexpress EGFRvIII, a mutant-type epidermal growth factor receptor (EGFR) only expressed within cancer cells.⁴⁸ This cell type was incubated with our siRNA-QDs modified with Tat and RGD peptides and armed with EGFRvIII-targeting siRNA. The cells were simultaneously imaged for the internalization of siRNA-QDs using fluorescence microscopy. Significant cell death was observed in the wells loaded with siRNA-QDs against EGFRvIII after 48h in Figure 9. Quantitative analysis revealed that the number of viable U87-EGFRvIII cells, as observed via fluorescence microscopy, decreased with increased incubation time. When compared with the control (U87-EGFRvIII without siRNA-QDs), there was a significant decrease in the number of viable cells, thus demonstrating the effectiveness of our nanoparticle-based siRNA delivery to knock-down the oncogene. The result was confirmed using the MTT assay which showed a decrease in the number of viable cells in the well incubated with siRNA-QDs against EGFRvIII in Figure 10A. This assay further confirmed that the QDs themselves were noncytotoxic when used alone as they did not result in any appreciable cell death as shown in Figure 5A. The knockdown of EGFRvIII and the inhibition of the downstream proteins in the PI3K signaling pathway were confirmed using Western Immunoblotting. The results in Figure 10B confirm a considerable decrease in the expression of EGFRvIII, and down-regulation of phospho-AKT and phospho-S6 as compared to the control. Thus, these results demonstrate the specificity of

the siRNA against EGFRvIII, the inherent noncytotoxicity of the QDs, and the facile evaluation and manipulation of cancer cell proliferation with multifunctional-QD constructs.

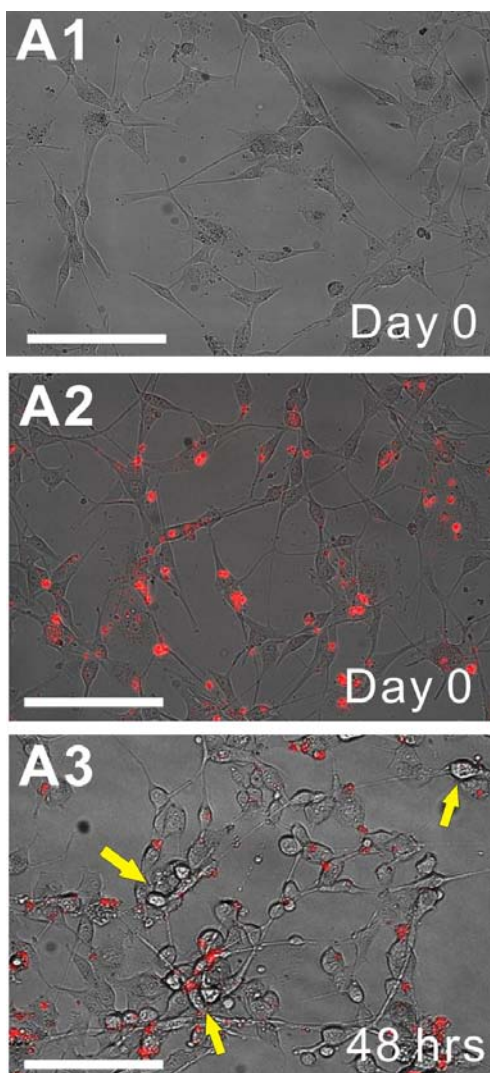


Figure III-9. Phase contrast images showing the internalization of siRNA-QDs against EGFRvIII into the U87-EGFRvIII cells. (A1): Morphology of U87-EGFRvIII cells before incubation with siRNA-QDs on Day 0. **(A2):** U87-EGFRvIII cells after incubation with siRNA-QDs (red) on Day 0. **(A3):** Morphology of U87-EGFRvIII 48hrs after incubation with siRNA-QDs. Note that effect of the EGFRvIII knockdown by the siRNA-QDs can be clearly seen as they have clearly shrunk (yellow arrows) and look collapsed as compared to Day 0, marking the onset of apoptosis (Scale bar = 100 μ m). Copyright Wiley-VCH Verlag GmbH & Co. KGaA. Reproduced with the permission of Ref. 49

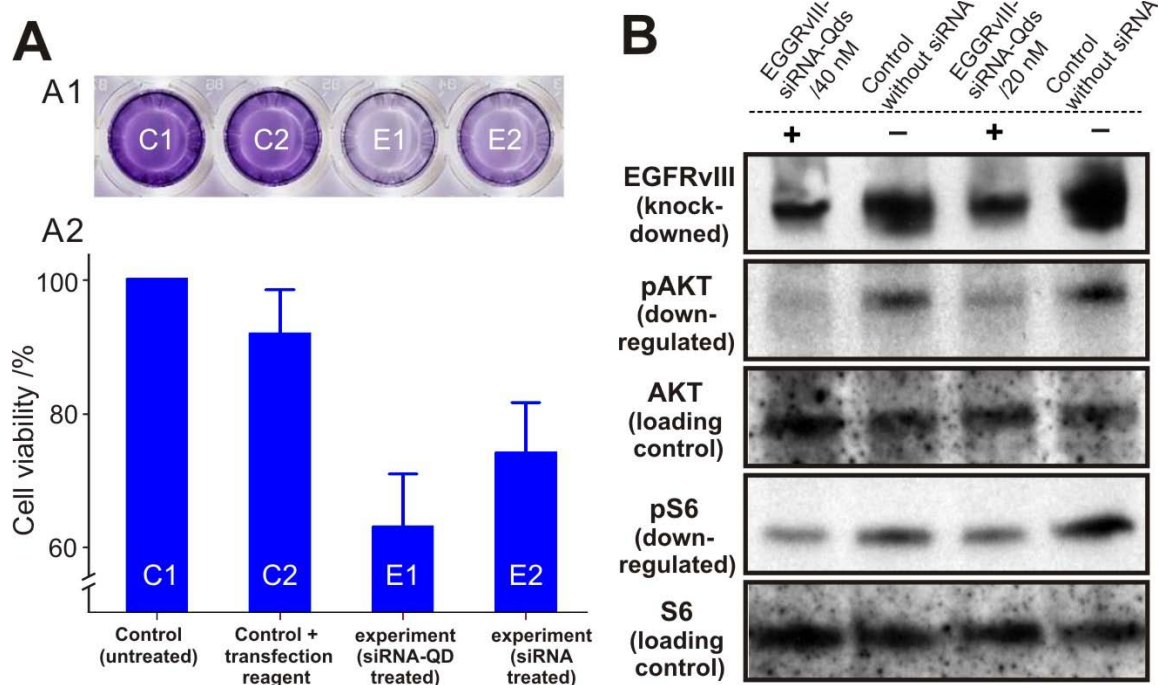


Figure III-10. Knockdown of EGFRvIII in U87 EGFRvIII using multifunctional siRNA-QDs (A): Cell viability assay using MTT assay. **(A1)** Optical image of cell viability (MTT) assay in a well plate. Dark blue color represents high number of viable cells and pale blue indicates low viable cell population. **(A2)** MTT assayed wells were quantified with UV absorbance and converted to cell viability. Untreated control C1 and C2 represent control cell population and viable cell population in presence of a cationic lipid based transfection reagent respectively. siRNA-QD transfected cells in experiment (E1) and siRNA treated cells in E2 show low numbers of the viable cells due to knockdown of EGFRvIII gene **(B)** Western Immunoblotting to show silencing effect of EGFRvIII gene. Protein expression level of EGFRvIII is dramatically decreased, and phosphorylation levels of key proteins in PI3K signaling pathway are reduced significantly. The upstream protein (AKT) and the downstream protein (S6), which plays an important role in cell proliferation, are selected to investigate the gene-knockdown effect on the PI3K signaling pathway. Copyright Wiley-VCH Verlag GmbH & Co. KGaA. Reproduced with the permission of Ref. 49

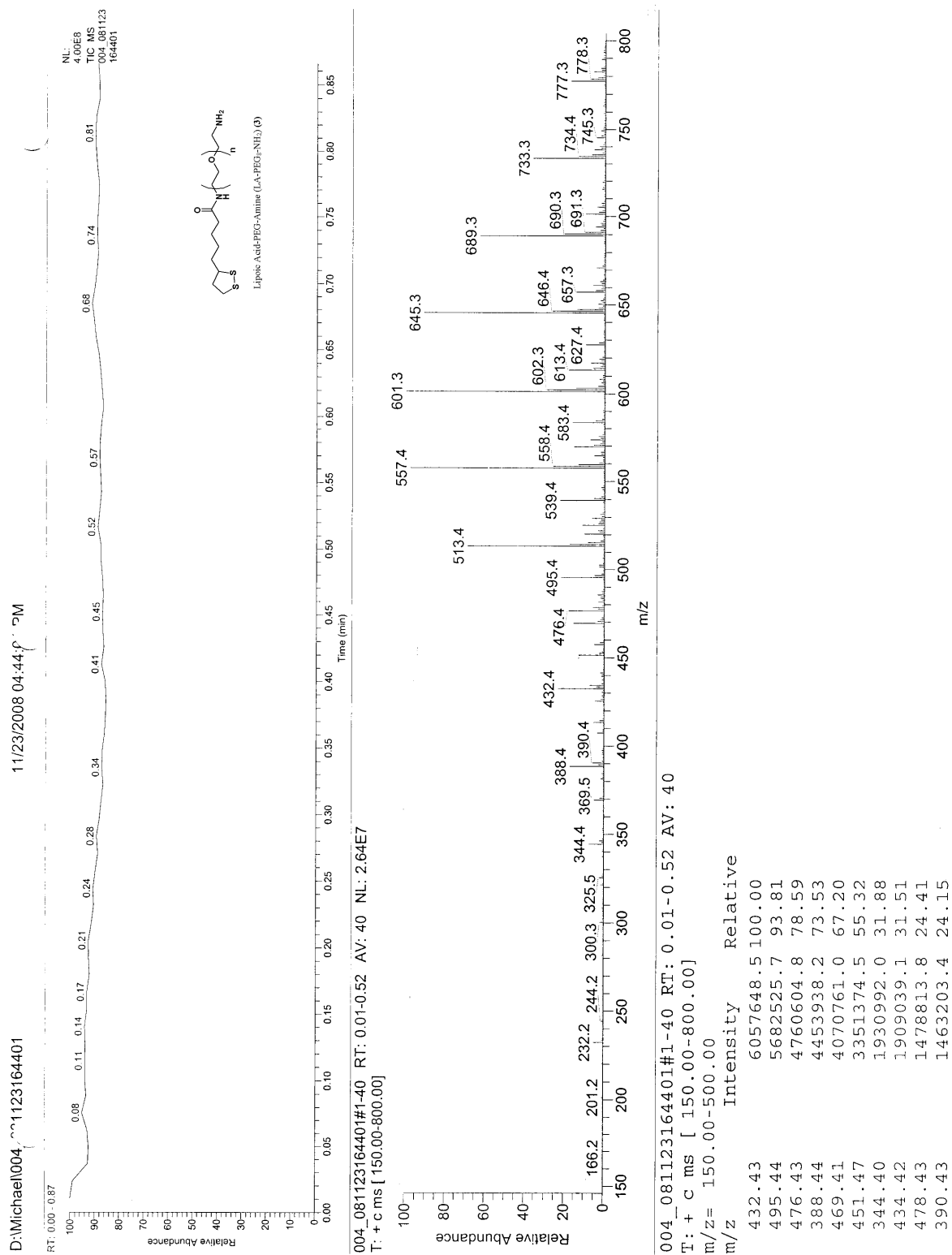
D. Conclusion

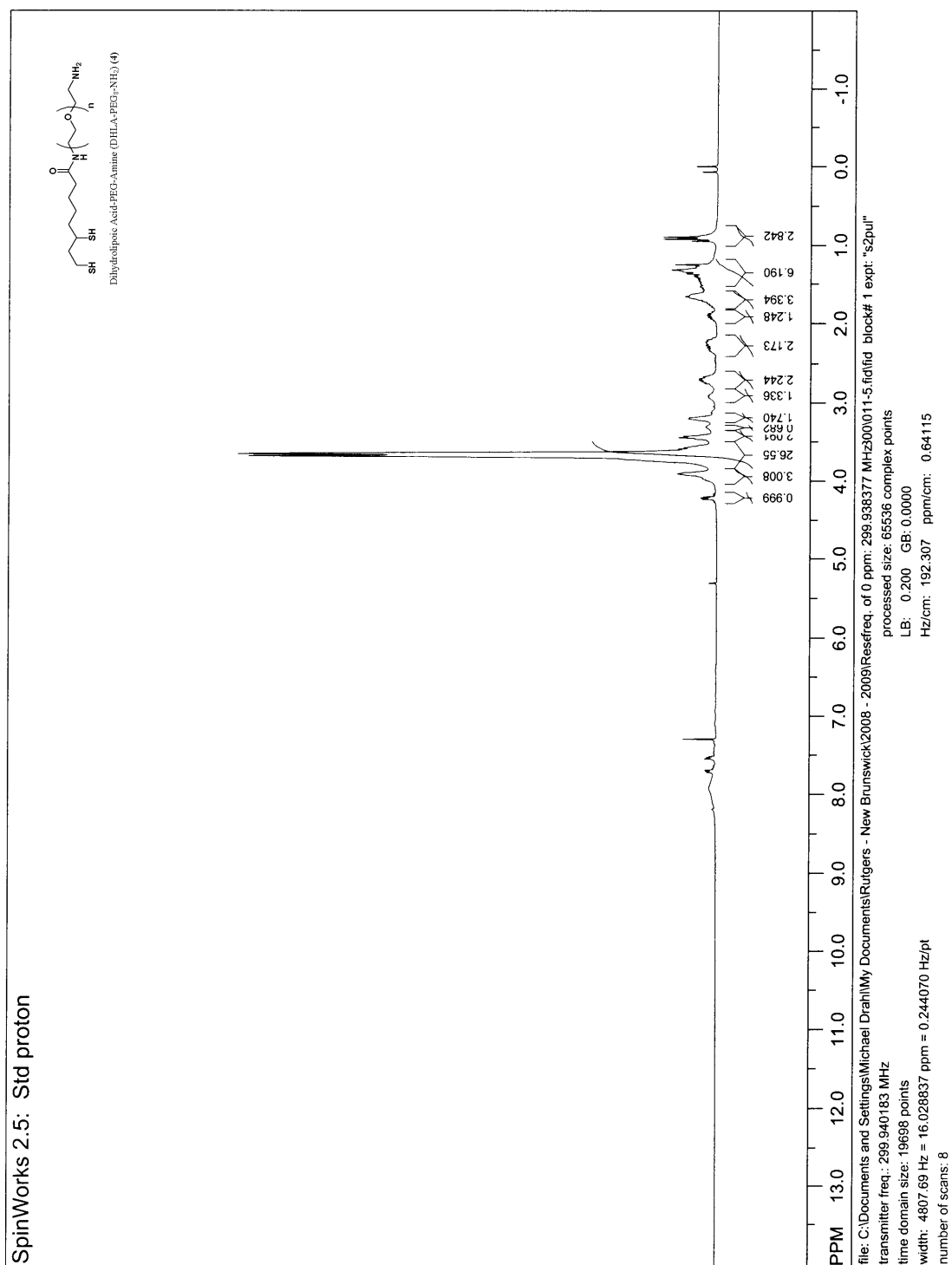
In summary, this work is a demonstration of the multi-functional siRNA-QD strategy focusing on targeted delivery, high transfection efficiency, and multi-modal imaging/tracking. Our siRNA-QDs could be used for the development of novel chemotherapies and diagnostics relevant to brain cancer research. These novel methods and applications complement recent advances in nanomaterial-based siRNA delivery, nanomaterial-based molecular imaging, as well as siRNA-based chemotherapeutic strategies reported recently. While the ability to functionalize as well as control the surface of quantum dots with specific linkers and multi-functional molecules (siRNA and peptides) is critical for nanoparticle-based drug delivery, this method could also provide highly useful information regarding bio-surface chemistry of nanomaterials. In addition, the application of multi-functional siRNA-QDs to modulate the key cancer signaling pathways is important not only for selective chemotherapeutic strategy but also for dissecting signaling cascades triggered by inhibiting specific proteins. Collectively, our multi-functional QD-based siRNA delivery strategy has significant potential for simultaneous prognosis, diagnosis, and therapy.

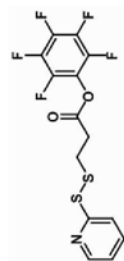
E. Appendix

- 1. Mass spectra of Lipoic Acid-PEG-Amine (LA-PEG₈-NH₂) (3)**
- 2. Mass spectra of Dihydrolipoic Acid-PEG-Amine (DHLA-PEG₈-NH₂) (4)**
- 3. NMR spectra of Dihydrolipoic Acid-PEG-Amine (DHLA-PEG₈-NH₂) (4)**
- 4. NMR spectra of 3-(2-Pyridyl)-dithiopropionic acid pentafluorophenyl ester (HFL1) (6)**

1. Mass spectra of Lipoic Acid-PEG-Amine (LA-PEG₈-NH₂) (3)



3. NMR spectra of Dihydrolipoic Acid-PEG-Amine (DHLA-PEG₈-NH₂) (4)



F. References

- 1 Medarova, Z., Pham, W., Farrar, C., Petkova, V. & Moore, A. In vivo imaging of siRNA delivery and silencing in tumors. *Nature Medicine* **13**, 372-377, doi:10.1038/nm1486 (2007).
- 2 Dykxhoorn, D. M., Palliser, D. & Lieberman, J. The silent treatment: siRNAs as small molecule drugs. *Gene Therapy* **13**, 541-552, doi:10.1038/sj.gt.3302703 (2006).
- 3 Wasungu, L. & Hoekstra, D. Cationic lipids, lipoplexes and intracellular delivery of genes. *Journal of Controlled Release* **116**, 255-264, doi:10.1016/j.jconrel.2006.06.024 (2006).
- 4 Jeong, J. H., Mok, H., Oh, Y. K. & Park, T. G. siRNA Conjugate Delivery Systems. *Bioconjugate Chemistry* **20**, 5-14, doi:10.1021/bc800278e (2009).
- 5 Patil, M. L. *et al.* Surface-modified and internally cationic polyamidoamine dendrimers for efficient siRNA delivery. *Bioconjugate Chemistry* **19**, 1396-1403, doi:10.1021/bc8000722 (2008).
- 6 Zintchenko, A., Philipp, A., Dehshahri, A. & Wagner, E. Simple modifications of branched PEI lead to highly efficient siRNA carriers with low toxicity. *Bioconjugate Chemistry* **19**, 1448-1455, doi:10.1021/bc800065f (2008).
- 7 Lee, J. H. *et al.* All-in-One Target-Cell-Specific Magnetic Nanoparticles for Simultaneous Molecular Imaging and siRNA Delivery. *Angewandte Chemie-International Edition* **48**, 4174-4179, doi:10.1002/anie.200805998 (2009).
- 8 Derfus, A. M., Chen, A. A., Min, D. H., Ruoslahti, E. & Bhatia, S. N. Targeted quantum dot conjugates for siRNA delivery. *Bioconjugate Chemistry* **18**, 1391-1396 (2007).
- 9 Qi, L. F. & Gao, X. H. Quantum dot-amphipol nanocomplex for intracellular delivery and real-time imaging of siRNA. *Acs Nano* **2**, 1403-1410, doi:10.1021/nn800280r (2008).
- 10 Lee, J. S. *et al.* Gold, Poly(beta-amino ester) Nanoparticles for Small Interfering RNA Delivery. *Nano Letters* **9**, 2402-2406, doi:10.1021/nl9009793 (2009).
- 11 Yezhelyev, M. V., Qi, L. F., O'Regan, R. M., Nie, S. & Gao, X. H. Proton-sponge coated quantum dots for siRNA delivery and intracellular imaging. *Journal of the American Chemical Society* **130**, 9006-9012, doi:10.1021/ja800086u (2008).

- 12 Giljohann, D. A., Seferos, D. S., Prigodich, A. E., Patel, P. C. & Mirkin, C. A. Gene Regulation with Polyvalent siRNA-Nanoparticle Conjugates. *Journal of the American Chemical Society* **131**, 2072-+, doi:10.1021/ja808719p (2009).
- 13 Kikkeri, R., Lepenies, B., Adibekian, A., Laurino, P. & Seeberger, P. H. In Vitro Imaging and in Vivo Liver Targeting with Carbohydrate Capped Quantum Dots. *Journal of the American Chemical Society* **131**, 2110-+, doi:10.1021/ja807711w (2009).
- 14 Bhirde, A. A. *et al.* Targeted Killing of Cancer Cells in Vivo and in Vitro with EGF-Directed Carbon Nanotube-Based Drug Delivery. *Acs Nano* **3**, 307-316, doi:10.1021/nn800551s (2009).
- 15 Fan, Q. W. & Weiss, W. A. RNA interference against a glioma-derived allele of EGFR induces blockade at G(2)M. *Oncogene* **24**, 829-837, doi:10.1038/sj.onc.1208227 (2005).
- 16 Arwert, E. *et al.* Visualizing the dynamics of EGFR activity and antiglioma therapies in vivo. *Cancer Research* **67**, 7335-7342, doi:10.1158/0008-5472.can-07-0077 (2007).
- 17 Veeravagu, A. *et al.* Integrin alpha(v)beta(3)-Targeted Radioimmunotherapy of Glioblastoma Multiforme. *Clinical Cancer Research* **14**, 7330-7339, doi:10.1158/1078-0432.ccr-08-0797 (2008).
- 18 Lesniak, M. S. & Brem, H. Targeted therapy for brain tumours. *Nature Reviews Drug Discovery* **3**, 499-508 (2004).
- 19 Ekstrand, A. J., Sugawa, N., James, C. D. & Collins, V. P. Amplified and rearranged epidermal growth-factor receptor genes in human glioblastomas reveal deletions of sequences encoding portions of the N-terminal and or C-terminal tails. *Proc. Natl. Acad. Sci. U. S. A.* **89**, 4309-4313 (1992).
- 20 Humphrey, P. A. *et al.* Antisynthetic peptide antibody reacting at the fusion junction of deletion mutant epidermal growth-factor receptors in human glioblastoma. *Proc. Natl. Acad. Sci. U. S. A.* **87**, 4207-4211 (1990).
- 21 Vivanco, I. & Sawyers, C. L. The phosphatidylinositol 3-kinase-AKT pathway in human cancer. *Nature Reviews Cancer* **2**, 489-501, doi:10.1038/mrc839 (2002).
- 22 Yamoutpour, F. *et al.* Gene silencing for epidermal growth factor receptor variant III induces cell-specific cytotoxicity. *Molecular Cancer Therapeutics* **7**, 3586-3597, doi:10.1158/1535-7163.mct-08-0653 (2008).

- 23 Yu, W. W., Qu, L. H., Guo, W. Z. & Peng, X. G. Experimental determination of the extinction coefficient of CdTe, CdSe, and CdS nanocrystals. *Chemistry of Materials* **15**, 2854-2860, doi:10.1021/cm034081k (2003).
- 24 Li, J. J. *et al.* Large-scale synthesis of nearly monodisperse CdSe/CdS core/shell nanocrystals using air-stable reagents via successive ion layer adsorption and reaction. *Journal of the American Chemical Society* **125**, 12567-12575, doi:10.1021/ja0363563 (2003).
- 25 Xie, R. G., Kolb, U., Li, J. X., Basche, T. & Mews, A. Synthesis and characterization of highly luminescent CdSe-Core CdS/Zn_{0.5}Cd_{0.5}S/ZnS multishell nanocrystals. *Journal of the American Chemical Society* **127**, 7480-7488, doi:10.1021/ja042939g (2005).
- 26 Liu, W. *et al.* Compact biocompatible quantum dots functionalized for cellular imaging. *Journal of the American Chemical Society* **130**, 1274-1284, doi:10.1021/ja076069p (2008).
- 27 Susumu, K. *et al.* Enhancing the stability and biological functionalities of quantum dots via compact multifunctional ligands. *Journal of the American Chemical Society* **129**, 13987-13996, doi:10.1021/ja0749744 (2007).
- 28 Kida, S. *et al.* Studies on heterobifunctional cross-linking reagents, 6-maleimidohexanoic acid active esters. *Chemical & Pharmaceutical Bulletin* **55**, 685-687 (2007).
- 29 Kamruzzahan, A. S. M. *et al.* Antibody linking to atomic force microscope tips via disulfide bond formation. *Bioconjugate Chemistry* **17**, 1473-1481, doi:10.1021/bc060252a (2006).
- 30 Bauhuber, S., Hozsa, C., Breunig, M. & Göpferich, A. Delivery of Nucleic Acids via Disulfide-Based Carrier Systems. *Advanced Materials* **21**, 3286-3306 (2009).
- 31 Chiu, Y. L., Ali, A., Chu, C. Y., Cao, H. & Rana, T. M. Visualizing a correlation between siRNA localization, cellular uptake, and RNAi in living cells. *Chemistry & Biology* **11**, 1165-1175, doi:10.1016/j.chembiol.2004.06.006 (2004).
- 32 Xie, J. *et al.* Ultrasmall c(RGDyK)-coated Fe₃O₄ nanoparticles and their specific targeting to integrin $\alpha(v)\beta(3)$ -rich tumor cells. *Journal of the American Chemical Society* **130**, 7542-+, doi:10.1021/ja802003h (2008).
- 33 Cai, W. B. *et al.* Peptide-labeled near-infrared quantum dots for imaging tumor vasculature in living subjects. *Nano Letters* **6**, 669-676, doi:10.1021/nl052405t (2006).

- 34 Berry, C. C. Intracellular delivery of nanopartides via the HIV-1 tat pepticle. *Nanomedicine* **3**, 357-365, doi:10.2217/17435889.3.3.357 (2008).
- 35 Ruan, G., Agrawal, A., Marcus, A. I. & Nie, S. Imaging and tracking of tat peptide-conjugated quantum dots in living cells: new insights into nanoparticle uptake, intracellular transport, and vesicle shedding. *Journal of the American Chemical Society* **129**, 14759-14766, doi:10.1021/ja074936k (2007).
- 36 Peng, Z. A. & Peng, X. G. Formation of high-quality CdTe, CdSe, and CdS nanocrystals using CdO as precursor. *Journal of the American Chemical Society* **123**, 183-184 (2001).
- 37 Peng, Z. A. & Peng, X. G. Nearly monodisperse and shape-controlled CdSe nanocrystals via alternative routes: Nucleation and growth. *Journal of the American Chemical Society* **124**, 3343-3353, doi:10.1021/ja0173167 (2002).
- 38 Qu, L. H., Peng, Z. A. & Peng, X. G. Alternative routes toward high quality CdSe nanocrystals. *Nano Letters* **1**, 333-337, doi:10.1021/nl015532 (2001).
- 39 Qu, L. H., Yu, W. W. & Peng, X. P. In situ observation of the nucleation and growth of CdSe nanocrystals. *Nano Letters* **4**, 465-469, doi:10.1021/nl035211r (2004).
- 40 Chirakul, P., Perez-Luna, V. H., Owen, H., Lopez, G. P. & Hampton, P. D. Synthesis and characterization of amine-terminated self-assembled monolayers containing diethylene glycol linkages. *Langmuir* **18**, 4324-4330, doi:10.1021/la015703o (2002).
- 41 Mantovani, G. *et al.* Design and synthesis of N-maleimido-functionalized hydrophilic polymers via copper-mediated living radical polymerization: A suitable alternative to PEGylation chemistry. *Journal of the American Chemical Society* **127**, 2966-2973, doi:10.1021/ja0430999 (2005).
- 42 Nielsen, O. & Buchardt, O. Facile synthesis of reagents containing a terminal maleimido ligand linked to an active ester. *Synthesis-Stuttgart*, 819-821 (1991).
- 43 Derfus, A. M., Chan, W. C. W. & Bhatia, S. N. Probing the cytotoxicity of semiconductor quantum dots. *Nano Letters* **4**, 11-18, doi:10.1021/nl0347334 (2004).
- 44 Kirchner, C. *et al.* Cytotoxicity of colloidal CdSe and CdSe/ZnS nanoparticles. *Nano Letters* **5**, 331-338, doi:10.1021/nl047996m (2005).
- 45 Meyer, A., van Golen, C. M., Kim, B., van Golen, K. L. & Feldman, E. L. Integrin expression regulates neuroblastoma attachment and migration. *Neoplasia* **6**, 332-342, doi:10.1593/neo.03445 (2004).

- 46 Martiniova, L. *et al.* Characterization of an animal model of aggressive metastatic pheochromocytoma linked to a specific gene signature. *Clinical & Experimental Metastasis* **26**, 239-250, doi:10.1007/s10585-009-9236-0 (2009).
- 47 Li, Z. B. *et al.* ⁶⁴Cu-Labeled "Tetrameric and octameric RGD peptides for small-animal PET of Tumor alpha(v)beta(3) integrin expression. *Journal of Nuclear Medicine* **48**, 1162-1171, doi:10.2967/jnumed.107.039859 (2007).
- 48 Wang, M. Y. *et al.* Mammalian target of rapamycin inhibition promotes response to epidermal growth factor receptor kinase inhibitors in PTEN-Deficient and PTEN-intact glioblastoma cells. *Cancer Research* **66**, 7864-7869, doi:10.1158/0008-5472.can-04-4392 (2006).
- 49 Jung, J. *et al.* Selective inhibition of human brain tumor cells through multifunctional quantum-dot-based siRNA delivery. *Angewandte Chemie-International Edition* **49**, 103-107, doi:10.1002/anie.200905126 (2010).

CHAPTER IV

GRAPHITE-COATED MAGNETIC NANOPARTICLES AS MULTIMODAL IMAGING PROBES AND HYPERTHERMIA AGENTS FOR BRAIN TUMOR CELLS

A. Introduction

Magnetic nanomaterials have shown great potential for cancer research as non-invasive imaging probes as well as multifunctional therapeutics¹⁻³. The unique physical and chemical properties of magnetic nanoparticles (MNPs) have enabled their use in a variety of applications, including magnetic resonance imaging (MRI), drug/gene delivery⁴⁻⁶, magnetic mechanotransduction⁷ and hyperthermia⁸. Recent efforts in cancer therapy have demonstrated the application of hyperthermia, which involves localized heating of cancerous cells or tissues, as an adjuvant to chemotherapy and radiation to improve their efficacy⁹. Hyperthermia typically involves increasing the local temperature of the tumor region to 42-46 °C over a given time period, ultimately resulting in apoptosis of heat-sensitized cancer cells¹⁰. One of the best methods of achieving a localized hyperthermal effect is to use MNPs and subsequently apply electromagnetic fields following their cellular uptake/localization^{8,11}. However, to harness the full potential of magnetic nanomaterials in cancer diagnosis and therapy, it is important to focus on: i) the development of a novel synthetic route for obtaining core-shell metal alloy MNPs in high yields, ii) the surface modification of these MNPs with specific biomolecules for targeted delivery, and iii) the further exploration of their excellent magnetic properties for molecular imaging (e.g. Raman spectroscopy, MRI) and therapeutic approaches (e.g. hyperthermia, gene delivery).

Significant advances have been made in synthesizing various multifunctional MNPs, including metals¹², metal oxides¹³ metal alloys^{14,15} and metal graphitic-shell nanomaterials^{16,17} for biological and clinical applications. However, in spite of their superior magnetic properties, the use of a metal alloy magnetic nanomaterial such as iron

cobalt (FeCo) has been limited due to high susceptibility to oxidation and potential toxicity concerns. Therefore, the enclosure of the FeCo core within a graphitic carbon shell has been of interest to obtain metal alloy MNPs with higher stability and enhanced magnetic moments without the aforementioned problems. The graphitic carbon shell-coated FeCo nanoparticles (NPs) have been previously synthesized by electric arc-discharge, high temperature thermal decomposition^{18,19} or chemical vapor deposition²⁰. However, these methods have severe limitations including low production yields, the lack of an environmentally-friendly approach and complicated synthetic methodologies.

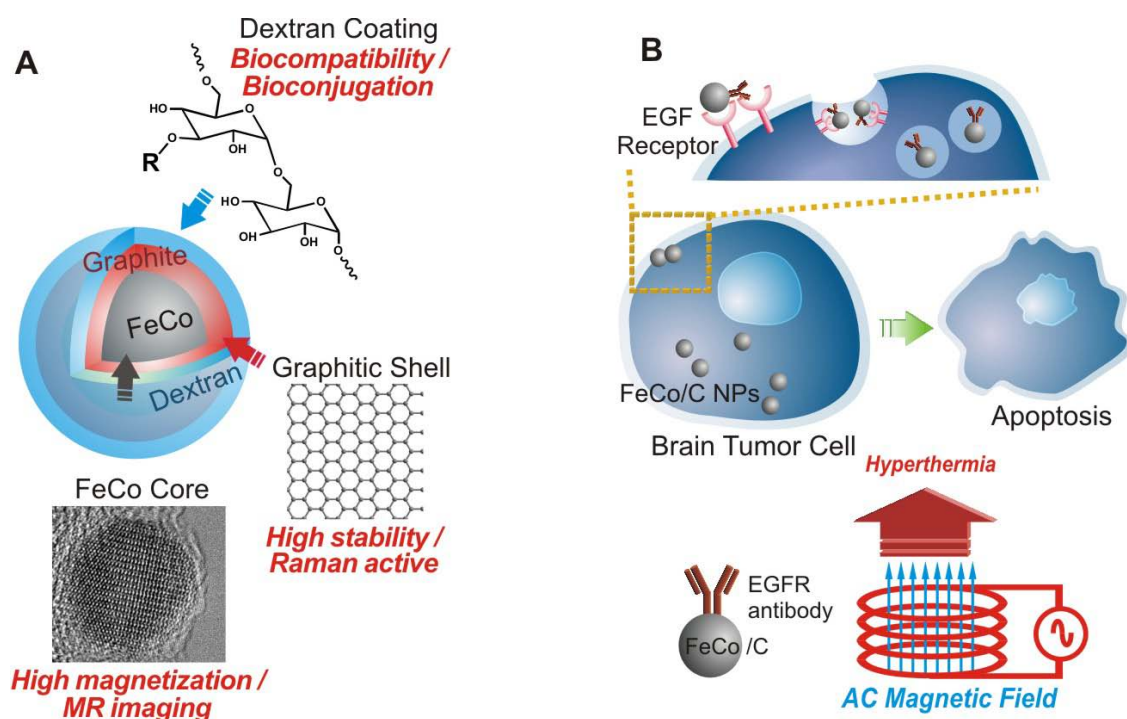


Figure IV-1. Multimodal magnetic FeCo-graphite nanoparticles for multimodal imaging and targeted brain tumor therapy. (A) Detailed structure of the MNPs depicting the highly magnetic FeCo core, protective Raman active graphite shell and the biocompatible dextran coating (B) Inhibition of proliferation and induction of apoptosis via hyperthermia using FeCo/C NP constructs. Copyright Wiley-VCH Verlag GmbH & Co. KGaA. Reproduced with the permission of Ref. 47

Herein, we describe the novel synthesis of multifunctional magnetic nanoparticles (MNPs) with an iron cobalt core and a graphitic carbon shell (FeCo/C) for targeting brain tumor cells (bTCs) to demonstrate hyperthermia-based therapy resulting in the significant inhibition of tumor cell proliferation and induction of apoptosis (Figure 1). In parallel, we also demonstrated that our MNPs can be used as highly sensitive imaging probes for *in vivo* MRI and *in vitro* Raman imaging. As a model in this study, we used glioblastoma multiforme (GBM) cell line, the most malignant and difficult-to-treat brain tumor. We hypothesized that the targeted delivery of our MNPs to bTCs and subsequent hyperthermal treatment would selectively damage the bTCs thereby inhibiting their proliferation and inducing apoptosis. Hence, this MNP-based therapeutics could be used for the simultaneous imaging and therapy of malignant tumors both *in vitro* and *in vivo*.

B. Materials and Methods

1. Synthesis of MNPs

1. 1. Synthesis of FeCo/C NPs

The novel synthetic methods 7 nm /11nm FeCo/C NPs are described in following results and discussion session in detail.

1. 2. Synthesis of Fe₃O₄ NPs

1. 2. 1. Synthesis of Iron-Oleate Complex

Monodisperse iron oxide (magnetite; Fe₃O₄) nanoparticles (NPs), 11nm in diameter were synthesized according to previously reported protocol¹⁹. Briefly, the iron-oleate complex was prepared by dissolving iron chloride (FeCl₃.6H₂O, 4 mmol, Aldrich, 98%) and sodium oleate (12mmol) in a mixture solvent composed of 8 ml ethanol, 6 ml distilled water and 14 ml hexane under inert atmosphere. The resulting solution was then heated to 70 °C and maintained at that temperature for four hours. Thereafter, the upper organic layer containing the iron oleate complex was washed three times with distilled water in a separatory funnel to remove traces of unreacted starting materials. Following washing, hexane was evaporated off to yield iron-oleate complex in a waxy solid-like form.

1. 2. 2. Synthesis of Fe₃O₄ NPs

3.6 g of the previously synthesized iron-oleate complex and 0.57 g of oleic acid were dissolved in 20 g of 1-octadecene at room temperature. The resulting mixture was

heated upto 320 °C at a constant heating rate of 5 °C min⁻¹ and kept at that temperature for 30 min. At 320 °C, the initial transparent reddish orange solution became turbid and brownish black. The resulting solution was then cooled down to room temperature and the nanocrystals were then precipitated out using ethanol and centrifuged to yield monodisperse 11 nm Fe₃O₄ nanoparticles. The nanoparticles were then characterized using transmission electron microscopy.

1. 3. Physical Characterization of the FeCo/C NPs

The NPs were characterized using XRD (Bruker D8 X-ray diffractometer with CuK α radiation (Ni filter)), TEM (Tecnai G2 and JEOL JEM-2010F high-resolution transmission electron microscope operated at an accelerating voltage of 200 kV), Raman spectroscopy (Renishaw Micro-Raman 2000 with He-Ne laser excitation of 632.8 nm) and SQUID magnetometry (Quantum design magnetometer). The stoichiometry of Fe and Co and metal concentration in the NPs were determined using Inductively Coupled Plasma-Atomic Emission Spectrometer (ICP-AES, data not shown).

2. Surface Modification of the FeCo/C NPs with the Functionalized Dextrans

200 mg of FeCo/C magnetic NPs were dispersed in 10 ml of NaOH (0.5 M) and this suspension was mixed with a solution of 400 mg of functionalized dextran in NaOH (0.5 M) prepared previously. The mixture was sonicated for 24 h at 30 °C and the coated NPs were separated magnetically and washed thrice with water to remove the unreacted functionalized dextran.

2. 1. T₂ Measurements

Aqueous solutions of varying concentrations of FeCo/C NPs were used for T_2 measurements using a 4.7 T MRI instrument with a 72 mm volume coil (Bruker, Germany). The T_2 values of various phantom solutions were obtained from the Carr-Purcell-Meiboom-Gill (CPMG) sequence at room temperature (TR = 10 s, 128 echoes with 7.4 ms even echo space, number of acquisition = 1, spatial resolution = $391\ \mu\text{m} \times 391\ \mu\text{m}$, section thickness = 1 mm).

2. 2. Conjugation of Targeting Molecules to FeCo/C NPs

Amine reactive FeCo/C-Np-Dex (Nitrophenyl ester conjugated dextran; Np-Dex) magnetic NPs were dispersed in degassed PBS. To 50 μl of the above FeCo/C solution (9 mg/ml), 20 μl of EGFR (Epidermal Growth Factor Receptor) antibody (0.5 mg/ml, BD Pharmingen, San Diego, CA) or 25 μl of cRGD solution (5mM, American Peptide Company, Sunnyvale, CA) was added. The reaction solution was stirred for 3-4 hours at 100 rpm. After conjugation, unreacted biomolecules were removed by three cycles of ultracentrifugation at 14,000 rpm and subsequent washing with PBS.

3. Cell Culture of U87-EGFP and other Control cells

For the hyperthermia, MR imaging, and Raman study, EGFP overexpressed U87 cells (U87-EGFP) and several controls cells (PC-12 and Astrocytes) were cultured using previously reported methods, albeit with minor modifications. For U87-EGFP, DMEM with high glucose, 10% FBS, 1% Streptomycin-penicillin and 1% Glutamax (Invitrogen, Carlsbad, CA) were used as basic components of growth media including Geneticin G418 (100 $\mu\text{g}/\text{ml}$, Invitrogen) as a selection marker. Astrocytes were cultured in the above

mentioned growth media without any selection markers, while PC-12 cells were cultured in DMEM with 10% horse serum, 5% FBS and 1% Streptomycin-penicillin. All cells were cultured at 37 °C in humidified 5% CO₂ atmosphere.

4. *In Vitro* Imaging

4. 1. MRI Imaging

For the MR imaging of cell pellets, cells were cultured in 6-well plates up to 80-90% confluency. After 2 hours of treatment with FeCo/C MNPs and Fe₃O₄ MNPs (90-120µg/ml) in Opti-MEM, cells were washed three or four times with DMEM and incubated in the growth media for 24-48 hours. Cells with the NPs were trypsinized and washed with PBS. 10% formaldehyde solution (100~150µl) was added to the detached cells in a 500 µl eppendorf tube and centrifuged at 3500 rpm for mild fixation. After removing the supernatant, cells were incubated in 10% formaldehyde solution for 10-15 mins. By repeating this procedure, similar amount of cells for each nanoparticles - FeCo/C MNPs and Fe₃O₄ MNPs- were collected and these were stored in 10% formaldehyde solution under 4°C. For the MR imaging of the single layer of the cells with nanoparticles, U87-EGFP cells were grown on 15mm diameter plastic cover slips (EMS, Hatfield, PA) in 12-well plates. After treatment with two different nanoparticles - FeCo/C MNPs and Fe₃O₄ MNPs, cells were fixed with 4% paraformaldehyde solution. MRI imaging was performed at 4.7 T using the following parameters: point resolution: 156 × 156 µm, section thickness of 0.6 mm, TE = 60 ms, TR = 4000 ms, number of acquisitions = 1.

4. 2. Raman Imaging

Internalization of nanoparticles into U87-EGFP cells was performed in 48-well plates using the above mentioned conditions. To each well, FeCo/C MNPs with different number of carbon graphite layers were added using the previously mentioned conditions. The cells were then imaged using a Renishaw Micro-Raman 2000 instrument with He-Ne laser excitation of 632.8 nm.

5. *In vivo* MR Imaging

We injected 11 nm FeCo/C NPs (10 μ L, 0.25 mg of Fe) and Resovist (100 μ L, 2.5 mg of Fe) into a rat's tail vein. T₂-weighted MR images before injection and at 30 minute intervals post-injection were obtained using a 4.7 T MRI instrument (Bruker, Germany). We used the following parameters: resolution of $234 \times 256 \mu\text{m}$, section thickness of 2.0 mm, TR = 400 ms, TE = 15 ms, number of acquisitions = 8. Flip angle = 30°.

6. Hyperthermia Measurements

All the AC magnetic field experiments were conducted using a Comdel CLF-5000 RF generator in a magnetic field with a frequency of 334 kHz and at amplitude of 150 Oe. To measure the temperature variation of the magnetic NPs suspensions, 2 mL of each suspension was taken in a double- walled test tube where the space between the outer and inner walls was evacuated to minimize any heat loss. The tube was placed at the center of the induction heater coil and an alcohol thermometer was used to measure the temperature increase in the suspension, thereby negating the electrical and magnetic effects of the generator on the thermometer. For hyperthermia measurements in cells, 15 mm diameter cover glass (Fisher scientific, Pittsburg, PA) was autoclaved and sterilized under UV light.

U87-EGFP cells were cultured to 40-60 % confluency on the cover glasses in 24-well plates. FeCo/C NPs or Fe₃O₄ NPs in Opti-MEM (Invitrogen, Carlsbad, CA) were added at various concentrations (10, 30, 60, 90 µg/ml). After 2-4 hrs of incubation, cells were washed with DMEM to remove non-specific attachment of NPs and the media was changed to growth media. After, overnight incubation, hyperthermia study was carried out. For target-specific hyperthermia experiments, control cells such as PC-12 and astrocytes were co-cultured with U87-EGFP (about 1:1 ratio). EGFR antibody or cRGD conjugated FeCo/C NPs were used as a hyperthermia agents at different concentrations (1 µg/ml and 5 µg/ml). Detailed procedure was same as the one used for FeCo/C and Fe₃O₄ in U87-EGFP cells.

C. Results and Discussion

1. The synthesis of high performance FeCo/C NPs and their magnetic properties

We synthesized graphitic carbon-protected iron cobalt (FeCo/C) nanoparticles (7 and 11 nm in diameter) with a body-centered cubic crystalline structure. The highly stable FeCo/C NPs were formed by heating an aqueous mixture of iron and cobalt salts with sucrose as a carbon source under specific temperature and pressure conditions in a simple hydrothermal synthetic chamber, followed by annealing at 1000 °C under an inert atmosphere^{3,15,21,22}. The hydrothermal treatment at high pressure induces the dehydration of the carbohydrates (sucrose in our case) and subsequent carbonization, resulting in carbon ions being predominantly positioned at the surface of the FeCo core. Consequently, the carbon graphite shell grows on the FeCo core during the annealing process which leads to graphitic carbon-protected iron cobalt (FeCo/C) NPs^{19,23}. High resolution transmission electron microscopy (HR-TEM) confirmed the monodispersity and narrow size distribution of the nanoparticles in Figure 2A and clearly showed the crystalline structure of the FeCo core (Figure 2B, d spacing = 1.98 Å). The X-ray diffraction (XRD) peak positions in Figure 2C confirm the presence of a crystalline body-centered cubic FeCo core and graphite shell. The absence of oxide peaks in the diffractogram further supports our hypothesis that the graphitic-carbon coating protects the metal-alloy core from aerial oxidation. Raman spectroscopic analysis showed the presence of intense peaks at 1320 cm^{-1} (D-band) and 1610 cm^{-1} (G-band), which provides evidence for the presence of graphitic-carbon shells (Figure 2d). The variation in shell thickness could be easily

monitored using Raman imaging (marked by arrows in Figure 2D). In addition, the size of the core and the shell could be easily tuned by varying the FeCo/sucrose molar ratio and the reaction temperature (Figure 3A). The ability to tune the size of the nanoparticles is essential for biological applications, since there is an optimal nanoparticle size that facilitates nanoparticle-mediated cellular responses for specific biological effects²⁴. We also characterized the magnetic properties of our FeCo/C NPs using a superconducting quantum interference device (SQUID). Our FeCo/C NPs were found to display remarkable superparamagnetic behaviors at room temperature as suggested by the significantly higher value of saturation magnetization (M_s) for our FeCo/C NPs as compared to that of the commercially available Fe_3O_4 (Figure 2E). This was attributed to the higher magnetic moments of the FeCo/C NPs as a result of the high temperature annealing. The crystallinity of the FeCo/C NPs increased after annealing at 1000 °C (Figure 3B), thereby resulting in an overall increase in its magnetic moment.

In this work, our multifunctional magnetic nanoparticles (MNPs: FeCo/C) have several advantages over other conventional magnetic nanoparticles such as Fe_2O_3 and Fe_3O_4 : i) FeCo exhibits an excellent magnetization value (e.g. 11 nm of FeCo ~235 emu/g), has high curie temperature, and high magnetic anisotropy energies, all of which are critical to enhance their potential for biomedical applications such as MRI and hyperthermia ii) the number of graphite shell layers can be controlled by our synthetic method, which would lead to improved Raman signal intensity for detecting cancer cells, and iii) the nanoparticles are chemically inert due to the presence of a graphitic carbon shell^{20,23} and they can be made biocompatible by appropriate surface modifications (e.g. dextran-ligand coating). Moreover, compared to conventional methods^{16,18-20} for the synthesis of

core-shell metal alloy magnetic nanomaterials, our novel hydrothermal synthetic approach has several advantages such as relatively milder synthetic conditions, low environmental impact, cost-effectiveness, ease of scalability (Figure 3C), exclusion of toxic solvents and size separation techniques.

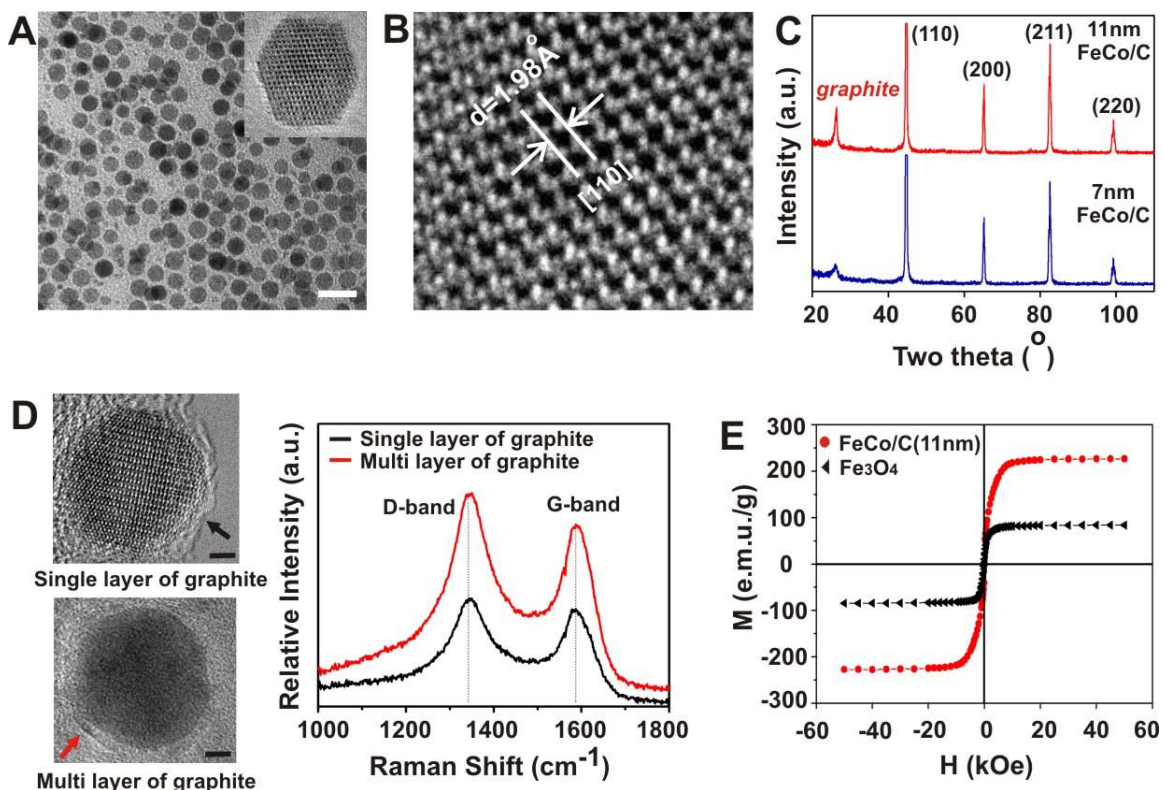


Figure IV-2. Structural and magnetic properties of the FeCo/C NPs. (A): TEM image of the 11 nm nanoparticles (Scale bar = 20 nm). (B): HR-TEM image of the nanoparticles showing the crystalline lattice structure of the FeCo core. (C): Powder-XRD for the 7 nm and 11 nm nanoparticles showing the presence of a body-centered cubic crystalline core and graphitic shell. (D): Raman spectrum (excitation of 632.8 nm) of the 11 nm nanoparticles with single and multiple carbon shells (marked by arrows), showing the D and G bands of graphitic carbon (Scale bar = 2nm) (E): Room-temperature magnetization versus applied magnetic field for 11 nm FeCo/C NPs (red symbols) and Fe_3O_4 (black symbols). Note that no hysteresis loop exists owing to the superparamagnetism of the nanoparticles. Copyright Wiley-VCH Verlag GmbH & Co. KGaA. Reproduced with the permission of Ref. 47

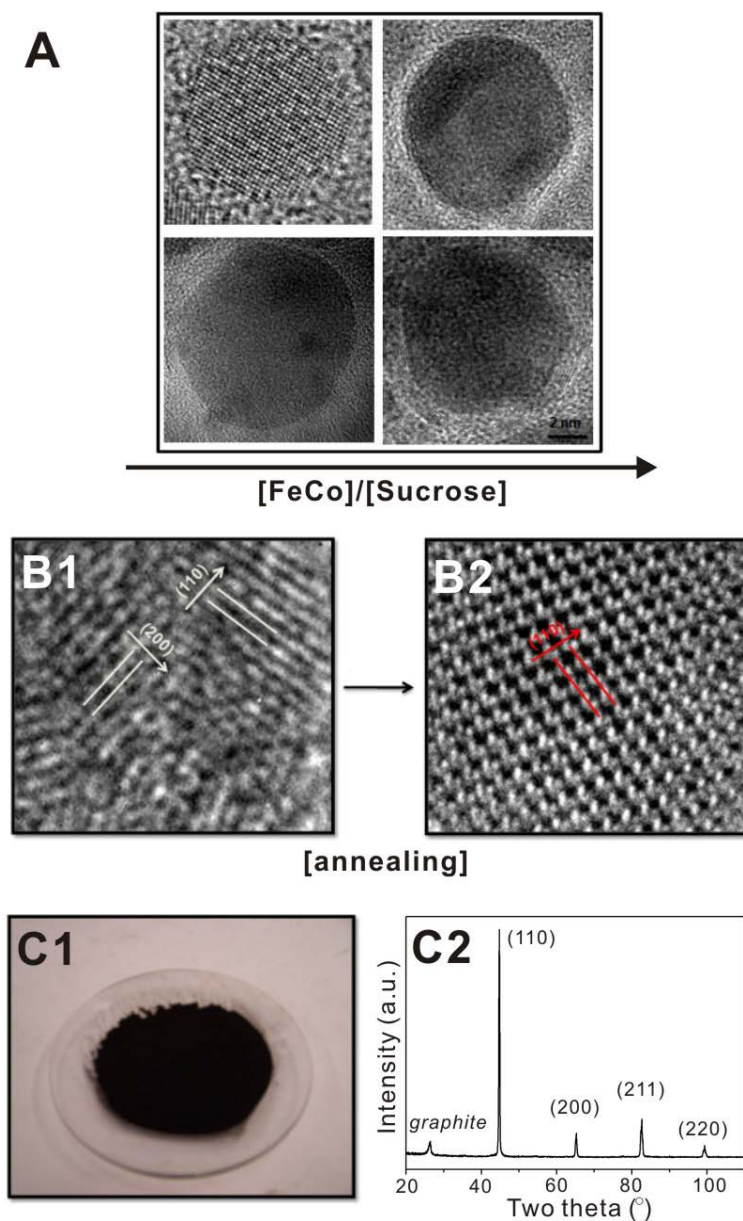


Figure IV-3. (A): HR-TEM image of FeCo/C MNPs as a function of [FeCo]/Sucrose ratio. The shell thickness can be easily controlled by varying the [Fe/Co]/Sucrose ratio. **(B1): HR-TEM image of as-prepared FeCo/C NPs (B2): HR-TEM image of FeCo/C MNPs after annealing at 1000 °C.** The identification of lattice fringes for as-prepared FeCo/C NPs indicated the presence of chemically disordered phase, whereas the annealed FeCo/C NPs show that the particles have uniform lattice fringes across the particles, which is attributed to good crystallinity. **(C1): Photograph of the air-stable FeCo/C NPs obtained via a large-scale synthesis (C2): the corresponding powder-XRD spectrum.**

1. 1. The synthesis of FeCo/C NPs

7 nm FeCo/C NPs were prepared by dissolving $\text{Fe}(\text{NO}_3)_3 \cdot 9\text{H}_2\text{O}$ (2.424 g, 6 mmol) and $\text{Co}(\text{NO}_3)_2 \cdot 6\text{H}_2\text{O}$ (1.164 g, 4 mmol) in 30 mL of distilled water and then 2.9 mmol of sucrose was added. The mixture was stirred vigorously to form a clear solution and then placed in a 45 mL capacity Teflon-lined stainless steel autoclave, which was heated in an oven to 190 °C for 9h. For 11 nm FeCo/C NPs, the mixture was heated to 220 °C for 9h. The products were washed several times with distilled water, filtered off and finally dried in a drying oven at 80 °C for 5h. Subsequently, the dried products were annealed at 1000 °C for 3h under Ar atmosphere to allow for the growth of the carbon graphite shell on the surface of FeCo NPs. To remove the remaining carbon graphite, the products were washed several times with distilled water and separated using a bar magnet. The number of graphite shells was controlled by varying the amount of sucrose between 2.9 mmol and 8.8 mmol. To prepare large amounts of FeCo/C magnetic NPs in one step, 13.5744 g of $\text{Fe}(\text{NO}_3)_3 \cdot 9\text{H}_2\text{O}$ (33.6 mmol) and 6.5184 g of $\text{Co}(\text{NO}_3)_2 \cdot 6\text{H}_2\text{O}$ (22.4 mmol) were added to 30 mL of distilled water, which was followed by the addition of 14.5 mmol of sucrose under the above mentioned reaction conditions. The amount of the FeCo/C NPs was as much as 5 g with a yield greater than 95 %.

2. The MR/Raman imaging of FeCo/C for single cell and in vivo

Highly sensitive multimodal imaging nanomaterials have gained much attention as diagnostic tools for specific cancers such as breast and brain cancers. Current biomedical imaging techniques including magnetic resonance imaging (MRI), Raman imaging, positron emission tomography (PET), and computed X-ray tomography (CT) are vital in the diagnosis of various diseases. However, most of the nanomaterials used as imaging and contrast agents lack the capability for comprehensive imaging^{21,25}. Therefore, nanomaterials incorporating multiple imaging modalities are quickly becoming important tools for state-of-the-art biomedical research and clinical diagnostics and therapeutics. To investigate the capability of our FeCo/C NPs as multimodal imaging nanoprobe, we focused on two important cancer-imaging methods, *in vivo* MRI and *in vitro* Raman imaging, both of which provide complementary information about microenvironments of brain tumors at the tissue level and/or cellular level. MRI enables non-invasive high-quality anatomical information of brain cancerous tissues^{26,27} while Raman spectral imaging allows for the investigation of subcellular compartments of tumors and can provide a unique spectral fingerprint profile of biomolecular structures of tumor cells²⁸. Particularly, Raman spectral imaging has recently shown to be a powerful diagnostic tool for cancer research. For example, carbon nanotube (CNT)-based Raman detection methods for cancer cells have been successfully demonstrated²⁸⁻³⁰. In order to test the capability of our MNPs as MRI contrast agents, the transverse relaxation times (T_2) of the water protons were measured in a specific magnetic field and their values were compared to those of the commercially available MRI contrast agent, Resovist. Both the 7 and 11 nm FeCo/C NPs exhibited higher relaxivity coefficient (r_2) and enhanced T_2 -weighted MR contrast as

compared to Resovist in Figure 3A and 3B. Characterization of our biocompatible dextran coated-FeCo/C NPs as *in vivo* MRI agents was performed by injecting the MNPs into the rat's tail vein. Preliminary MRI data showed that our nanoparticles accumulated in the liver, spleen and kidneys and their imaging contrast was significantly higher (about 10 times) than that of Resovist (Figure 3C). Furthermore, the analysis of *in vitro* Raman imaging results, where confocal microscopy was used to observe the NP-internalized U87 cell lines, confirmed that the intensity of the D- and G- bands of the graphitic-carbon shells was indeed proportional to the number of the carbon shells on the FeCo/C NPs in Figure 3D. This data strongly suggests that our FeCo/C NPs have a well-defined correlation and sensitive response when used as Raman imaging probes at the single cancer cell level. In Figure 5, there are more detailed MR images of in various cell lines (Figure 5A) and Raman image of single cell where FeCo/C NPs were internalized (Figure 5B3).

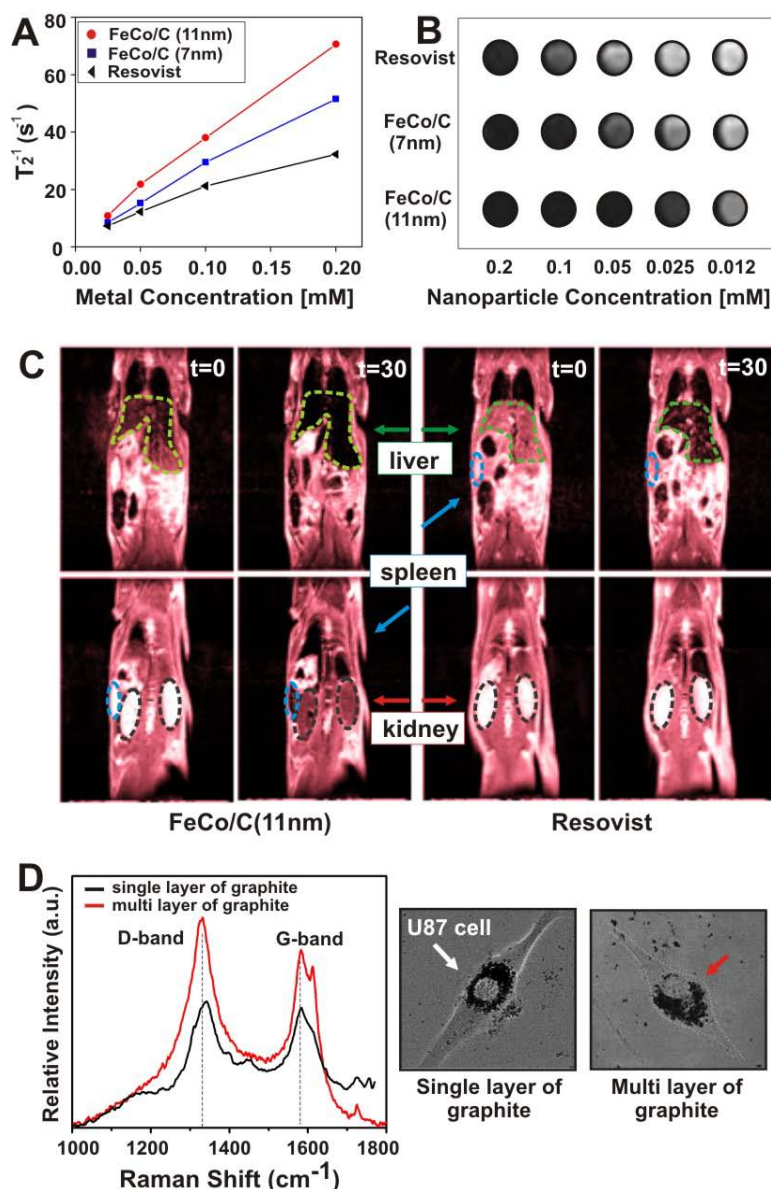


Figure IV-4. MR measurements and imaging of FeCo/C NPs and Resovist. (A) Concentration dependent T_2 measurements of FeCo/C NPs and Resovist solutions. (B) T_2 -weighted MR images of various nanoparticle solutions. The FeCo/C NPs show higher MR image contrast (several fold) as compared to Resovist, a traditional MRI contrast agent (C) T_2 -weighted MR images of a rat before ($t=0$ min) and 30 mins after ($t=30$ mins) injection of FeCo/C NPs (left) and Resovist (right) into a rat's tail vein. The nanoparticles were seen to localize in the liver (green arrow), spleen (blue arrow) and kidneys (red arrow) of the animal. Also, FeCo/C NPs show a higher imaging contrast at a lower concentration (0.25 mg of Fe) as compared to Resovist (2.5 mg of Fe). (D) Raman spectra of U87-EGFP cells treated with 11 nm FeCo/C NPs. The spectra show the capability of the FeCo/C NPs to be used as imaging agents at the single cell level. Copyright Wiley-VCH Verlag GmbH & Co. KGaA. Reproduced with the permission of Ref. 47

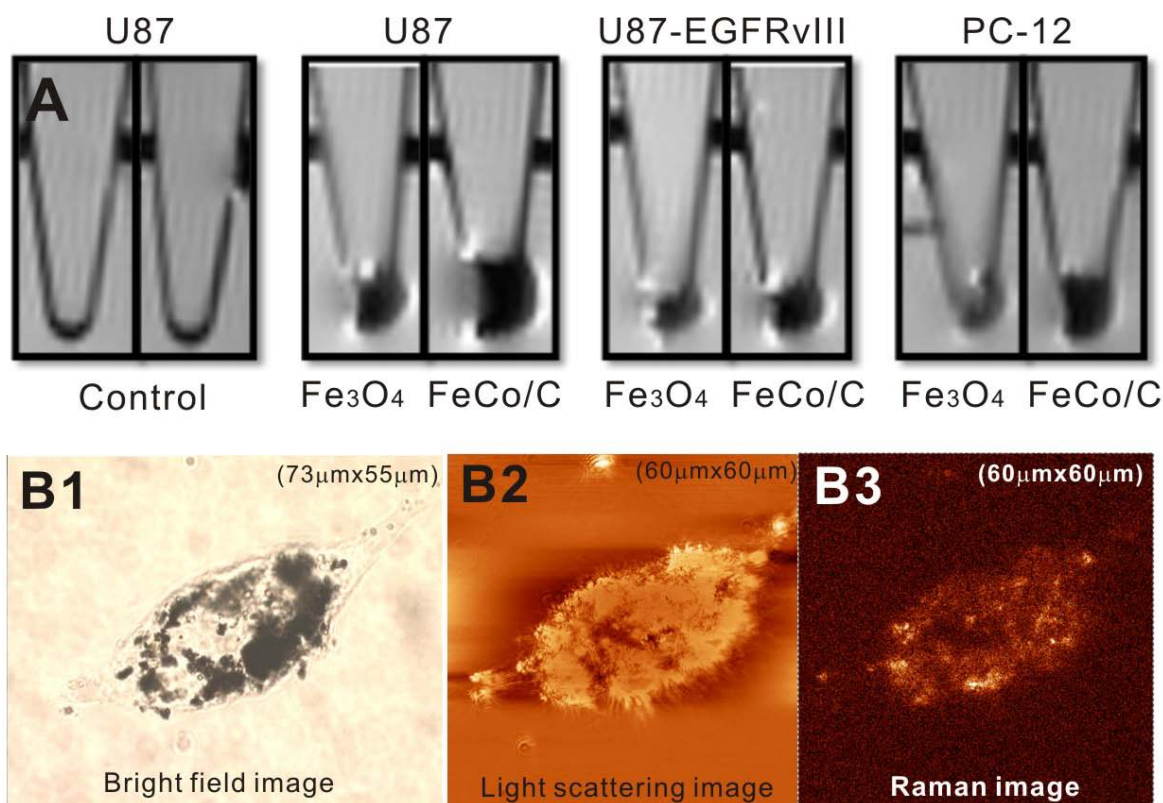


Figure IV-5. MR and Raman imaging of FeCo/C NPs in various cell lines (A): T₂-weighted MR contrast images of Fe₃O₄ and FeCo/C NPs in various cell samples. The FeCo/C NP-containing cells show a much higher T₂-weighted contrast evidenced by the darker color as compared to Fe₃O₄ NP-containing cells and control cells. **(B1):** Bright field image of single layer graphitic FeCo/C NPs internalized into U-87 cell. **(B2):** Scattering image of single layer graphitic FeCo/C NPs internalized into U-87 cell using 632.8 nm scanning laser light. **(B3):** Raman image of single layer carbon graphite encapsulated FeCo NPs internalized into U-87 cell.

3. Dextran-coated FeCo/C NPs

Another critical step to realize the full potential of our multimodal FeCo/C NPs for *in vitro/in vivo* biomedical applications (e.g. targeted drug/gene delivery, MRI, and hyperthermal therapy) is to make the nanoparticles biocompatible and modify the surface for achieving target specific intracellular delivery^{31,32}. Several strategies including coating with molecules such as dextran, have been successfully used for functionalizing magnetic nanoparticles and rendering them biocompatible^{31,33}. Hence, we synthesized a series of dextran derivatives (Figure 6A) and used them to coat our FeCo/C NPs (Figure 6B). The dextran-coated FeCo/C NPs were found to have excellent colloidal, pH, and salt stability without considerable aggregation over a period of 1 month (Figure 10). These dextran-modified FeCo/C NPs were then conjugated to specific targeting biomolecules, such as EGFR antibodies and cyclic-RGD (c-RGD) (Figure 7), to target glioblastoma cells and to improve their intracellular uptake. Typically, brain tumor cells (bTCs) express high levels of the integrin receptor protein $\alpha_v\beta_3$ which is shown to have a high binding affinity towards the c-RGD ligand³⁴. Similarly, EGFR antibodies are helpful for the targeted delivery of our MNPs into the bTCs. The conjugation of biomolecules such as EGFR antibodies and cyclic-RGD to our FeCo/C NPs not only increases transfection of our nanoparticles via receptor-mediated endocytosis, but also selectively targets the glioblastoma cells when administered *in vivo*^{33,35,36}.

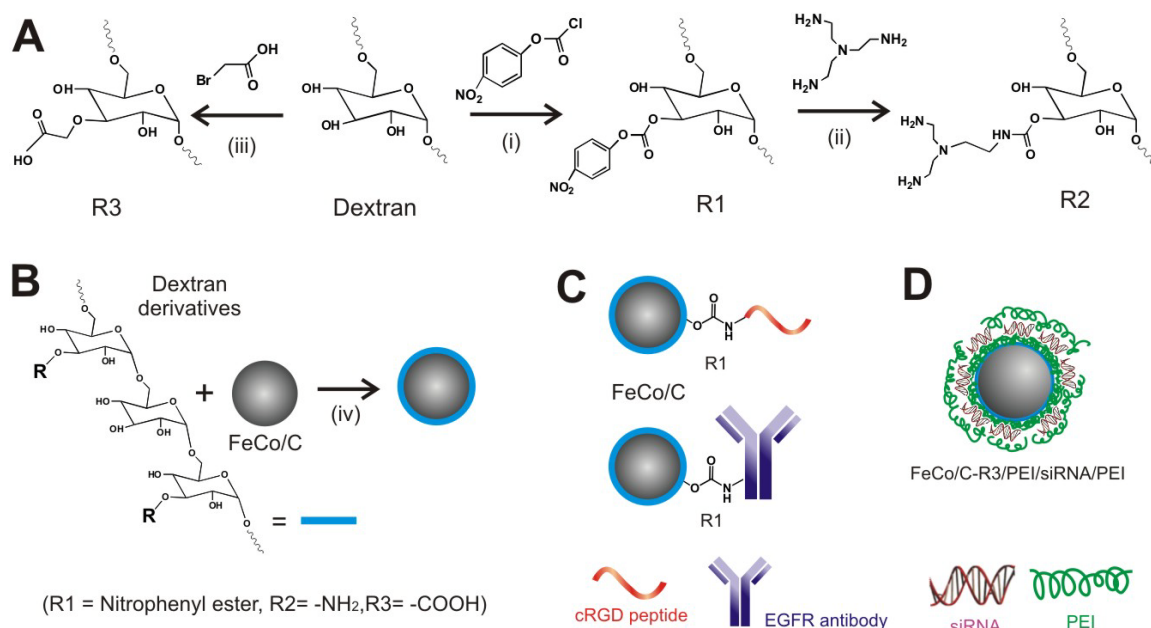


Figure IV-6. Synthesis of various dextran derivatives and coating with FeCo/C Nanoparticles for bioconjugation. (A): Synthesis of dextran derivatives terminated with 4-nitrophenyl chloroformate group (R1), -NH₂ group (R2) and -COOH group (R3). (B): Coating of the FeCo/C NPs with dextran derivatives to render them biocompatible and enable conjugation of biomolecules onto their surface. (C, D): Conjugation of EGFR antibody and cRGD peptide to the reactive functional groups present on the dextran coated FeCo/C NPs.

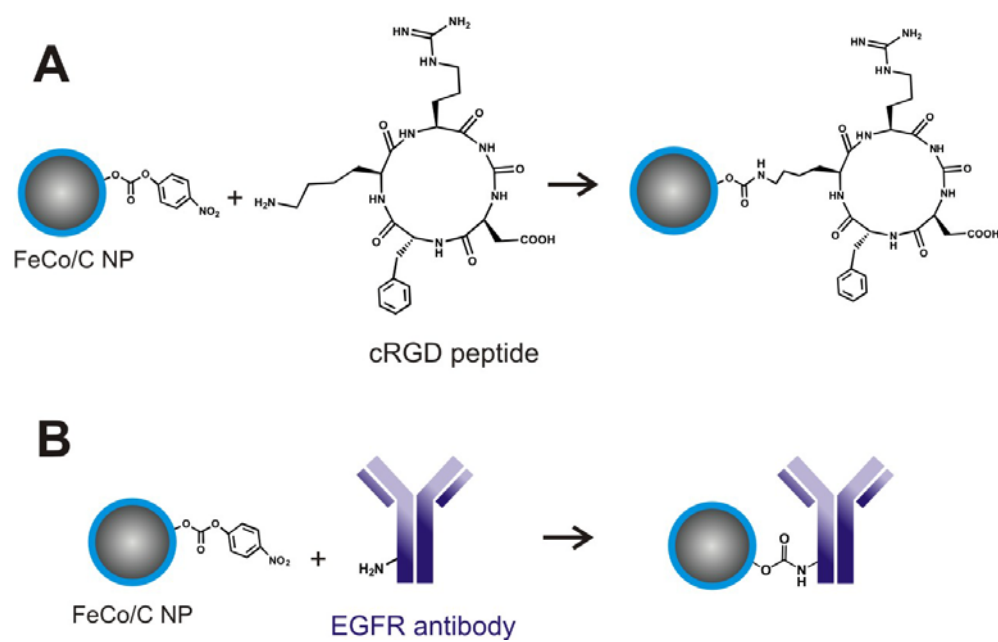


Figure IV-7. Bioconjugation strategies for cRGD peptide (A) and EGFR (B) antibody coupling to dextran coated FeCo/C nanoparticles with a functional group.

3. 1. Synthesis of amine functionalized Dextran

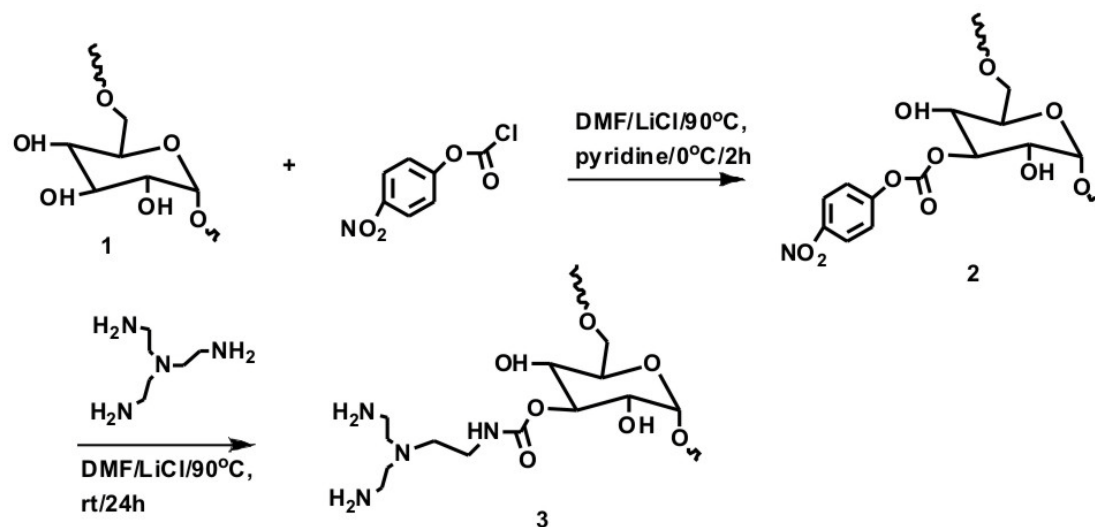
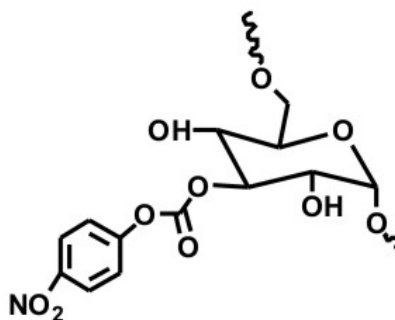


Figure IV-8. Synthesis of dextran functionalized with 4-nitrophenyl chloroformate groups and amine groups.

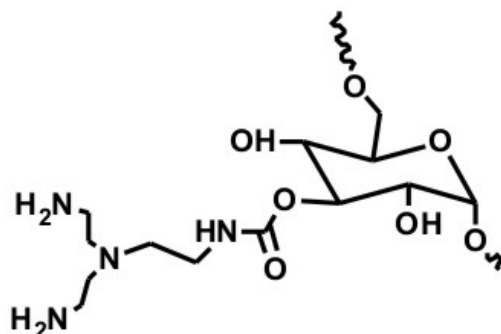
3. 1. 1. Dextran functionalized with 4-nitrophenyl chloroformate groups (4-NC dextran) (2)



Dextran functionalized with 4-nitrophenyl chloroformate groups (4-NC dextran) (2)

Scheme 1 shows the synthesis of 4-NC dextran³⁵. For a complete dissolution of dextran (**1**) in DMF, 15 g (92 mmol) dextran and 5.0 g (118 mmol, 2 w/v %) water-free lithium chloride (LiCl) were suspended in 250 ml DMF and stirred at 90 °C until a clear solution appears. The reaction mixture was cooled to 0 °C, and pyridine (4.2 mL, 52 mmol) was added to the dextran solution followed by 4-NC (10.5g, 52 mmol). The reaction mixture was stirred for 4 h at 0 °C, and finally the 4-nitrophenyl carbonated dextran was isolated by precipitation in cold ethanol, washed with diethyl ether, and dried under vacuum. Yield: 14.5 g, 97%. ¹H NMR (D₂O): δ 3.27-4.13 (m, dextran glucosidic protons), 4.68 (s, dextran anomeric proton), 7.83 and 8.67 (dd, aromatic protons).

3. 1. 2. Dextran functionalized with amine groups (3)



Dextran functionalized with amine groups (3)

For a complete dissolution of 4-NC dextran in DMF, 7 g (37 mmol) 4-NC dextran and 1.13 g (26.7 mmol, 1 w/v %) water-free LiCl were suspended in 56 mL DMF and stirred at 90 °C until a clear solution appeared. The solution was then cooled again to 0 °C. Tris(aminoethyl)amine (7 mL, 45 mmol) was dissolved in DMF (56 mL) and added drop

wise under stirring to the 4-NC dextran solution. The reaction was stirred for 24 h at room temperature. Subsequently, the product was isolated by precipitation in cold ethanol and washed several times with ethanol to remove *p*-nitrophenol. The product was filtrated and dried under vacuum. Finally the completion of the reaction was determined by a Ninhydrin color test and NMR spectroscopy. Yield: 4.6g, 66%. ^1H NMR ($\text{DMSO-}d_6$): δ 1.0 (t, amine protons), δ 2.42-2.57 (m, amine protons), δ 3.1-3.8 (m, dextran glucosidic protons), 4.08 (s, dextran glucosidic protons), 4.69 (s, dextran anomeric proton), 8.0 (s, amide protons).

3. 2. Synthesis of carboxyl functionalized Dextran

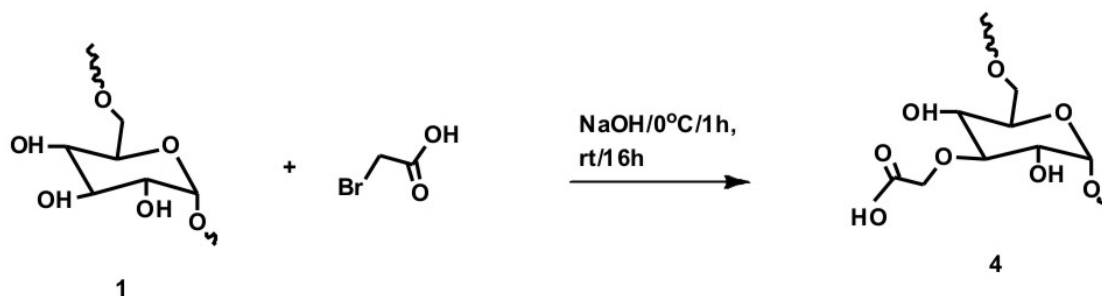
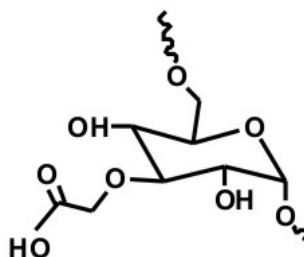


Figure IV-9. Synthesis of dextran functionalized with carboxyl groups.

3. 2. 1. Dextran functionalized with carboxyl groups (4)



Dextran functionalized with carboxyl groups (4)

Scheme 2 shows the representative synthesis for obtaining dextran functionalized by carboxyl groups (4). Carboxydextran was synthesized using the methods reported previously³⁶. 6 g dextran was dissolved in 20 mL 0.1 M NaOH. Then 1M bromoacetic acid (1.4 g) and 10 mL 2 M NaOH (0.8 g) were added to 10 mL of the dextran solution under stirring. The solution was stirred for 24 h at room temperature. The carboxydextran was then isolated by precipitation in acetone and subsequently washed with acetone. The product was dried under vacuum. Yield: 5.8g, 96%. ¹H NMR (D₂O): δ 3.26-4.18 (m, dextran glucosidic protons), 4.52-4.92 (m, dextran anomeric proton), 5.05-5.10 (s, carboxylic acid protons).

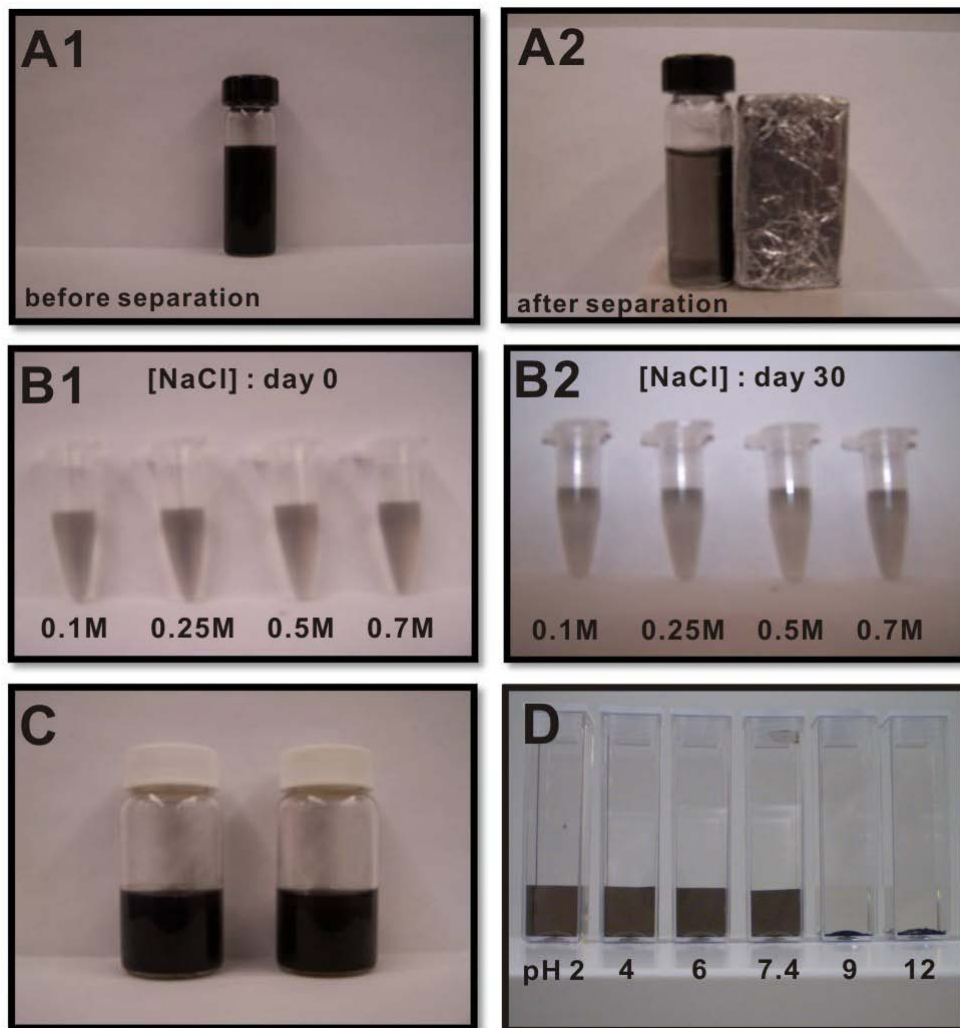


Figure IV-10. Photographs of colloidal solutions of 11nm FeCo/C NPs (A1, A2): Separation of dextran-coated FeCo/C NPs from a suspension in HNO_3 (53 wt%) by a commercial neodymium magnet. **(B1, B2):** Colloidal stability of dextran-coated FeCo/C in NaCl solution from day0 (B1) to day30 (B2). **(C):** Dispersion of carboxy dextran-coated FeCo/C NPs in water. **(D):** pH stability of dextran-coated FeCo/C from pH2 to pH12 in different buffer systems; pH 2 (phosphate buffer), pH4 (benzoate buffer), pH6 (MES buffer), pH7.4 (phosphate buffer), pH9 (Tris buffer), pH12 (phosphate buffer)

4. Target-specific hyperthermia-based cancer therapy

Having demonstrated the potential of our FeCo/C NPs as multimodal imaging probes, we then focused on evaluating their ability to be used as targeted hyperthermia agents for tumor therapy *in vitro*. We hypothesized that our FeCo/C NP would be more efficient hyperthermia agents than Fe₃O₄ NPs of similar size due to their high magnetization and hence, would be more effective in inhibiting the proliferation and inducing apoptosis of target brain tumor cell^{30,37}. To test their efficacy as targeted hyperthermia agents, we first measured the minimum time required to attain the therapeutic temperature (~43 °C) when placed in a homogeneous magnetic field. The specific absorption rate (SAR) of FeCo/C NPs, as derived from the plots of temperature versus time in aqueous solutions under a 334 kHz magnetic field (which is the optimum frequency range estimated by the Neel and Brownian relaxation time simulations³⁸), indicated that the time required for our FeCo/C NPs to reach the therapeutic temperature was ten times shorter than that of Fe₃O₄ NPs (Figure 11A). We next evaluated the concentration-dependent cytotoxicity of our FeCo/C NPs by serial dilution investigations (Figure 12B). From this study, the range of concentrations inducing negligible cytotoxic effects on cells was identified and the concentrations within this range were used for our subsequent experiments. We then sought to precisely increase the temperature of tumor cells thereby minimizing the exposure of other cells to hyperthermic temperatures. For this purpose, FeCo/C NPs functionalized with cyclic-RGD or EGFR antibodies were incubated in co-cultures of glioblastoma cells (U87-EGFP), which had been genetically labelled with enhanced green fluorescent protein (EGFP) and present EGFRs on their surface, and several other less-tumorigenic cells such as PC-12 and astrocytes which tend to have low

expression levels of integrins and EGFR. Our data indicates that the surface-modification of our FeCo/C NPs with cRGD or EGFR antibodies resulted in their selective cellular uptake by the target bTCs, as compared to PC-12 (Figure 11) or astrocytes (Figure 14). Following intracellular uptake of the aforementioned NP constructs, the cells were exposed to AC magnetic field for 15 min. Significant inhibition of proliferation and hyperthermia induced-cell death was observed mainly in the U87 cells while the less-tumorigenic PC-12 cells largely continued proliferating with time (Figure 11B and 11C). Furthermore, Annexin V assays for detection of early apoptosis proved that the cell death was caused by localized heat-induced apoptosis rather than necrosis (Figure 15). We also compared the performance of our FeCo/C NPs with 11 nm Fe₃O₄ NPs under the same experimental conditions and found that the FeCo/C NP-internalized U87-EGFP cells showed a higher percentage of cell death after 24 hours as compared to the Fe₃O₄ NP-internalized ones (Figure 13).

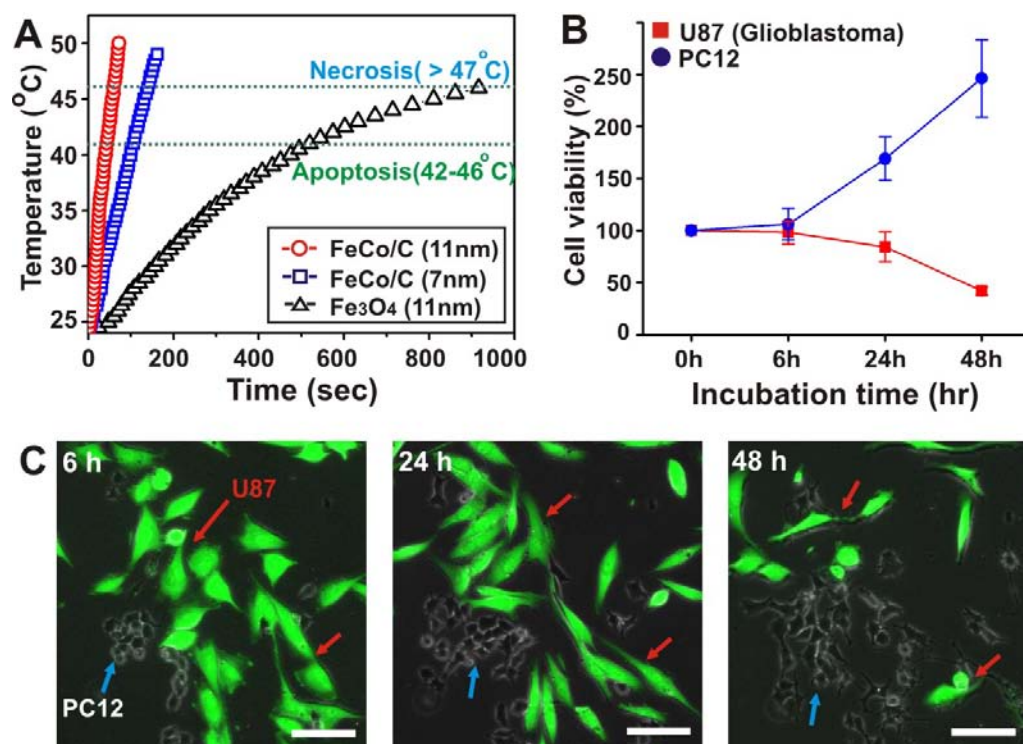


Figure IV-11. *In vitro* hyperthermia studies of the FeCo/C NPs. (A) Plot of temperature versus time for 7 nm FeCo/C, 11 nm FeCo/C and 11 nm Fe₃O₄ NPs showing their relative heat-induction abilities. The heat generated is much higher for FeCo/C NPs than conventional Fe₃O₄ NPs at a given nanoparticle concentration (Figure 11A). It also shows the size-dependent heating effects confirming that 11 nm FeCo/C NPs are better than 7 nm ones for hyperthermia. (B) and (C) U87-EGFP cell death induced by hyperthermia in co-cultures of the highly tumorigenic U87-EGFP cells (marked by red arrows) and the less tumorigenic PC-12 cells (marked by blue arrows) via the targeted delivery of FeCo/C NPs to the U87 cells. Quantitative analysis (B) and fluorescence images (C) show that significant hyperthermia-induced cell death is observed in U87 cells while the PC-12 cells keep proliferating with time. (The number of cells at 0 hrs was taken to be 100% and the other time points were normalized to this value. Scale bar in all images is 100 μm). Copyright Wiley-VCH Verlag GmbH & Co. KGaA. Reproduced with the permission of Ref. 47

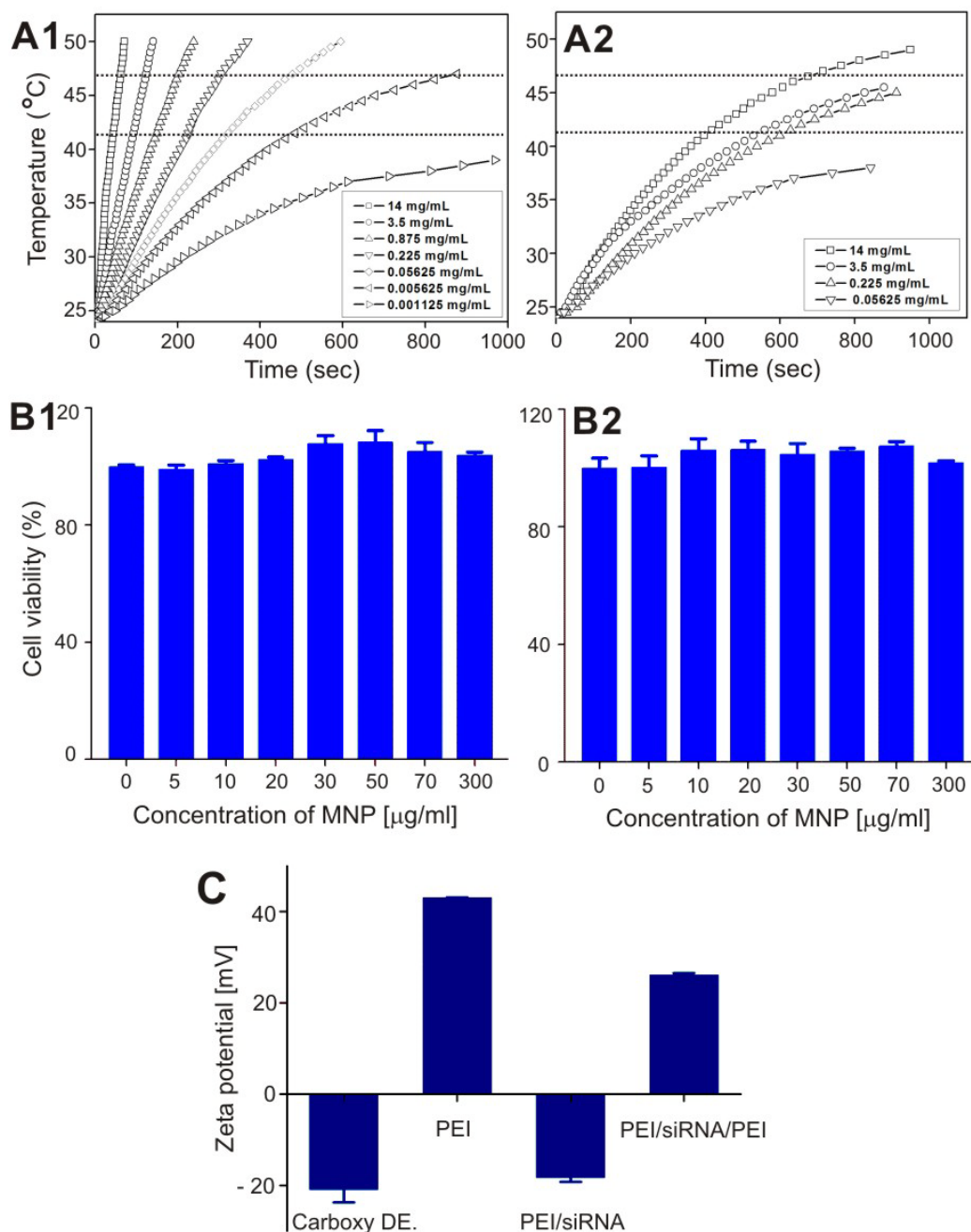


Figure IV-12. Characterization for *In vitro* hyperthermia studies and siRNA delivery using the FeCo/C NPs. (A): Plots of increase in temperature *versus* time for suspensions with different concentrations of (A1), 11 nm FeCo/C NPs and (A2), 11 nm Fe₃O₄ NPs under the 334 kHz magnetic field. **(B):** Toxicity assay using MTS for various concentrations of 11 nm FeCo/C NPs in (B1), U87-EGFP and (B2), U87-EGFRvIII cell lines. **(C):** Zeta potential measurements of various forms of FeCo/C NPs including PEI-siRNA-PEI-FeCo/C NPs to ensure appropriate layer-by-layer coating.

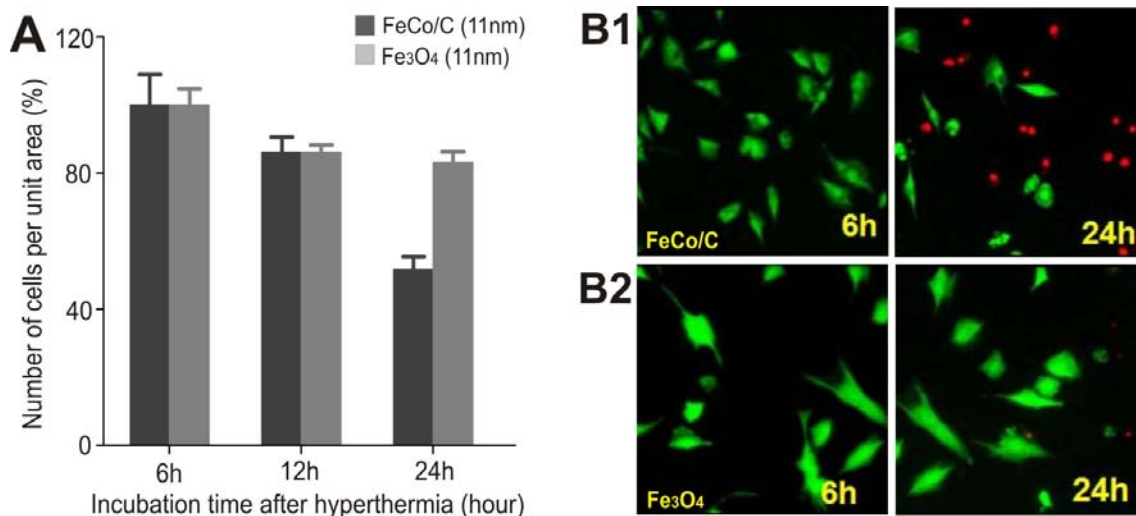


Figure IV-13. U87-EGFP cell death induced by hyperthermia using FeCo/C and Fe₃O₄ nanocrystals. (A): MTS assay showing the effects of hyperthermia induced by FeCo/C and Fe₃O₄ MNPs. **(B):** Dex-NH₂ coated FeCo/C NPs and Fe₃O₄ NPs were used for transfection into U87-EGFP cell line at a concentration of 30 µg/mL. The cell morphology and population were monitored at 6h and 24h after hyperthermia for 15 min. PI staining was performed 30 min before taking images at 24h. The populations of dead and live cells were quantified using the red (PI) and green (EGFP) fluorescence using a fluorescence microscope. **(B1)** Dex-NH₂ coated FeCo/C NPs **(B2)** Fe₃O₄ NPs

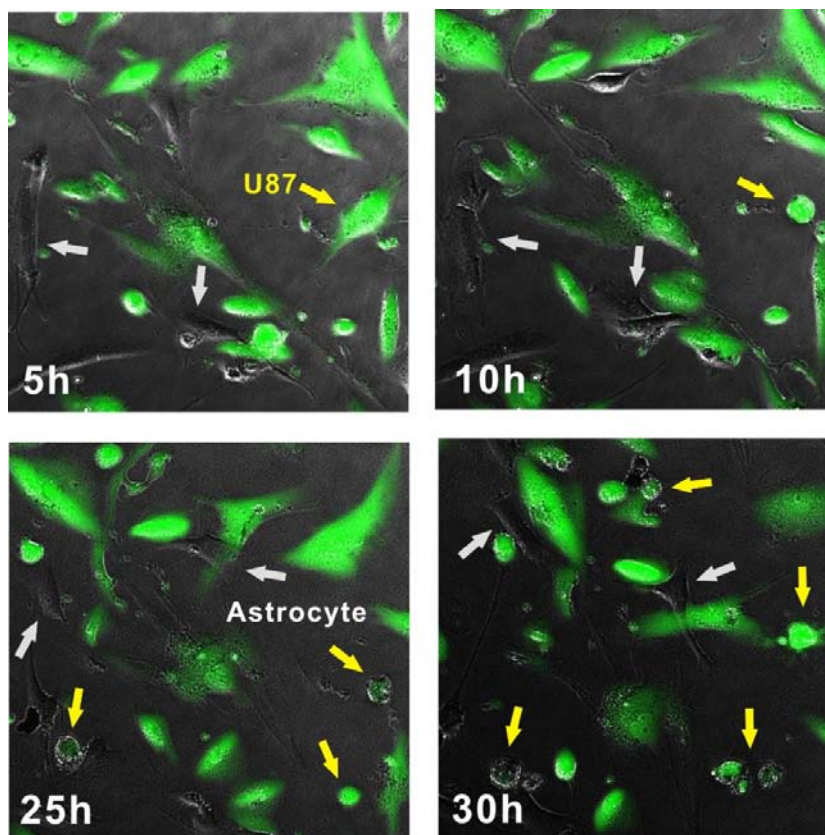


Figure IV-14. Targeted hyperthermia using FeCo/C NPs in co-cultures of U87-EGFP and astrocytes. U87-EGFP cells were co-cultured with astrocytes and 11 nm FeCo/C NPs with EGFR antibody were selectively delivered to U87-EGFP at a nanoparticle concentration of 10 $\mu\text{g/mL}$. After 15 minutes of hyperthermia treatment, cells were monitored to check the hyperthermia effect up to 30 h. Images show that U87-EGFP cells are in the process of apoptosis but the astrocytes are still viable.

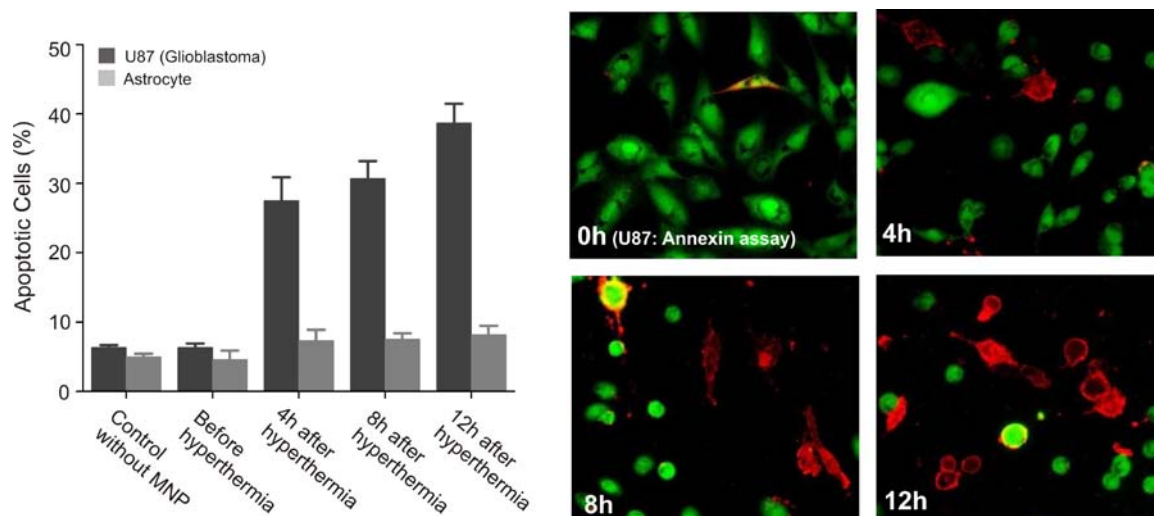


Figure IV-15. Annexin-V assay for quantification of apoptotic cells in co-cultures of U87-EGFP cells and astrocytes. Apoptotic cells are quantified with annexin-V assay after treatment with 30 $\mu\text{g/mL}$ EGFR-conjugated FeCo/C NPs and subsequent hyperthermia at 334 kHz for 15 min. Astrocytes are not damaged by the FeCo/C, however 40% of U87-EGFP cells are in an early apoptotic process 12 hours after hyperthermia.

5. A combined therapy via siRNA and hyperthermia for synergistic silencing of the PI3K/AKT signaling pathway in bTCs

In the past decade, there has been a considerable interest in the development of nanoparticle based biomolecule carriers for simultaneous imaging, diagnostic and therapeutic purposes. RNA interference (RNAi), wherein small double-stranded RNA (siRNAs) can inhibit the expression of specific proteins by suppressing a target gene selectively at the post-transcriptional mRNA level, is one of the most promising therapeutic approaches for treating malignant cancers.³⁹⁻⁴¹ In combination with other chemotherapeutic methods like hyperthermia, RNAi could prove to be a powerful tool to manipulate the tumor microenvironment. In order to assess the capability of FeCo/C NPs to selectively deliver siRNA and knockdown the target gene, we examined the suppression of EGFP in U87-EGFP cells. EGFP reporter systems have been widely used by many groups for evaluating the knockdown efficiency and RNAi activity, since the endogenous expression level of EGFP is not closely related to the cell viability. The concentration-dependent cytotoxicity of our FeCo/C NPs was measured by serial dilution investigations.⁴²⁻⁴⁵ (Figure 12B) From this study, the range of concentrations inducing negligible cytotoxic effects on cells was identified and the concentrations within this range were used for our subsequent experiments. The decrease in green fluorescence intensity due to siRNA-mediated knockdown of EGFP was monitored to quantify the knockdown efficiency (~ 80 %, data of statistical analysis not shown) of our siRNA-NP constructs (Figure 16A2 and 16B2). Once the conditions for the siRNA delivery and knockdown were optimized, we focused on inhibiting the proliferation and inducing apoptosis of U87-EGFRvIII cell lines overexpressing the oncogenic EGFRvIII gene. EGFRvIII is a

mutant type of the epidermal growth factor receptor (EGFR) as well as an oncogenic receptor that is highly expressed only in tumor cells, and not in normal cells. We hypothesized that the knockdown of the target oncogene, EGFRvIII, with our siRNA-FeCo/C NP constructs would sensitize the cells towards a hyperthermia-based therapy, thereby leading to a synergistic inhibition of tumor cell proliferation and increase in cell death. The U87-EGFRvIII cells were incubated with our FeCo/C NPs modified with siRNA against EGFRvIII, followed by hyperthermia treatment for 5 minutes at 72, 96 and 120 hrs post siRNA-treatment. The effect of the knockdown of the EGFRvIII oncogene was imaged using a microscope at various time intervals (Figure 16B1 and 6B2). Quantitative analysis based upon MTS assay (Figure 6B3) showed that treatment of cells with our siRNA-MNPs against EGFRvIII followed by hyperthermia, induced significantly more cell death, as compared to the controls. This could be attributed to the fact that silencing of the EGFRvIII oncogene results in a decrease in expression of the focal adhesion proteins which makes the cells more susceptible to heat, thereby leading to a synergistic increase in cell death⁴⁶. Our study clearly demonstrates that the appropriate combination of various therapeutic modalities using our FeCo/C NPs can significantly enhance the therapeutic efficacy relative to the individual components.

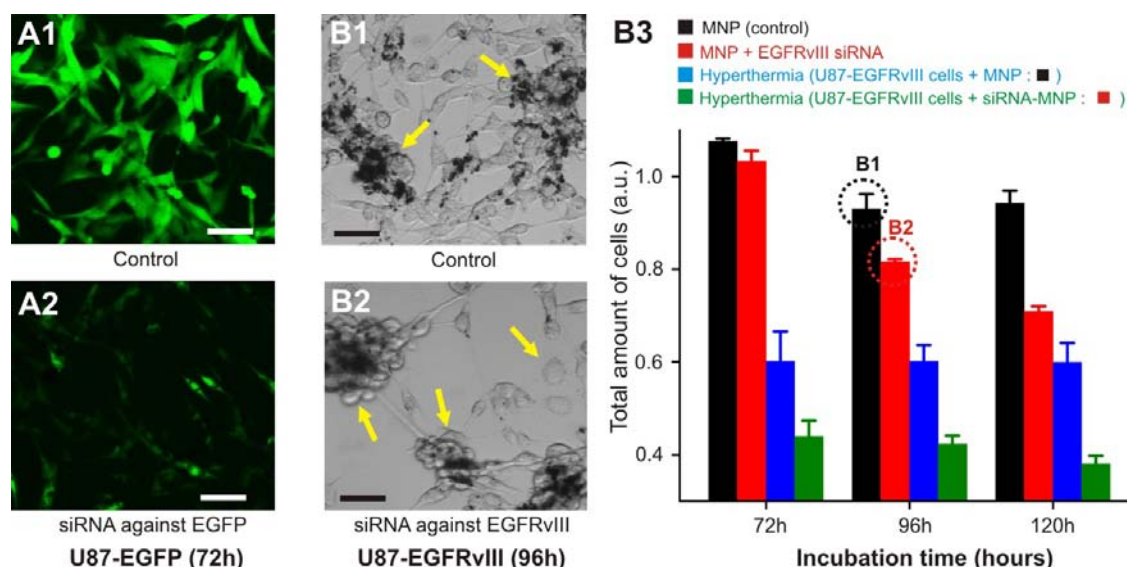


Figure IV-16. siRNA-mediated knockdown and hyperthermia using siRNA-FeCo/C constructs in U87 cells. **a,b,** Delivery of siRNA against EGFP in U87-EGFP cells. The knockdown was monitored using fluorescence imaging. The fluorescence in cells transfected with the siRNA-FeCo/C NPs was significantly reduced 72 h post-transfection (**A1**) as compared to the control cells without siRNA (**A2**). (**B1, B2**): Knockdown of the EGFRvIII oncogene in U87-EGFRvIII cells using FeCo/C-siRNA constructs. Cells treated with the siRNA-constructs show significant cell death after 96 h (**B1**) as compared to the controls (**B2**) due to the knockdown of the EGFRvIII gene. The populations of dead cells are marked by yellow arrows. (**B3**): MTS assay demonstrating the synergistic inhibition of proliferation and induction of cell death by the combined siRNA and hyperthermia treatment using siRNA-FeCo/C MNPs in U87-EGFRvIII cells as compared to individual treatments and non-treated controls (Scale bar in all images is 100 μ m). Copyright Wiley-VCH Verlag GmbH & Co. KGaA. Reproduced with the permission of Ref. 47

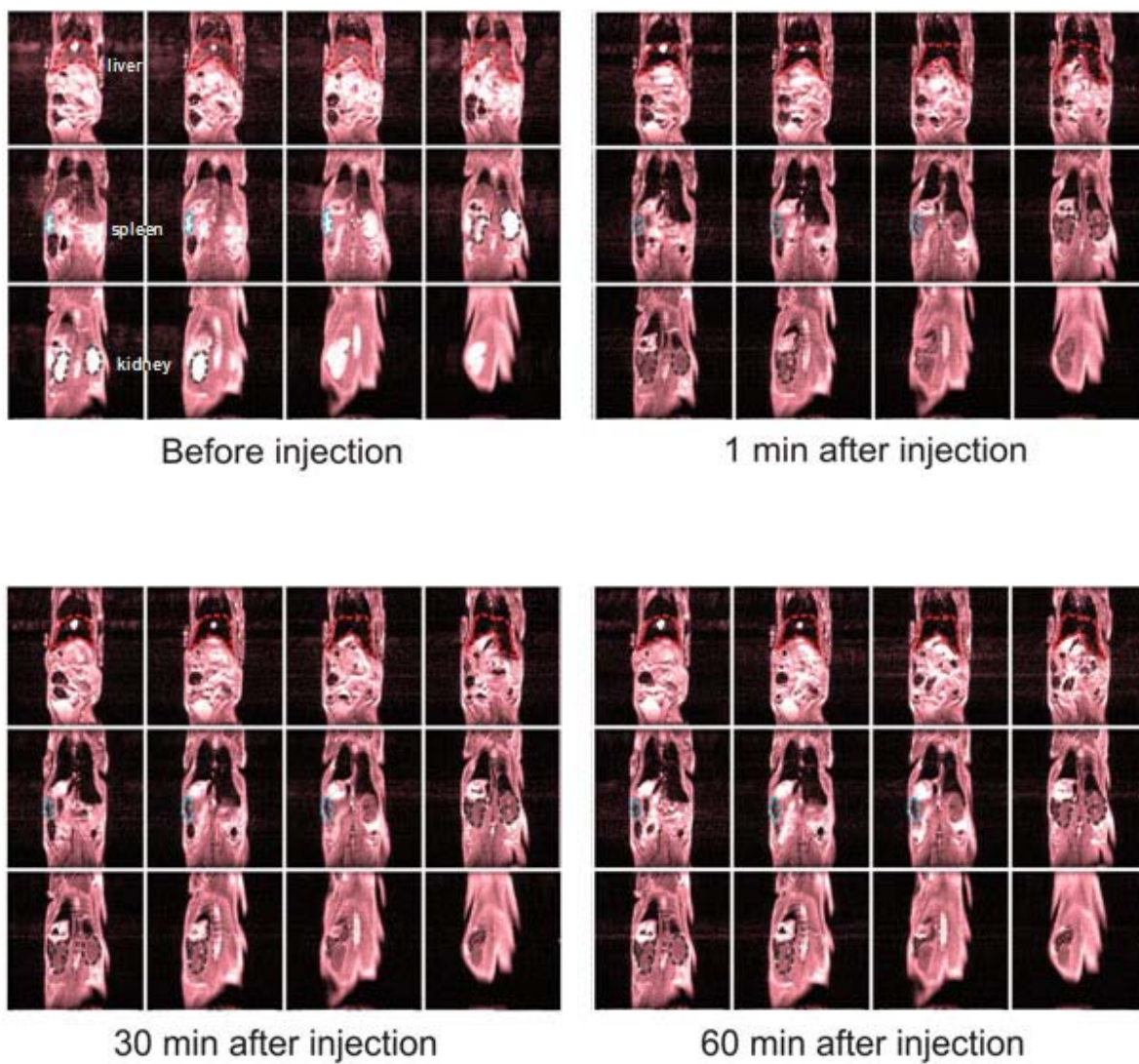
D. Conclusion

In summary, this work provides an early demonstration of integrating molecular imaging with a targeted hyperthermia-based therapy in malignant brain tumor cells using highly efficient FeCo/C NPs with high selectivity. Our FeCo/C NPs have successfully been demonstrated to have a well-defined correlation and a fast and sensitive thermal response to the strength of applied magnetic field. At the same time, our FeCo/C NPs could be developed as novel therapeutic and diagnostic tools for brain cancer research. The ability to functionalize the graphitic surface of the MNPs with targeting ligands and drug molecules would be critical to realize the potential of nanoparticle-based diagnosis, and therapy of cancers. It should be noted that our FeCo/C NPs showed excellent MRI contrast results, compared to the conventional MRI contrast agents as well as enabled us to collect the Raman spectral information at the single cell level. More importantly, the use of our FeCo/C NPs for site-specific and localized hyperthermia would greatly complement and enhance the effects of other therapeutic modalities including gene therapy and chemotherapy, thereby reducing the dose of anticancer drugs, mitigating their toxic side-effects and effectively circumventing drug-resistance in cancers.

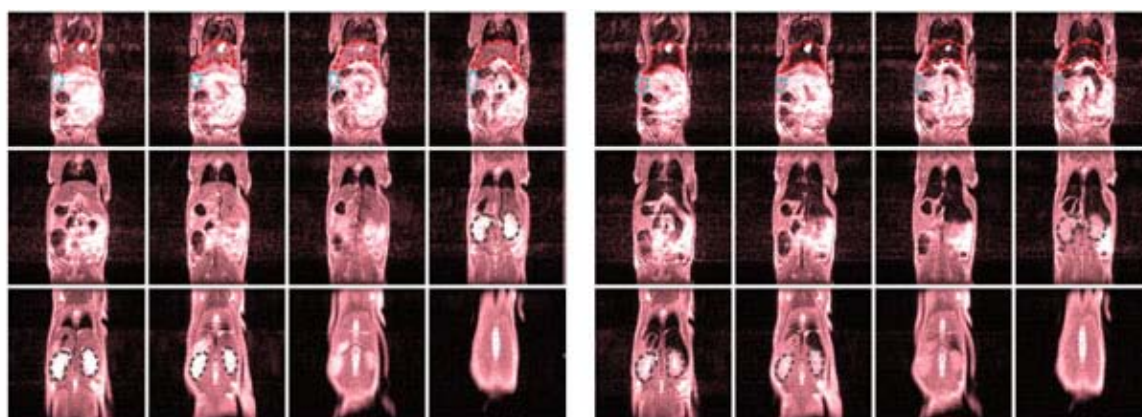
E. Appendix

- 1. T₂-weighted images of the rat's body after injection of carboxy dextran-coated FeCo/C NPs at a concentration of 0.25 mg Fe/kg**
- 2. T₂-weighted images of the rat's body after injection of Resovist at a concentration of 2.5 mg Fe/kg**
- 3. NMR spectra of dextran functionalized with 4-nitrophenyl chloroformate groups (4-NC dextran) (2)**
- 4. NMR spectra of dextran functionalized with amine groups (3)**
- 5. NMR spectra of dextran functionalized with carboxyl groups (4)**

1. T₂-weighted images of the rat's body after injection of carboxy dextran-coated FeCo/C NPs at a concentration of 0.25 mg Fe/kg

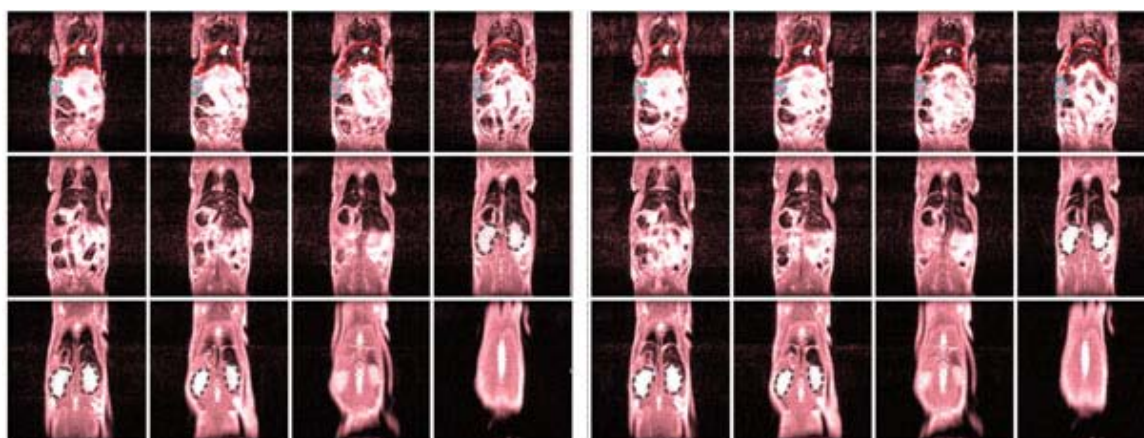


2. T₂-weighted images of the rat's body after injection of Resovist at a concentration of 2.5 mg Fe/kg



Before injection

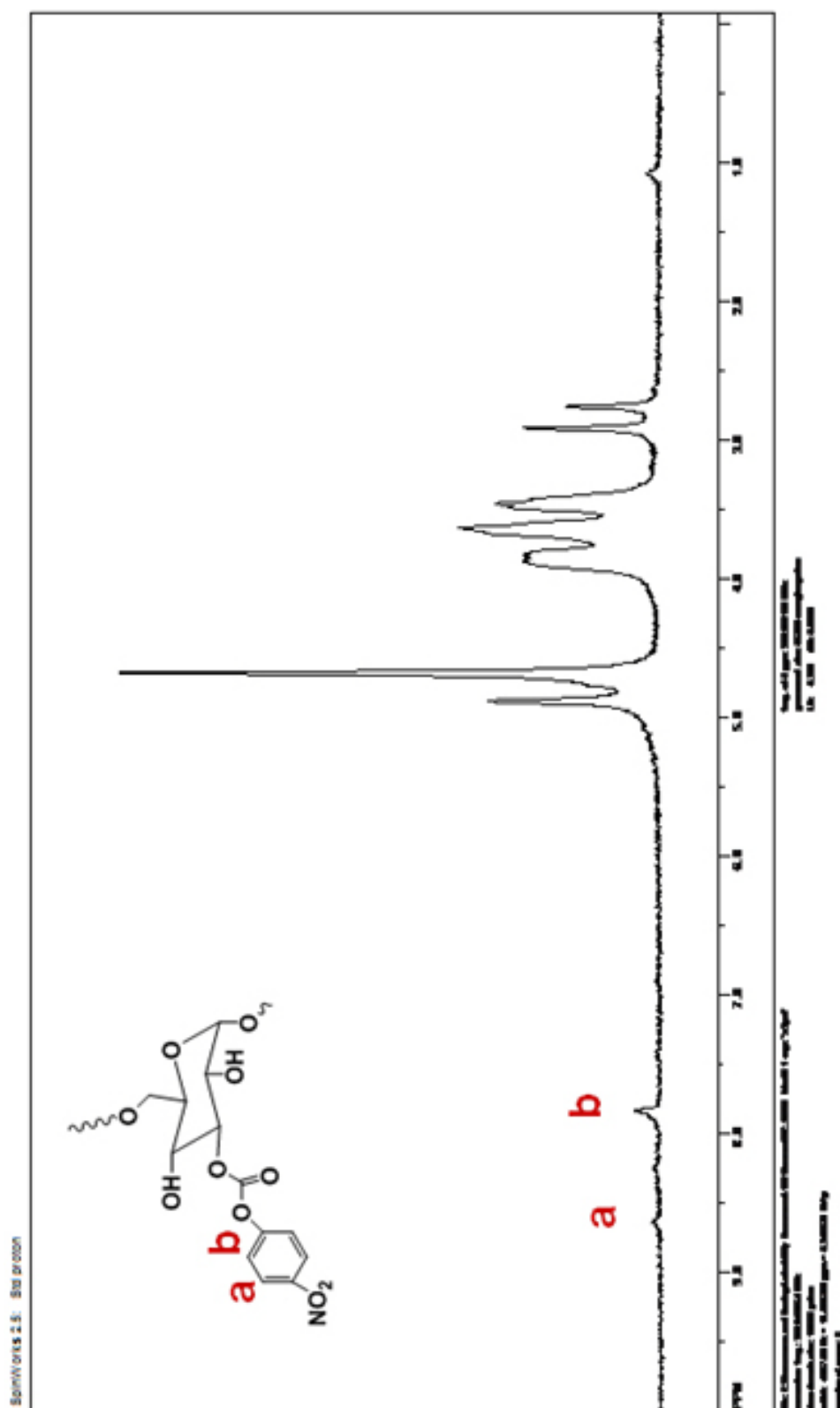
1 min after injection



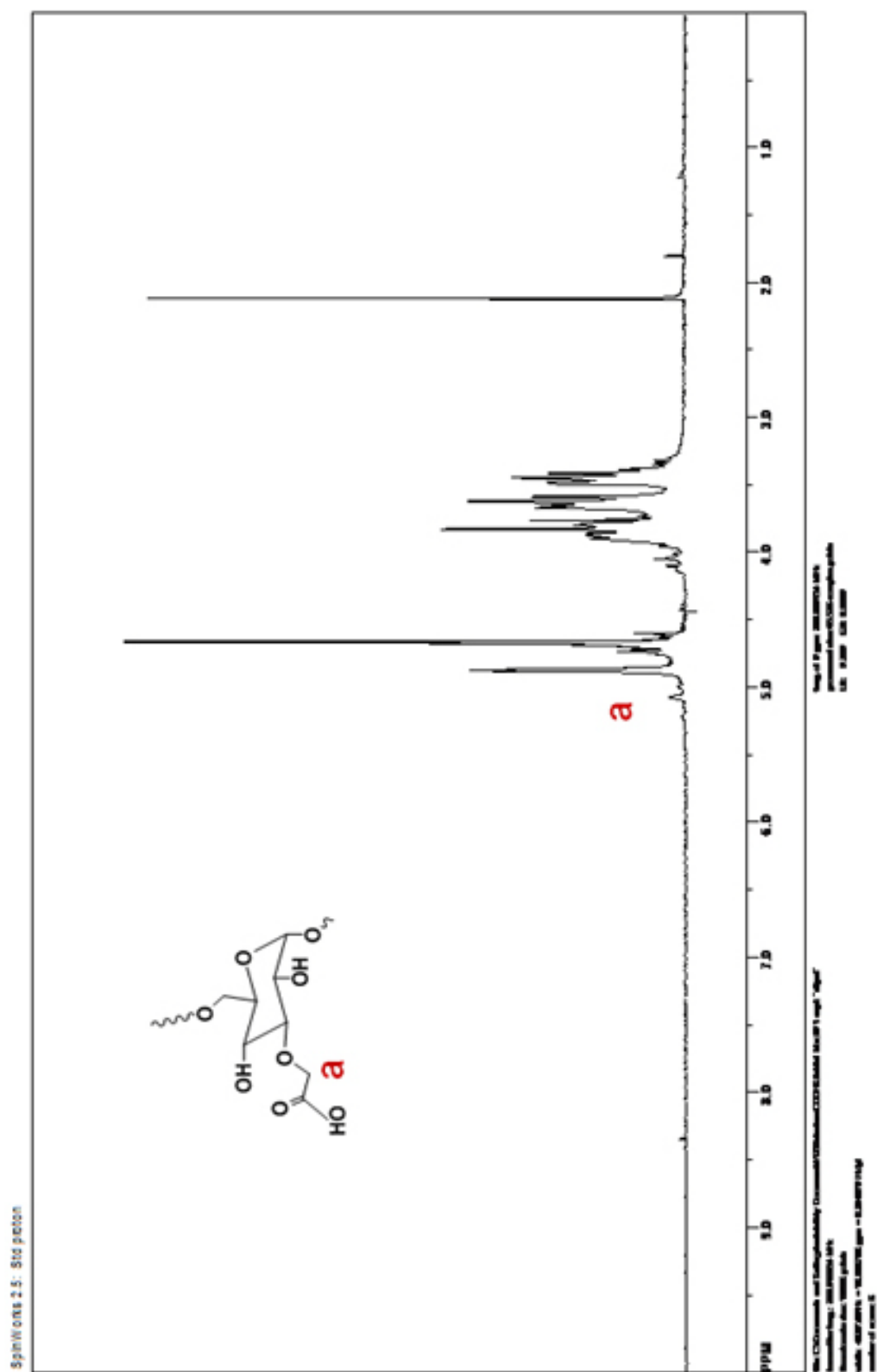
30 min after injection

60 min after injection

3. NMR spectra of dextran functionalized with 4-nitrophenyl chloroformate groups (4-NC dextran) (2)



5. NMR spectra of dextran functionalized with carboxyl groups (4)



F. References

- 1 Bulte, J. W. M. *et al.* Magnetodendrimers allow endosomal magnetic labeling and in vivo tracking of stem cells. *Nature Biotechnology* **19**, 1141-1147 (2001).
- 2 Lu, A. H., Salabas, E. L. & Schuth, F. Magnetic nanoparticles: Synthesis, protection, functionalization, and application. *Angewandte Chemie-International Edition* **46**, 1222-1244, doi:10.1002/anie.200602866 (2007).
- 3 Zeng, H. & Sun, S. H. Syntheses, properties and potential applications of multicomponent magnetic nanoparticles. *Advanced Functional Materials* **18**, 391-400, doi:10.1002/adfm.200701211 (2008).
- 4 Kim, J. *et al.* Designed fabrication of a multifunctional polymer nanomedical platform for simultaneous cancer-targeted imaging and magnetically guided drug delivery. *Advanced Materials* **20**, 478-+, doi:10.1002/adma.200701726 (2008).
- 5 Lin, W. B., Hyeon, T., Lanza, G. M., Zhang, M. Q. & Meade, T. J. Magnetic Nanoparticles for Early Detection of Cancer by Magnetic Resonance Imaging. *MRS Bulletin* **34**, 441-448 (2009).
- 6 Hogemann, D., Ntziachristos, V., Josephson, L. & Weissleder, R. High throughput magnetic resonance imaging for evaluating targeted nanoparticle probes. *Bioconjugate Chemistry* **13**, 116-121, doi:10.1021/bc015549h (2002).
- 7 Mannix, R. J. *et al.* Nanomagnetic actuation of receptor-mediated signal transduction. *Nature Nanotechnology* **3**, 36-40, doi:10.1038/nnano.2007.418 (2008).
- 8 Cherukuri, P., Glazer, E. S. & Curleya, S. A. Targeted hyperthermia using metal nanoparticles. *Advanced Drug Delivery Reviews* **62**, 339-345, doi:10.1016/j.addr.2009.11.006 (2010).
- 9 Huilgol, N. G., Gupta, D. & Dixit, R. Chemoradiation with hyperthermia in the treatment of head and neck cancer. *International Journal of Hyperthermia* **26**, 21-25, doi:10.3109/02656730903418283 (2010).
- 10 Prasad, N. K., Rathinasamy, K., Panda, D. & Bahadur, D. Mechanism of cell death induced by magnetic hyperthermia with nanoparticles of gamma-MnxFe2-xO3 synthesized by a single step process. *Journal of Materials Chemistry* **17**, 5042-5051, doi:10.1039/b708156a (2007).

- 11 Ito, A., Matsuoka, F., Honda, H. & Kobayashi, T. Heat shock protein 70 gene therapy combined with hyperthermia using magnetic nanoparticles. *Cancer Gene Therapy* **10**, 918-925, doi:10.1038/sj.cgt.7700648 (2003).
- 12 Huber, D. L. Synthesis, properties, and applications of iron nanoparticles. *Small* **1**, 482-501, doi:10.1002/sml.200500006 (2005).
- 13 Lee, H. *et al.* Thermally cross-linked superparamagnetic iron oxide nanoparticles: Synthesis and application as a dual Imaging probe for cancer in vivo. *Journal of the American Chemical Society* **129**, 12739-12745, doi:10.1021/ja072210i (2007).
- 14 Chaubey, G. S. *et al.* Synthesis and stabilization of FeCo nanoparticles. *Journal of the American Chemical Society* **129**, 7214-+, doi:10.1021/ja0708969 (2007).
- 15 Sun, S. H., Murray, C. B., Weller, D., Folks, L. & Moser, A. Monodisperse FePt nanoparticles and ferromagnetic FePt nanocrystal superlattices. *Science* **287**, 1989-1992 (2000).
- 16 Bystrzejewski, M. *et al.* Large scale continuous synthesis of carbon-encapsulated magnetic nanoparticles. *Nanotechnology* **18**, doi:145608 10.1088/0957-4484/18/14/145608 (2007).
- 17 Mahmood, M. *et al.* Graphitic Materials for RF Thermal Ablation of Tumors. *IEEE Transactions on Industry Applications* **45**, 2162-2169, doi:10.1109/tia.2009.2031918 (2009).
- 18 Hyeon, T., Lee, S. S., Park, J., Chung, Y. & Bin Na, H. Synthesis of highly crystalline and monodisperse maghemite nanocrystallites without a size-selection process. *Journal of the American Chemical Society* **123**, 12798-12801, doi:10.1021/ja016812s (2001).
- 19 Park, J. *et al.* Ultra-large-scale syntheses of monodisperse nanocrystals. *Nature Materials* **3**, 891-895, doi:10.1038/nmat1251 (2004).
- 20 Seo, W. S. *et al.* FeCo/graphitic-shell nanocrystals as advanced magnetic-resonance-imaging and near-infrared agents. *Nature Materials* **5**, 971-976, doi:10.1038/nmat1775 (2006).
- 21 Xu, C. J. & Sun, S. H. Superparamagnetic nanoparticles as targeted probes for diagnostic and therapeutic applications. *Dalton Transactions*, 5583-5591, doi:10.1039/b900272n (2009).
- 22 Wei, X. W. *et al.* Large-Scale Controlled Synthesis of FeCo Nanocubes and Microcages by Wet Chemistry. *Chemistry of Materials* **20**, 6248-6253, doi:10.1021/cm800518x (2008).

- 23 Seo, W. S., Kim, S. M., Kim, Y. M., Sun, X. & Dai, H. J. Synthesis of Ultrasmall Ferromagnetic Face-Centered Tetragonal FePt-Graphite Core-Shell Nanocrystals. *Small* **4**, 1968-1971, doi:10.1002/smll.200800257 (2008).
- 24 Solanki, A., Kim, J. D. & Lee, K. B. Nanotechnology for regenerative medicine: nanomaterials for stem cell imaging. *Nanomedicine* **3**, 567-578, doi:10.2217/17435889.3.4.567 (2008).
- 25 Yamada, M. *et al.* Manganese-Guided Cellular MRI of Human Embryonic Stem Cell and Human Bone Marrow Stromal Cell Viability. *Magnetic Resonance in Medicine* **62**, 1047-1054, doi:10.1002/mrm.22071 (2009).
- 26 Lee, H. *et al.* Antibiofouling polymer-coated superparamagnetic iron oxide nanoparticles as potential magnetic resonance contrast agents for in vivo cancer imaging. *Journal of the American Chemical Society* **128**, 7383-7389, doi:10.1021/ja061529k (2006).
- 27 Wang, C. G. & Irudayaraj, J. Multifunctional Magnetic-Optical Nanoparticle Probes for Simultaneous Detection, Separation, and Thermal Ablation of Multiple Pathogens. *Small* **6**, 283-289, doi:10.1002/smll.200901596 (2010).
- 28 Qian, X. M. *et al.* In vivo tumor targeting and spectroscopic detection with surface-enhanced Raman nanoparticle tags. *Nature Biotechnology* **26**, 83-90, doi:10.1038/nbt.1377 (2008).
- 29 Haka, A. S. *et al.* Identifying microcalcifications in benign and malignant breast lesions by probing differences in their chemical composition using Raman spectroscopy. *Cancer Research* **62**, 5375-5380 (2002).
- 30 Wang, L. Y., Bai, J. W., Li, Y. J. & Huang, Y. Multifunctional nanoparticles displaying magnetization and near-IR absorption. *Angewandte Chemie-International Edition* **47**, 2439-2442, doi:10.1002/anie.200800014 (2008).
- 31 Berry, C. C., Wells, S., Charles, S., Aitchison, G. & Curtis, A. S. G. Cell response to dextran-derivatised iron oxide nanoparticles post internalisation. *Biomaterials* **25**, 5405-5413, doi:10.1016/j.biomaterials.2003.12.046 (2004).
- 32 Zhang, Y., Kohler, N. & Zhang, M. Q. Surface modification of superparamagnetic magnetite nanoparticles and their intracellular uptake. *Biomaterials* **23**, 1553-1561 (2002).
- 33 Hifumi, H. *et al.* Dextran Coated Gadolinium Phosphate Nanoparticles for Magnetic Resonance Tumor Imaging. *Journal of Materials Chemistry* **19**, 6393-6399, doi:10.1039/b902134e (2009).

- 34 Xie, J. *et al.* Ultrasmall c(RGDyK)-coated Fe₃O₄ nanoparticles and their specific targeting to integrin $\alpha(v)\beta(3)$ -rich tumor cells. *Journal of the American Chemical Society* **130**, 7542-+, doi:10.1021/ja802003h (2008).
- 35 Ramirez, J. C., Sanchezchaves, M. & Arranz, F. Dextran Functionalized by 4-nitrophenyl carbonate groups-Aminolysis Reactions. *Angewandte Makromolekulare Chemie* **225**, 123-130 (1995).
- 36 Lee, S. & Perez-Luna, V. H. Dextran-gold nanoparticle hybrid material for biomolecule immobilization and detection. *Analytical Chemistry* **77**, 7204-7211, doi:10.1021/ac050484n (2005).
- 37 Yang, W. L. *et al.* Convection-enhanced delivery of boronated epidermal growth factor for molecular targeting of EGF receptor-positive gliomas. *Cancer Research* **62**, 6552-6558 (2002).
- 38 Mornet, S., Vasseur, S., Grasset, F. & Duguet, E. Magnetic nanoparticle design for medical diagnosis and therapy. *Journal of Material Chemistry* **14**, 2161-2175 (2004).
- 39 Gan, H. K., Kaye, A. H. & Luwor, R. B. The EGFRvIII variant in glioblastoma multiforme. *Journal of Clinical Neuroscience* **16**, 748-754, doi:DOI 10.1016/j.jocn.2008.12.005 (2009).
- 40 Elbakry, A. *et al.* Layer-by-Layer Assembled Gold Nanoparticles for siRNA Delivery. *Nano Letters* **9**, 2059-2064, doi:10.1021/nl9003865 (2009).
- 41 Heimberger, A. B., Suki, D., Yang, D., Shi, W. M. & Aldape, K. The natural history of EGFR and EGFRvIII in glioblastoma patients. *Journal of Translational Medicine* **3**, doi:3810.1186/1479-5876-3-38 (2005).
- 42 Jung, J. J. *et al.* Selective Inhibition of Human Brain Tumor Cells through Multifunctional Quantum-Dot-Based siRNA Delivery. *Angewandte Chemie-International Edition* **49**, 103-107, doi:10.1002/anie.200905126 (2010).
- 43 Kuan, C. T., Wikstrand, C. J. & Bigner, D. D. EGF mutant receptor vIII as a molecular target in cancer therapy. *Endocrine-Related Cancer* **8**, 83-96 (2001).
- 44 Lee, K. B., Lim, J. H. & Mirkin, C. A. Protein nanostructures formed via direct-write dip-pen nanolithography. *Journal of the American Chemical Society* **125**, 5588-5589, doi:10.1021/ja034236p (2003).
- 45 Lee, K. B., Park, S. J., Mirkin, C. A., Smith, J. C. & Mrksich, M. Protein nanoarrays generated by dip-pen nanolithography. *Science* **295**, 1702-1705 (2002).

- 46 Yuan, T. L. & Cantley, L. C. PI3K pathway alterations in cancer: variations on a theme. *Oncogene* **27**, 5497-5510, doi:10.1038/onc.2008.245 (2008).
- 47 Park, J. K., Jung, J. & Lee, K.-B. Targeted multifunctional magnetic nanoparticles for synergistic siRNA delivery and hyperthermia for brain tumor cells. *Angewandte Chemie-International Edition* in revision

CHAPTER V

CONCLUSIONS AND PERSPECTIVES

Nanoscience is a burgeoning field with promising methodologies to overcome the limits of conventional scientific approaches. It is a multidisciplinary field that has led to the development of new instrumentalities and nanostructures. Especially, nanobiotechnology and nanomedicine are leading to significant improvements in biotechnology and cell biology.

The RNA interference(RNAi)-based approach is one of the most promising new chemotherapeutic strategies. Various nanomaterials such as quantum dots(QDs), iron oxide NPs, gold NPs, and polymer NPs have been used for efficiently delivering siRNA into tumor cells. However, most of them focused on just the enhancement of transfection efficiency and the knockdown of non-oncogenes such as EGFP. The study in chapter III demonstrated target-oriented delivery of siRNA, monitoring of colocalization of siRNA, and knockdown of the key oncogene EGFRvIII for inducing apoptosis of malignant brain cancer cells all together in one multimodal QD system.

Target-specific QDs were designed as a siRNA delivery vehicle and imaging probe. High quality CdSe/CdS/ZnS core-shell QDs were prepared via thermal decomposition and SILAR(successive ionic layer adsorption and reaction) methods. In order to make them water-soluble and biocompatible, surface ligands were replaced by DHLA-PEG-NH₂ (dihydrolipoic acid-polyethylene glycol), mercaptoacetic acid (MAA), mercaptosuccinic acid(MSA)-streptavidin, etc. For the conjugation of biomolecules, biofunctional linkers were synthesized to link them via both covalent bond for tracking and disulfide bond for the delivery. siRNA for gene-silencing and RGD/TAT peptide for targeted delivery were successfully attached to the surface of QDs in a controlled manner for numbers and ratio of each species.

siRNA delivered by target-specific QDs succeeded in knock-down of EGFRvIII that led to the apoptosis of brain cancer cells. First, as a proof-of-concept, siRNA against EGFP was transfected into U87-EGFP cells by this system simply to ascertain the efficiency of gene knock-down and its correlation with the co-localization of QDs. In addition, target-specific delivery was also demonstrated by showing that the majority of QDs were located in U87 cells among co-cultured control cells which have much less amount of target receptors for RGD peptide. In order to test them as a prominent multimodal therapeutic platform, these were transfected to U87-EGFRvIII cells which overexpress EGFRvIII, the key oncogene for the up-regulation of the PI3K/AKT signaling pathway which is critical for cancer cell proliferation. The silencing effect of EGFRvIII, inhibition of cell proliferation/induction of cell apoptosis was confirmed by showing the morphological change of apoptotic cells, the decreased population of viable cells, and down-regulation of key signaling proteins in the PI3K pathway.

Magnetic nanomaterials have shown great potential for cancer research as *in vivo* imaging probes as well as multifunctional therapeutic agents. To harness the maximum potential of magnetic nanoparticles(MNPs), it is necessary to synthesize MNPs having excellent magnetic properties for diagnosis and therapy, and to develop novel effective therapeutic methods with multimodal MNPs using the non-invasive radiation of a magnetic field. However, most current studies focused on the synthesis and characterization of MNPs with limited demonstration of biomedical applications. The potential of MNPs is partially explored to highlight limited aspects of its effect. Therefore, there is a clear need to synthesize effective chemotherapeutic MNPs and to develop novel therapeutic strategies combining siRNA/drug delivery and hyperthermia. In this study of

chapter IV, high performance metal alloys MNPs with a graphitic-shell (FeCo/C) were synthesized for targeted delivery of siRNA-MNPs to brain tumor cells in order to investigate the hyperthermic effect after the knock-down of EGFRvIII, expecting the synergistic inhibition of tumor cell proliferation and induction of apoptosis.

7nm and 11nm graphitic carbon-shell protected iron-cobalt(FeCo/C) MNPs were made by a novel synthetic approach which combined a hydrothermal method and annealing at high temperature. The FeCo core shows superior magnetization and the graphite shell protects the core from decomposition by oxidation and other factors. Through the annealing process, the crystallinity was improved a lot, the graphite shell was formed, and the shell thickness was easily controlled. T_2 weighted magnetic resonance(MR) imaging of FeCo/C is much more sensitive than commercially available MNP, Resovist. In addition, the graphite shell is Raman active so it can be used for *in vivo* imaging. For biocompatibility and easy bioconjugation, various functionalized-dextrans were synthesized and coated on the surface of FeCo/C. cRGD and antibody were conjugated for targeting toward brain cancer cells. PEI(polyethylene imine) was also used for the transfection of nucleic acids such as siRNA, plasmid, and antisense DNA.

A combined therapy of siRNA delivery and hyperthermia was performed for brain tumor cells. The high magnetization of FeCo/C results in high hyperthermia capability through both the increased Neel relaxation under the AC magnetic field and the higher SAR(specific absorption rate) value that is a key parameter for hyperthermia, compared to the conventional iron oxide nanoparticles. The hyperthermia study was performed by target-specifically delivering EGFR antibody/cRGD conjugated FeCo/C MNPs to brain cancer cells from the co-cultured control cells, and by generating heat to induce apoptosis

of cancer cells. In order to maximize the therapeutic effect of FeCo/C, siRNA-FeCo/C MNPs were internalized and the PI3K signaling pathway was successfully silenced. As a result, knock-down of EGFRvIII caused cancer cell apoptosis and decreased expression of focal adhesion protein by the signaling crosstalk to the FAK signaling pathway. When hyperthermia is applied to brain cancer cells with down-regulated PI3K/AKT signal by as-delivered siRNA, there is a synergistic effect of cancer cell death by hyperthermia and gene silencing.

The multimodal and multifunctional NP system could be effectively accomplished by coupling biodegradable polymers. Poly(β -amino ester) (PBAE) polymer developed by the Langer group is a good candidate because it has been reported to be biocompatible and utilized for siRNA delivery. In the chapter V, we propose the synthesis of PBAE and dextran to coat FeCo/C for the increase of *in vivo* biocompatibility as commercially available MR contrasting agents are coated with dextran. Moreover, its potential includes conjugation of anticancer drug and formulation with siRNA in one hybrid system. Since Erlotinib, a key anticancer drug, inhibits the function of as-expressed EGFRvIII, and siRNA breaks down mRNA critical for as-preparing EGFRvIII, this system will play an important role of synergistic induction of cancer cell apoptosis. In addition, increased biocompatibility, longer circulation by attaching PEG, and highly sensitive MR imaging by FeCo/C make this system a promising candidate for *in vivo* diagnosis and cancer therapy.

Poly(β -amino ester) (PBAE) dextran polymer-FeCo/C MNP hybrid system was prepared. PBAE-dextran was synthesized to coat FeCo/C MNPs. PBAE has been reported to be biocompatible and biodegradable, and the PBAE polymer moiety can conjugate

different types of molecules for various purposes. Therefore, each repeating unit was utilized in the following ways. First, the anticancer drug, Erlotinib, was conjugated to inhibit the receptor tyrosine kinase, and the hydroxyl group is for the increase of water-solubility. Second, the oligoamine moiety was attached to increase the efficient delivery of siRNA against EGFRvIII, a key receptor tyrosine kinase for the PI3K signaling pathway. Moreover, targeting molecules such as cRGD and EGFR antibody were linked to this moiety. Therefore, this hybrid system allows the synergistic down-regulation of the PI3K signaling pathway with both gene knock-down by siRNA and inhibition of function of as-expressed EGFRvIII by Erlotinib. Moreover, hyperthermia was added for maximum efficacy of brain cancer cell death, and both highly sensitive MR imaging by FeCo/C and conjugation of PEG(polyethylene glycol) are for *in vivo* application for cancer therapy .

Synergistic cancer therapy is being carried out with anticancer drug and siRNA plus hyperthermia by FeCo/C. The efficacy of anticancer drug conjugated to PBAE was compared to the anticancer drug itself. The degradation mechanism in the cell was explored. This hybrid system was delivered target-specifically to brain cancer cells with EGFR antibody or cRGD. When siRNA against EGFRvIII was added, the PI3K/AKT signaling pathway was silenced efficiently. Hyperthermia added to the system will show an improved therapeutic effect for future *in vivo* application.

The PI3K signaling pathway is interconnected with various signaling pathways. EGFRvIII triggering the PI3K/AKT signaling for cell proliferation/apoptosis also affects focal adhesion formation, cancer cell migration, and invasion via FAK signaling pathway, etc. All these effects can help us to understand cancer cell metastasis and be applied to the development of a novel therapeutic strategy. Combining the delivery of siRNA-NPs with

culture of transfected cancer cells on micro-scale structures, a new methodology is proposed in the Appendix to quantify and evaluate the phenotype change of cancer cells via knockdown of the gene, especially for a metastasis study of cancer cells. Micro-contact printed(μ CP) patterns and microfluidic techniques are being used to quantify the phenotype change by knock-down of EGFRvIII. U87-EGFRvIII cells transfected with siRNA-QDs have been cultured on the stride and square pattern to compare the focal adhesion formation (FAF) with normal U87-EGFRvIII cells. By measuring their elongated length on the pattern, the FAF was quantified and evaluated. For cancer cell migration, a microfluidic device was utilized to derive the velocity change of U87-EGFRvIII containing siRNA-QDs, which is caused by difference of the expression of integrin proteins. As a complementary study, western blotting is being performed to correlate it with the genotype change of related proteins such as focal adhesion protein, integrin, AKT, and S6 after the knock-down of EGFRvIII.

CURRICULUM VITAE

Jongjin Jung

EDUCATION:

2002~2010 Ph.D. in Chemistry, Dept. of Chemistry and Chemical Biology
Rutgers, The State University of New Jersey, New Brunswick, NJ, USA

2008~2010 Graduate Research, Rutgers University, New Brunswick, NJ
(Advisor: Dr. Ki-Bum Lee)

2002~2007 Graduate Research, Rutgers University, New Brunswick, NJ
(Advisor: Dr. David S. Talaga)

1997~2001 B.S. in Biochemistry, Yonsei Univeristy, Seoul, KOREA

PUBLICATIONS:

Jung, J.; Kim, C.J.; Park, J.K. ; and Lee, K.-B. “The multimodal magnetic nanoparticle platform for the targeted MRI imaging and the combined chemotherapy with siRNA and anticancer drug coupled with biodegradable PBAEs (poly(β -amino ester)s)” *Angew. Chem. Int. Ed (in preparation)*

Park, J.K.; **Jung, J.**; Subramaniam, P.; Shah, B.P.; Kim, C.; Lee, J.K.; Cho, J.-H.; Lee, C.; and Lee, K.-B. “Targeted multifunctional magnetic nanoparticles for synergistic siRNA delivery and hyperthermia for brain tumor cells” *Angew. Chem. Int. Ed. (in Revision)*

Jung, J.; Solanki, A.; Memoli, K.A.; Kamei, K.-I.; Kim, H.; Drahl, M.A.; Williams, L.J.; Tseng, H.-R.; Lee, K.-B. “Selective Inhibition of Human Brain Tumor Cells through Multifunctional Quantum-Dot-Based siRNA Delivery” *Angew. Chem. Int. Ed.* **2010**, 49(1), 103-107.

Lee, K.-B.; Solanki, A.; Kim, J.D.; **Jung, J.** “Nanomedicine: dynamic integration of nanotechnology with biomedical science”, Zhang, M., Editor, World Scientific, **2008**.

Jung, J.; Lim, S.K.; Kim, Y.; Weontae Lee. “ NMR structure of a minimum activity domain of human para-thyroid peptide hormone: structural origin of receptor activation” *J Pept Res* **2002** Nov, 60(5), 239-246